Mechanics of Silicon Electrodes in Lithium Ion Batteries

by

Yonghao An

A Dissertation Presented in Partial Fulfillment
of the Requirements for the Degree
Doctor of Philosophy

Approved on March 2014 by the
Graduate Supervisory Committee:

Hanqing Jiang, Chair
Nikhilesh Chawla
Patrick Phelan
Yinmin Wang
Hongyu Yu

ARIZONA STATE UNIVERSITY

May 2014

ABSTRACT

As one of the most promising materials for high capacity electrode in next generation of lithium ion batteries, silicon has attracted a great deal of attention in recent years. Advanced characterization techniques and atomic simulations helped to depict that the lithiation/delithiation of silicon electrode involves processes including large volume change (anisotropic for the initial lithiation of crystal silicon), plastic flow or softening of material dependent on composition, electrochemically driven phase transformation between solid states, anisotropic or isotropic migration of atomic sharp interface, and mass diffusion of lithium atoms. Motivated by the promising prospect of the application and underlying interesting physics, mechanics coupled with multi-physics of silicon electrodes in lithium ion batteries is studied in this dissertation. For silicon electrodes with large size, diffusion controlled kinetics is assumed, and the coupled large deformation and mass transportation is studied. For crystal silicon with small size, interface controlled kinetics is assumed, and anisotropic interface reaction is studied, with a geometry design principle proposed. As a preliminary experimental validation, enhanced lithiation and fracture behavior of silicon pillars via atomic layer coatings and geometry design is studied, with results supporting the geometry design principle we proposed based on our simulations. Through the work documented here, a consistent description and understanding of the behavior of silicon electrode is given at continuum level and some insights for the future development of the silicon electrode are provided.

DEDICATION

This dissertation is dedicated to my son, Jiyao, who was born in California during the days when I was conducting my research at Lawrence Livermore National Laboratory, and to my wife, Yipei, for the unconditional love and support she has for me.

ACKNOWLEDGMENTS

I first would like to thank my advisor, Prof. Hanqing Jiang, who has always been helpful, supportive, and caring ever since I entered the PhD program at Arizona State University. His vision, leadership, and work ethics will always be among the virtues I can learn and benefit from in my lifetime.

I also love to thank Dr. Morris Wang, who has been advising me during the past two years I spent at LLNL. He taught me so much as a materials scientist, an experimentalist, and a professional researcher.

In addition, I am very grateful for all the help and advice from my committee members, Prof. Nikhilesh Chawla, Prof. Patrick Phelan, and Prof. Hongyu Yu.

Last but not the least, the help and support from my colleagues at LLNL, Dr. Ming Tang, Dr. Brandon Wood, Dr. Jianchao Ye, Dr. Tae Wook Heo, Dr. Fang Qian, and my colleagues at ASU, Dr. Teng Ma, Dr. Jiaping Zhang, Dr. Cunjiang Yu, Dr. Huiyang Fei, are truly appreciated.

The work in this dissertation was partially supported by the Lawrence Scholar Program, and by the LDRD program (PLS 12-ERD-053) at LLNL.

TABLE OF CONTENTS

Page

CHAPTER Page

LIST OF TABLES

LIST OF FIGURES

Figure Page

CHAPTER 1

INTRODUCTION

1.1. Background

Lithium Ion Battery (LIB) today is not only a developing technology for energy storage, but also a fast growing industry such that the global market for LIB is expected to pass $25 billion by 2017, no mention all the other related industries that are bottlenecked by the development of LIB. It continues to advance as high power and high capacity cells increase penetration into large-format applications. For market adoption, the lithium-ion chemistry competes mainly with established energy storage technologies, such as lead acid, in many of these applications. However, key performance characteristics such as high energy density have enabled LIB to increase market penetration, resulting in growth opportunities. Currently most lithium-ion batteries are used in consumer electronic devices like mobile phones, notebook PCs, and for automotive products used in Electric Vehicles (EV). LIBs for storage have come into the spotlight due to the electricity supply issues resulting from the eastern Japan earthquake and the global efforts to embrace smart grids and green energy. With domestic and overseas LIB makers entering the markets for storage systems, the market for LIBs for storage is taking off.

The concept of LIB was developed as an improvement to curb the safety issues in Primary Lithium Battery (PLB), which was first proposed in 1976 by Whittingham [1]. Different from PLB, which is using lithium metal as negative electrode, LIB uses materials containing lithium ions as the both electrodes. The electrochemical intercalation of lithium into graphite was first demonstrated by Basu in 1977 [2, 3], later

patented at Bell Labs. Thus, as the first successful negative electrode material containing Li ions, LiC6, made the LIB possible. On the other hand, the first positive electrode material for LIB, LiCoO2, still in use today, was demonstrated and patented by Goodenough *et al.* in early 1980s [4, 5]. After that, lots of effort had been made on the development of electrode and electrolyte materials for LIB [6-8] until the release of the first commercial LIB by Sony Corporation in 1991. The introduction of $LiFePO_4$ (LFP) and other phospho-olivines as the positive electrode materiasl by Goodenough *et al.* in 1996 [9] and improvement of these materials towards commercialization by Yet-Ming Chiang later [10-12] boosted the application of LIB into another level.

Started around 2007 and still ongoing, the latest wave of research and development for LIB has been continuously on heat in both academia and industry, in the search for next generation of the LIB with higher energy and power density, longer life time, better safety performance, and low cost *etc.,* driven by the giant rising market for consumer electronics, electric vehicles, and energy storage devices in smart grid. In academia, not being a complete list, a number of groups at Stanford university [13-27], Sandia National Laboratory [28-41], University of St Andrews, UK [42-52], Georgia Tech [53-58], are among the most active research groups in the field of LIBs, while in the industry, TDK Corporation, Samsung SDI Co. Ltd., LG, Panasonic, and Hitachi, are some of the biggest players, as the fast spreading application of LIB in consumer electronics.

1.2. Lithium Ion Batteries

A LIB is one type of rechargeable batteries. Different from non-rechargeable lithium battery using lithium metal as one electrode, widely used button cell battery for example, LIB uses lithium compounds for both two electrodes. Lithium ions shuttle

between two electrodes as charge carriers during the charging/discharging operation of the battery. Typically, one battery is composed of several electrochemical cells, connected in series and/or in parallel to provide desired voltage, capacity, and power. The structure of an individual cell of LIB is illustrated in Fig. 1.1.

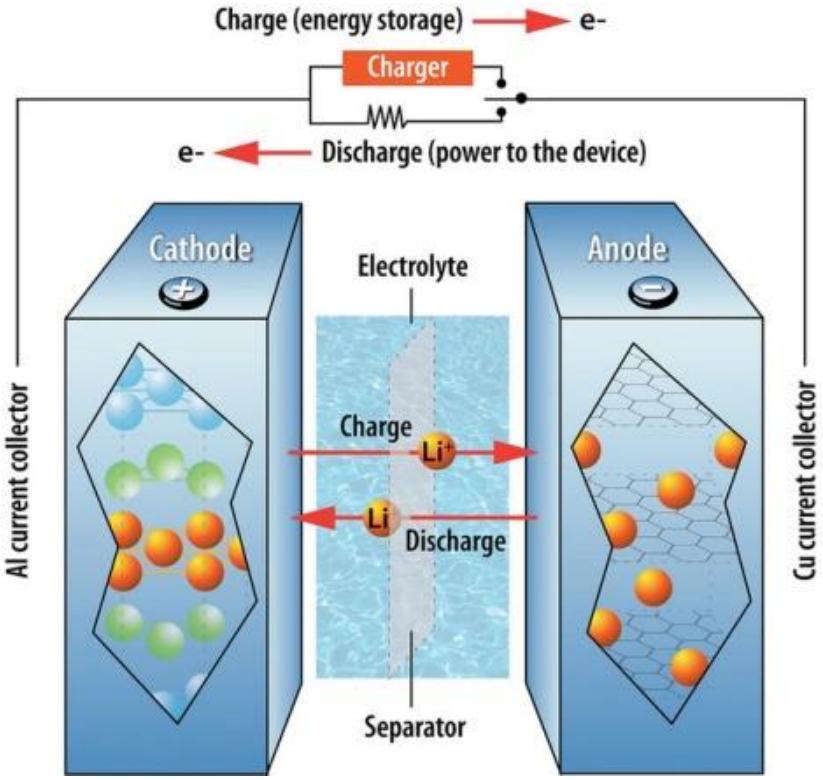

Figure 1.1. Illustration of the structure of electrochemical cell of LIB.

Like any other electrochemical systems, a LIB cell contains three key components, two electrodes (cathode, and anode), and the electrolyte [59]. Usually, electrodes are exclusively conductive to electrons, while electrolyte is exclusively conductive to lithium ions. For a LIB, when the two electrodes are connected through an external circuit to power a device, it is called discharge. Determined by the nature of the electrode materials, electrons have higher Electrochemical Potential (ECP) in one electrode than in the other. If measured with voltmeter using a third standard electrode as reference, the

electrode with higher ECP will have lower voltage reading compared to the electrode with lower ECP. Therefore, the electrode with higher ECP is marked as negative electrode of the battery, and the other electrode with lower ECP is marked as positive electrolyte. During discharge, the electrons spontaneously flow from negative electrode to the positive electrode, while lithium ions flow from negative electrode to positive electrode through internal electrolyte. Faradaic process happens at the interfaces between electrodes and electrolyte, to transfer charges between electrons and lithium ions. At the interface between negative electrode and electrolyte, lithium in electrode is oxidized, and dissolved into electrolyte in the form of lithium ion. In the meantime, stoichiometric amount of electrons are produced, flowing to the other electrode. This current flowing out is called anodic current, and the negative electrode for battery is called anode. On the other end, lithium ions in electrolyte get reduced, and enter positive electrode to form compound, at the cost of electrons transported from anode consumed stoichiometrically. This current flowing in called cathodic current, and the positive electrode for battery is called cathode. When a LIB is fully discharged, a charge process is needed to restore its capacity. Charge is not a spontaneous process as discharge, thus an proper external power supply have to be used to force electrons flow from anode to cathode through external circuit and lithium ions transport from the anode to the cathode through internal electrolyte. As a result, reverse reactions as described above happen at two electrodes. Taking the LIB cell illustrated in Fig. 1.1 as an example, graphite and LiFePO4 are used as anode and cathode materials, respectively. The electrochemical reactions at two electrode/electrolyte interfaces are formulated as

$$C + xLi^{+} + xe^{-} \underset{\text{discharge}}{\overset{\text{charge}}{\rightleftharpoons}} LixC$$

$$LiFePO_4 \underset{\text{discharge}}{\overset{\text{charge}}{\rightleftharpoons}} xLi^{+} + xe^{-} + Li_{1-x}FePO_4$$

As shown in Fig. 1.1, in addition to electrodes and electrolyte, there are some other assisting components in a LIB cell. Current collectors are used to facilitate the electric contact between active electrode material and the external circuit. Highly conductive materials such as metals, graphene, or conductive polymer are chosen due to the different electrode material and working condition. Seperators are porous semipermeable membranes that allow lithium ions pass through while electrically insulated, therefore help to avoid the internal short circuit due to the direct contact of the two electrodes.

An electrolyte is a material in which the mobile species are ions and free movement of electrons are blocked. Several kinds of lithium ion conductors have been used as electrolyte for LIB, including organic liquid electrolytes [60-63], ionic liquid electrolytes [64-66], inorganic liquid electrolytes [67, 68], and solid polymer electrolytes [69-71], and inorganic solid electrolytes [72-75]. Among above mentioned electrolytes, organic liquid electrolytes are most commonly used electrolytes. They are solutions of lithium salts such as $LiPF_6$ in one or more of the carbonates solvents, including ethylene carbonate (EC), diethyl carbonate (DEC), dimethyl carbonate (DMC), ethylmethyl carbonate (EMC), or propylene carbonate (PC). Organic liquid is relatively less viscous therefore gives higher Li ion mobility. However, they are also highly flammable materials, which brings safety concerns when large scale applications come to consideration. Therefore, other types of electrolyte are studied, despite that they are still suffering from the limitation of being chemically unstable, small operational voltage window, or poor ion conductivity for practical purpose.

An electrode is a material in which the electrons are the mobile species and therefore can be used to sense or control the potential of the electrons. Materials with

host structures into/from which guest lithium atoms can be inserted/extracted upon charge/discharge process reversibly are chosen for the electrodes in LIB. Electrode materials that have been utilized in LIB include carbons (graphite, graphene, and carbon nanotube) [76-80], metals [14, 16, 34, 81-84], metal oxides [33, 41, 85-91], metal phosphides/sulfides/fluorides [10, 92-100], and composites/hybrid materials [19, 23, 101-107]. The insertion/extraction mechanism varies from material to material, but there are two representative types among them. First one is for so called "intercalation" material such as graphite, $LiFePO_4$, or TiO_2, who has interstitial/inter-layer space in its crystal structure to accommodate lithium atoms. Therefore, upon insertion/extraction, its crystal structure remains intact in principle. Intercalation material has the advantage of higher lithium diffusivity therefore higher rate performance, and less mechanical deformation upon composition change. However, it also has the disadvantage of less lithium capacity. The other one is so called "alloying" mechanism, for materials like tin, germanium, and silicon, *etc.* [82]. Those materials can alloy with very high concentration of lithium and therefore position themselves among materials for electrodes with the high capacity. Nevertheless, alloy materials are short of the big volumetric change upon insertion/extraction of lithium, and relatively low rate performance. There is another big category of electrode materials, including some metal oxides/sulfides/phosphides. The mechanism in these materials is a conversion reaction, which is not reversible in most cases and therefore hinders the application of this type of material.

Besides searching for alternative electrolytes for LIB, experimental progress on LIB research includes the application of unconventional materials especially engineered nanomaterials [19, 23, 91, 108-117] and hybrid materials [19, 99, 103, 109, 116, 118-123]

in electrodes, functionality and integration of the battery package [15, 27, 56, 58, 124-130], low cost and environment friendly synthesis techniques [14, 53, 117, 131], and advanced characterization techniques of the battery materials and behaviors[31, 32, 132-134], and so on. From theory/modeling perspective, first-principles simulations[135-139], molecular dynamics [140-144], as well as continuum modeling [39, 145-149] including phase field method [150, 151] and finite element simulation[152, 153], all provide us with insights from full spectrum of scales for the multi-physics underlying the electrochemical operation of LIBs.

1.3. Silicon Electrodes

As one of the high capacity alloying materials, silicon attracted a large amount of attention in search of novel electrode materials for LIB [13, 14, 16, 18, 23, 25, 35, 54, 56, 84, 101, 113, 117, 129, 154-166]. It is known to have the highest gravimetric capacity among all the electrode materials for LIB, 4200 mAh/g theoretically. A variety of approaches have been explored to improve the performance of the silicon electrode in LIB, including nanomaterial, structure optimization, surface coating/treatment, and so on.

In the meantime, advanced experimental techniques and ab initio computational capabilities have been utilized to investigate the physics involved in the electrochemical lithiation/delithiation process of silicon electrodes. A number of interesting phenomena have been observed or discovered through these studies. The first one is the large volume change (up to 300%) of silicon electrode upon lithiation and delithiatoin [13, 35, 36], which is anisotropic for the initial lithiation of crystal silicon [21, 139], in most cases followed by anisotropic size dependent fracture of the electrodes [20, 26, 30, 36]. Lithiation/delithiation is the insertion/extraction of lithium to the silicon electrode.

Associated with it, is the lithiation/delithiation induced phase transformation [38, 167], and in the case of crystal electrode, it is anisotropic due to the anisotropic mobility of the atomic sharp interface[39, 40, 136, 139, 168]. The phase transformation upon lithiation/delithiation gives rise to the composition dependent plasticity/softening of the materials [28, 132, 137, 141, 169-172]. In addition to its orientation dependence in crystal silicon, the phase transformation kinetics in silicon electrode is found to depend on the size, the stress state, and the electrochemical conditions of the electrode [17, 29, 35, 144, 149].

Therefore, motivated by the exciting prospect of the application of silicon electrode in LIB, and the inspiring physics underlying the various interesting behaviors, this dissertation is devoted to study the mechanics and its coupling with other mechanisms in the silicon electrode in LIB, in an attempt to give an unified description and understanding from continuum level of the phenomena in silicon electrode in LIB, by incorporating the information from experiments and atomic calculations in literature, and making use of the merit of the continuum modeling itself. Our goal is to provide advice for the future development of the silicon electrode through models that have been preliminarily verified in experiments.

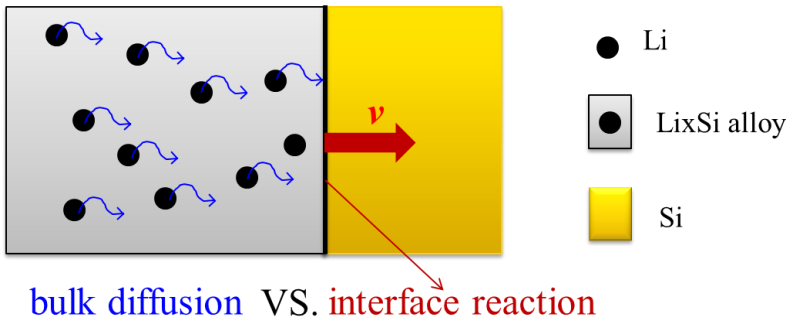

Figure 1.2. Illustration of the lithiation kinetics in Si electrodes in LIB.

The core argument of this dissertation is as follows. The lithiation process of the Si electrode involves two aspects of kinetics, as illustrated in Fig. 1.2, without taking into account of the surface effect at the electrode-electrolyte interface. First, Li enters the electrode at the interface with electrolyte, diffusing through the bulk amorphous LixSi alloy, and reaches the interface with Si (amorphous or crystal). This is a bulk diffusion process. Second, at the interface between LixSi alloy and Si, the Si-Si bonds are broken, new Li-Si bonds are formed, and the incoming Li are accommodated. Because there is rearrangement of chemical bonds at the interface, we call this process interface reaction. The reaction result in the phase change at the interface. These two processes compete with each other. Bulk diffusion provides the reactants for interface reaction, while interface reaction makes room for bulk diffusion. The diffusion controlled mass transport, is characterized by Li diffusivity D, in unit m^2/s. The interface controlled phase change is characterized by the interface velocity, in unit m/s. The ratio of diffusivity over interface velocity, gives a critical length, $L_c = D/v$. For a Si electrode with characteristic size A, two simplified cases are considered in this dissertation. In case I, the size of electrode is much bigger than the critical length, $A >> L_c$, and the diffusion time A^2/D is much larger than the reaction time A/v, therefore, the Li concentration in LixSi alloy doesn't have enough time to reach equilibrium, leading to a gradient distribution. The kinetics of the system is diffusion controlled. It is an isotropic process because as a second order tensor diffusivity D is expected to be isotropic in both amorphous phases (LixSi alloy or amorphous Si), and in crystal Si with cubic symmetry. In case II, the size of the electrode is much smaller than the critical length, $A << L_c$, and the diffusion time A^2/D is much smaller than the reaction time A/v, therefore, the Li

concentration in LixSi alloy has enough time to reach equilibrium, leading to a constant distribution. The kinetics in the system is interface controlled. It could be an anisotropic process because the interface velocity could depend on the local crystal orientation of the interface if the interface is between crystal and amorphous phases.

The content of this dissertation is arranged as follows. In Chapter 1, the topic and the scope of the dissertation are introduced. In Chapter 2, the coupling of finite deformation and mass diffusion in large silicon electrodes is studied as the first simplified case, while the anisotropic interface reaction and geometry design of nano crystal electrodes are discussed as the second simplified case in Chapter 3. In Chapter 4, we reported our experimental work on silicon pillars as electrodes in LIB, to partially verify our concept of geometry design for crystal electrode proposed in Chapter 3. A summary of the dissertation and future outlook are provided in Chapter 5.

CHAPTER 2

COUPLED FINITE DEFORMATION AND MASS DIFFUSION IN LARGE ELECTRODES

Due to the significant effect of self-constraint in silicon electrodes with relatively large size, the short lifetime confined by the mechanical failure is now considered to be the biggest challenge in desired applications. High stress induced by the huge volume change due to lithium insertion/distraction is the main reason underlying this problem. Some theoretical models have been developed to address this issue under the assumption that for large electrodes, the kinetics of lithium transportation is diffusion controlled. In order to properly implement these models, we develop a finite element based numerical method using a commercial software package ABAQUS, as a platform at the continuum level to study fully coupled large deformation and mass diffusion problem. By using this method, large deformation, elastic-plasticity of the electrodes, various spatial and temporal conditions, arbitrary geometry and dimension could be fulfilled. The interaction between anode and other components of the lithium ion batteries can also be studied as an integrated system. Several specific examples are presented to demonstrate the capability of this numerical platform and estimate their fracture performance upon lithiation.

2.1. Introduction

LIBs, as one type of rechargeable batteries, have attracted a great deal of attention due to their high-energy density, no memory effect, reasonable life cycle, and one of the best energy-to-weight ratios that are used in applications such as portable electronic devices, satellites and potentially electric vehicles [173-175]. Among the active research occurring in electrode materials for Li-ion batteries, the development of novel electrodes that show both high-energy and high-power density are much sought after. Silicon (Si) is an attractive anode material for Li-ion batteries because it has a low discharge potential and the highest known theoretical charge capacity of 4,200 mAh/g, ten times higher than that of existing graphite anodes and other oxide and nitride materials [13]. However, the development of Si-anode Li-ion batteries has lagged behind because of the large volumetric change that occurs upon insertion and extraction of Li. During charge/discharge cycling, Li atoms diffuse in and out the Si matrix and different Li_xSi phases are formed depending on the Li concentration. The largest volumetric change occurs for $Li_{22}Si_5$ alloy, where up to 300% volumetric change is required to accommodate 4.4 Li atoms for each Si atom, resulting in pulverization and early capacity fading of the battery cells due to the loss of electrical contact [176, 177].

The extraordinarily high energy capacity of Si, nonetheless, has motivated researchers to explore new means that curb the limitation of Si as a practical anode material for Li-ion batteries. Exploration of Si nanostructures is one of the encouraging research directions, such as nanowires or nanotubes [13, 129, 156, 165, 178]. High energy capacity has been realized through these attempts, but only in the first few tens of cycles of charging and discharging and dropped quickly in the following cycles. The total cycle number is still low.

In order to improve the cyclic stability of Si anodes, the mechanism underlying the behavior of failure should be well understood in the first place. From the perspective of mechanics, the failure of lithiated Si can be attributed to the high level of lithiation induced stress [179]. It is possible that the high stress level in Si could also affect the electrochemical performance of the Si anodes [180], such as changing the working voltage of the battery and influencing the charging rate of the battery. Therefore, besides as a key factor in understanding the failure of Si under lithiation, stress might also be an important factor that affects the performance of Li-ion batteries. Motivated by these aforementioned aspects, a large amount of work has already been conducted to examine the fundamental role of stress in Si anode in Li-ion batteries.

Novel phenomena for Si anode in Li-ion batteries have been observed in experiments. Some of them are beyond the traditional scope of our knowledge on the mechanical behavior of Si, such as the plasticity of lithiated Si [172]. Optical method has been used to *in-situ* measure the stress evolution in lithiated/delithiated Si film. A novel feature, plasticity, has been observed in this classic material that is usually considered to be brittle [181].

From the theoretical aspect, specifically at the continuum level, various types of models have been proposed regarding the multiple mechanisms through which stress is coupled with mass diffusion. The model of diffusion induced stress can be dated back to the work by Prussin in 1960s [182], in which an analogy between diffusion induced stress and thermal stress was used. In Prussin's original work, he assumed a one-way coupling in which the diffusion of the alien particles into the matrix material produced stress in the same way as the temperature load in thermally expandable materials. This work was broadened by considering mass-diffusion resulted heterogeneous materials as elastic

inclusion problems, in which the inclusion energy has been incorporated into the chemical potential of migrating particles [183-185]. Thus the coupling between mass diffusion and deformation has become a two-way behavior. Explicitly, local stress level affects how fast particles could migrate into a matrix material, and in turn, the mass distribution of alien particles affects what kind of stress distribution the matrix material would take. Later, Swaminathan *et al.* [186] developed a strict electromechanical theory to address the diffusion induced stress problem, in which not only the elastic inclusion energy induced by the migrating defect was considered, but also electrostatic energy was counted in for charged defects. In this theory, an alien particle in a matrix material induces stress through two mechanisms, namely strain induced by the geometrical incompatibility, and Maxwell stress due to the charge carried by the particle. Recently, based on molecular dynamic simulations, another mechanism has been proposed though which stress could affect diffusion [145, 187]. It is a kinetic mechanism, in which the diffusivity of an alien particle in a matrix material is exponentially dependent on the lateral normal stress applying perpendicular to the diffusing direction. To sum up, previous studies have already shown at least four mechanisms to couple mass diffusion and deformation or stress, namely mass distribution of alien particles affecting deformation through geometric mismatch (mechanically) and carried charge (electrostatically), and stress or deformation of alien particles affecting mass diffusion through chemical potential (thermodynamically) and diffusivity (kinetically). Above mentioned studies were limited to elastic behavior of Si anode.

Motivated by recent experimental observation of plasticity of lithiated Si, there are a handful of theoretical studies incorporating the Si plasticity [188, 189]. By employing the nonequilibrium thermodynamics, Zhao *et al.* [190] considered the

coupled plastic deformation and lithiation in a spherical anode. Bower *et al.* [147] developed a systematic theory to include finite deformation, diffusion, plastic flow, and electrochemical reaction in Si anode of Li-ion batteries. However, because of the complexity of these models, only simplified cases [191] were studied though the theoretical frame is somewhat completed. In order to utilize these proposed models to study more realistic situations, which include more complicated conditions, such as shapes of electrodes, mechanical and electrochemical boundary conditions with spatial and temporal complexity, as well as interaction of electrodes with different type of substrates and binders, a robust and versatile numerical platform must be developed correspondingly. To the best of our knowledge, such numerical platform that is able to rigorously couple the important factors in electrodes, namely large deformation, mass diffusion and plasticity, is not available to the research community, though there are many related works on coupled mass diffusion and elasticity [192-195], or based on small deformation theory [20, 39]. More importantly, the numerical platform must be capable of studying the fracture and damage of electrodes, which makes this task more challenging.

In this chapter, we propose a finite element based numerical method using the commercial finite element package ABAQUS, as a platform to study fully coupled large deformation and mass diffusion problem in electrodes. The present work has two merits to differentiate it from previous studies [196]. First, coupled large deformation (elasticity and plasticity) and mass diffusion is realized. The four coupling mechanisms as we previously discussed can be realized in this platform. Second, the implementation of this numerical method is realized via commercially available software so that the complicated mechanical and electrochemical boundary conditions can be readily imposed and

electrodes with various geometries, such as three dimensional bulk, two dimensional thin film, and one-dimensional nanowires and nanotubes can be studied. Even in the system level, the interaction between the electrodes with other components in Li-ion batteries, such as current collector, substrate and binders, can be studied. Moreover, the facture and damage of electrodes can be studied through the established modules in the commercial software package, such as cohesive elements for interfacial failure. Such a numerical platform with a rigorous consideration of coupled large deformation, mass diffusion and plasticity using commercial software package, therefore, provides a robust and versatile means to study the coupled large deformation and mass diffusion in electrodes of Li-ion batteries.

This chapter is organized as follows. In section 2.2, a general theoretical framework of coupled diffusion and large deformation is addressed. This theoretical framework will be used to develop the numerical method. Section 2.3 details the numerical implementation, which is based on a rigorous analogy between mass diffusion and thermal transport when the large deformation presents. Section 2.4 presents a one-dimensional example that is studied by using the present method and compared with the COMSOL Multiphysics as the benchmark. Section 2.5 studies some practically important examples, namely Si anode is bonded on current collector with and without soft binders, in which the damage and cohesive elements are involved, and the interplay between the different failure mode in binder and anode film is investigated. The future work and application of the numerical method are discussed in Section 2.6 as the concluding remarks.

2.2. Theoretical Model

In this section, the theoretical model for coupled large deformation and mass diffusion in electrodes for Li-ion batteries is generalized and integrated by following the previously developed models [147, 190, 197]. The Lagrangian description is used in depicting the model. Here the physical explanations are the focuses while the rigorous derivation and proof are left for the previously developed models.

2.2.1. Kinematics of deformation

The process of charging and discharging in Li ion battery is the process of Li migrating in and out of the electrodes, such as Si electrode. Thus the objective of interest consists of Li and electrode and it is referred as the system. Following the standard continuum mechanics, deformation gradient $\mathbf{F}(\mathbf{X},t)$ is used to describe the deformation of the system. $\mathbf{X}$ is the coordinates of a material point at the reference state, which is chosen to be the state for pure electrode or completely discharged electrode. t is time at the moment. To characterize the distribution of Li in the electrode matrix, the nominal concentration of Li $C(\mathbf{X},t)$ is defined as the mole of Li per unit volume of electrode at the reference state.

It is assumed that the deformation gradient $\mathbf{F}$ could be polar decomposed into three parts, namely, deformations due to material's elasticity, plasticity, and concentration change, respectively [147, 190]. Furthermore, these three parts could be diagonalized concurrently. Thus, the principle stretches could be decomposed into three parts, i.e., elastic, plastic, and concentration parts,

$$\lambda_i = \lambda_i^e \lambda_i^p \lambda_i^c \quad (i = 1, 2, 3. \text{No summation convention}). \tag{2.1}$$

Here the superscripts "*e*", "*p*", and "*c*" denote elastic, plastic and concentration parts, respectively. The principal stretch due to concentration change is assumed to be isotropic,

$$\lambda_1^c = \lambda_2^c = \lambda_3^c = \lambda^c(C), \tag{2.2}$$

though it may not be valid for crystal materials, such as Si in which the stretch due to concentration change depends on the crystal orientation [36].

2.2.2. Constitutive relations

Assume that the nominal free energy density of the system W can be defined as the function of the seven basic variables, λ_1^e, λ_2^e, λ_3^e, λ_1^p, λ_2^p, λ_3^p, and C. Utilizing the thermodynamics inequality and incompressibility of plasticity, the chemical potential μ of Li in an electrode, and true stress $\boldsymbol{\sigma}$ in the Li/electrode compound could be determined by

$$\sigma_i = \frac{1}{\lambda_1\lambda_2\lambda_3}\frac{\partial W}{\partial \ln \lambda_i^e}, \tag{2.3}$$

$$\mu = \frac{\partial W}{\partial C} - \lambda_1\lambda_2\lambda_3\sigma_h \frac{3}{\lambda^c}\frac{d\lambda^c}{dC}. \tag{2.4}$$

Here $\sigma_i (i = 1,2,3)$ is the principal true stress, and $\sigma_h = \frac{1}{3}(\sigma_1 + \sigma_2 + \sigma_3)$ is the hydrostatic stress. The detailed derivation can be found in [190]. Eq. (2.3) and Eq. (2.4) provide constitutive relations of the Li/electrode system.

In a recent work by Z.W. Cui *et al.* [146], in addition to the hydrostatic stress, the deviatoric stress also enters the chemical potential in the form of Eshelby stress tensor. Moreover, the dependence of material's mechanical property on the compositional strain makes another contribution of deformation to the chemical potential. We adopt the

hydrostatic stress-dependent chemical potential in the following analysis, though the general stress dependent chemical potential could be easily implemented using the similar approach.

2.2.3. Material models

The nominal free energy density of the system W consists of strain energy density and chemical energy density,

$$W(\lambda_i^e, \lambda_i^p, C) = W_s(\lambda_i^e, \lambda_i^p) + W_c(C). \tag{2.5}$$

$W_s(\lambda_i^e, \lambda_i^p)$ is the strain energy density exclusively depending on elastic-plastic deformation. In other words, $W_s(\lambda_i^e, \lambda_i^p)$ is caused by the change of atomic potential of electrode atoms due to the change of their distance induced by mechanical deformation elastically or plastically. $W_s(\lambda_i^e, \lambda_i^p)$ vanishes when $\lambda_i^e = \lambda_i^p = 1$ ($i = 1,2,3$). Different forms of strain energy density will give different mechanical constitutive relations. Here we decide not to specify and leave it in a general form, while the specific mechanical constitution we used in our simulation is described in the following section. $W_c(C)$ is the chemical energy density introduced in the system due to the new chemical bonding formed between Li and electrode atoms which depends on the electrochemical reactions, as well as the entropy increase because of mixing these heterogeneous species which is similar to that in the solution theory. As an example, a specific form of the chemical energy density is given by following Haftbaradaran *et al.*'s work [197],

$$W_c = RTC_{\max}\left(\bar{C}\ln\bar{C} + \left(1-\bar{C}\right)\ln\left(1-\bar{C}\right)\right) + C_{\max}\bar{C}\left(1-\bar{C}\right)\left(A_0\bar{C} + B_0\left(1-\bar{C}\right)\right). \tag{2.6}$$

Here RT is the product of gas constant R and absolute temperature T (i.e., energy per mole), $C_{\max}$ is the maximum concentration that could ever be reached in the Li/electrode

system, and $\bar{C} = \frac{C}{C_{\max}}$ is the normalized concentration that is used to characterize the relative saturation level of Li in an electrode. A_o and B_o are two empirical parameters. The first term in Eq. (2.6) describes the mixing entropy based on the ideal mixing from the solution theory, and the second term in Eq. (2.6) represents the energy of forming new chemical bonding which is also called excess energy, accounting for deviation from ideal behavior of mixing. The excess energy reflects the existence of different Li/electrode phases at different Li concentrations, which depends on the process of electrochemical reactions. It should be noted that it is not necessary to take the form as suggested by Eq. (2.6), which is specifically called three-suffix Margules model [198]. In fact, different forms, such as Van Laar model and Wilson model, have been developed and other empirical parameters (similar to A_o and B_o) have been employed. One must realize that accurate modeling needs to use more realistic excess energy for the Li/electrode system and thus detailed information on the phase transition of Li/electrode system is important.

Recent experiments have revealed that the lithiation process s involves sharp phase boundary between Li rich and Li poor phases [22, 35, 38]. The motion of the phase boundary is isotropic in amorphous Si while anisotropic in crystal Si [21]. The current numerical approach can be extended for the diffusion controlled phase boundary problem, though the numerical simulation of these phenomena is not within the scope of the present work. The basic idea is to follow the phase field method to model the coexistence of two phases. A free energy with double well has to be constructed by choosing the proper parameters A_o and B_o in the excess energy (Eq. (2.6)). In order to suppress the instability at the interface, the interface energy between two phases will be

introduced. To consider the anisotropic motion of the phase boundary, the orientation dependence of surface energy can be introduced. Similar idea has been used by Hong and Wang [199]. Different from the diffusion controlled interface motion as discussed above that can be easily realized through a slight modification on our numerical platform, the reaction controlled phase boundary motion cannot be implemented by a simple modification of the present platform, and will be presented in Chapter 3.

Substituting Eq. (2.6) into Eq. (2.4), the chemical potential per mole is given as

$$\mu = RT\ln\frac{\bar{C}}{1-\bar{C}} - \left[2\left(A_0 - 2B_0\right)\bar{C} - 3\left(A_0 - B_0\right)\bar{C}^2\right] - \lambda_1\lambda_2\lambda_3\sigma_h\frac{3}{\lambda^c}\frac{d\lambda^c}{dC}. \qquad (2.7)$$

The first term is the driving force for Li diffusion, which urges Li to diffuse from places with high concentration to places with low concentration; the second term depends on the quadratic term of Li concentration and thus prefers to keep Li at pre-determined state depending on the two empirical parameters A_o and B_o, which leads to phase separation; and the third term reflects the influence of stress on the chemical potential, which can be understood by the analogy of a pipette, i.e., a negative pressure "pumping in" and a positive pressure "squeezing out".

The $d\lambda^c / dC$ term actually defines a coefficient of compositional expansion, similar to coefficient of thermal expansion. As a simplest model, the stretch due to the change of Li concentration is assumed to be linearly dependent on Li concentration,

$$\lambda^c\left(C\right) = 1 + \beta\bar{C}. \qquad (2.8)$$

Here β is the non-dimensional coefficient of compositional expansion, which can be determined by the maximum volumetric change of the electrode during charge and discharge.

It is noticed that different volume expansion has been suggested, such as linear dependence of volume change on concentration [141, 148, 200]. Before more accurate experimental measurement, these two forms of compositional expansion are both reasonable. We adopt Eq. (2.8) in the following analysis, though other expressions of compositional expansion can be similarly implemented.

2.2.4. Mechanical constitution

Neither the model/numerical approach is limited to any particular mechanical constitutions, nor is this chapter focused on the topic of a realistic mechanical constitution. In fact one would find the present numerical platform in this chapter is compatible with most of the standard or user defined mechanical models. In order to provide a completed model description, a simple elastic-plastic mechanical constitution is given here and used throughout our simulation. The logarithm strain is adopted as the strain measurement here, which is commonly used as the strain measurement in the updated Lagrangian description for nonlinear finite element analysis.

The elastic property of the material is assumed isotropic, with the constitutive relation in the principal directions as

$$\sigma_i = \frac{E}{1+\nu}\left(\ln\lambda_i^e + \frac{\nu}{1-2\nu}\left(\ln\lambda_1^e + \ln\lambda_2^e + \ln\lambda_3^e\right)\right), \tag{2.9}$$

where E, ν are the Young's modulus and Poisson's ration of the Si anode. For a small time increment in an updated Lagrangian description, this elastic constitutive relation recovers the linear Hook's law.

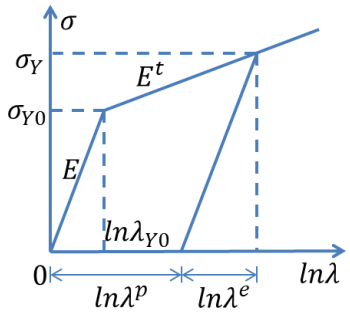

Figure 2.1. A bi-linear elastic-plastic strain-stress curve for a uniaxial tensile testing.

The Von Mises yielding criteria is adopted for the plastic deformation, as

$$\sigma_v = \sigma_Y\left(\ln \lambda_{eq}^p\right), \tag{2.10}$$

where σ_v is the Von Mises stress and defined by

$$\sigma_v = \sqrt{\frac{1}{2}\left[\left(\sigma_1-\sigma_2\right)^2+\left(\sigma_2-\sigma_3\right)^2+\left(\sigma_3-\sigma_1\right)^2\right]} \tag{2.11}$$

and σ_Y is material's yielding stress, which could be described as following when a linear stress hardening law is assumed as illustrated in Fig. 2.1,

$$\sigma_Y\left(\ln \lambda_{eq}^p\right) = \sigma_{Y0} + E^p \ln \lambda_{eq}^p . \tag{2.12}$$

Here σ_{Y0}, E^p are the initial yielding stress, and the "plastic" modulus respectively. $\ln \lambda_{eq}^p$ is the equivalent plastic strain that characterizes the accumulated plastic deformation during the deformation history, defined by

$$\ln \lambda_{eq}^p = \ln \lambda_{eq}^p\Big|_{t=0} + \int_0^t \sqrt{\frac{2}{3}\frac{d\left(\ln \lambda_i^p\right)}{dt}\frac{d\left(\ln \lambda_i^p\right)}{dt}}dt . \tag{2.13}$$

The incremental plastic strain is determined by the flow rule,

$$\Delta \ln \lambda_i^P = \Delta\alpha(t)\left(\sigma_i - \sigma_h\right), \tag{2.14}$$

and

$$\Delta\alpha(t)=\begin{cases}\Delta\alpha>0, \ for\ \dfrac{d\sigma_v}{dt}>\dfrac{d\sigma_Y}{dt},\sigma_V=\sigma_Y\\ 0, \qquad others\end{cases} \tag{2.15}$$

is a time dependent scalar which could be determined by the boundary value problem.

2.2.5. Governing equations and boundary conditions

The governing equations for the coupled large deformation and mass diffusion include mechanical equilibrium and mass conservation law as the following

$$\frac{\partial\sigma_{ij}}{\partial x_i}=0, \tag{2.16}$$

$$\frac{\partial C}{\partial t}+\frac{\partial J_K}{\partial X_K}=0. \tag{2.17}$$

The mechanical equilibrium is written in terms of true stress σ_{ij}, and current coordinates x_i, at the current time t. The mass conservation law is expressed in terms of the nominal concentration C, nominal mass flux J_K, and the reference coordinates X_K, at the current time t. The detailed derivations can be found somewhere else [147]. It should be noted that the usually used conservation law in small deformation,

$$\frac{\partial c}{\partial t}+\frac{\partial j_k}{\partial x_k}=0 \tag{2.18}$$

written using true quantities (true concentration c and true flux j_k) and current coordinates x_k, does not hold for large deformations.

Various boundary conditions for the coupled deformation and mass diffusion could be posed, including stress or displacement boundaries for mechanical deformation, and flux or concentration boundaries for mass diffusion. Specifically for Li-ion battery

problems, a meaningful boundary condition is the prescribed flux condition in reference coordinates,

$$J_K N_K = \bar{J} \quad on \quad S_f, \tag{2.19}$$

where $\bar{J}$ is the prescribed flux over a surface S_f with the outwards normal direction N_k in the reference state. Eq. (2.19) stands for the constant electrical current condition under which the battery is charging or discharging, or galvanostatic charging or discharging.

2.2.6. Kinetics

Similarly, kinetic law of describing the mass flux of Li into the electrode is given in terms of nominal quantities [147] other than true ones, as

$$J_I = -CM_{IJ}\frac{\partial \mu}{\partial X_J}, \tag{2.20}$$

where M_{IJ} is the mobility tensor, as a measurement of how fast Li diffuses in the electrode matrix. Here one should note that since the nominal flux **J** is used, the coordinates (I and J) in Eq. (2.20) are referred to the initial coordinates.

An alternative way to define flux in finite deformation theory is to assume that the true flux is proportional to the true gradient of chemical potential at the current state. These two definitions coexist in the literature [147, 148] and both have their own merits. In terms of implementation, one can easily switch from one to the other using the numerical platform in this chapter. In addition, the mobility tensor M_{IJ} can be connected through the deformation gradient with the diffusivity tensor in current state, which can be measured experimentally or determined from *ab initio* calculation.

Suggested by Haftbaradaran *et al.* [197], the lateral pressure that is perpendicular to the direction of diffusion could affect the diffusivity, working in a way similar to

frictional force. Therefore, a stress dependent mobility tensor is adopted and its nonzero components are

$$M_{11} = M_0 \exp(\kappa \frac{S_{22} + S_{33}}{2})$$
$$M_{22} = M_0 \exp(\kappa \frac{S_{11} + S_{33}}{2}) . \quad (2.21)$$
$$M_{33} = M_0 \exp(\kappa \frac{S_{11} + S_{22}}{2})$$

Here M_0 is the mobility at a stress-free state, κ is an empirical parameter describing the coupling between stress and diffusivity, and S_{IJ} is the second Piolar-Kirchhoff stress. The second Piolar-Kirchhoff stress is used since the mobility tensor is defined in the reference state.

The two-way coupling of deformation and mass diffusion is thus realized in this section, specifically the hydrostatic stress term in chemical potential as in Eq. (2.7), and the stress dependent mobility as in Eq. (2.21). No Maxwell stress is involved since the electrostatic interaction between Li and electrode matrix is not considered in this chapter.

2.3. Numerical Method

In order to utilize the theoretical model as presented in Section 2.2, a robust and versatile numerical method must be developed correspondingly. In addition to the development of an in-house code [201], a numerical method that is based on commercial software may be more powerful and easier to be disseminated in the community. In this section, we will present a rigorous numerical method to implement the theoretical model in Section 2.2 in a commercial finite element package ABAQUS. Here ABAQUS is chosen because of its wide use in the mechanics community.

The mechanical deformation, both elasticity and plasticity under large deformation, can be modeled in ABAQUS via its well-developed modules. Therefore, this section does not discuss the implementation of the mechanical deformation in ABAQUS but focuses on the coupled mechanical deformation and mass diffusion under large deformation in ABAQUS, since this coupling is not yet available in ABAQUS.

2.3.1. Dimensionless description of mass diffusion

A dimensionless formulation is used. The energy per mole is normalized by RT (unit: J/mole); mole density is normalized by $C_{\max}$ (unit: mole/m^3); length is normalized by a characteristic length L in the problem considered; and time is normalized by L^2/D_0, where $D_0 = M_0 RT$ (unit: m^2/second) is diffusivity of the Li in the electrode matrix at stress-free state. Thus, the following dimensionless quantities are defined: Li concentration $\bar{C} = \dfrac{C}{C_{\max}}$, time $\tau = \dfrac{D_0 t}{L^2}$, coordinates $\bar{X}_K = \dfrac{X_K}{L}$, $\bar{x}_i = \dfrac{x_i}{L}$, stress $\bar{\sigma}_{ij} = \dfrac{\sigma_{ij}}{C_{\max} RT}$, chemical potential $\bar{\mu} = \dfrac{\mu}{RT}$, flux $\bar{J} = \dfrac{L}{C_{\max} D_0} J$, mobility tensor $\bar{\mathbf{M}} = \dfrac{RT}{D_0}\mathbf{M}$, and other parameters $\bar{A}_0 = \dfrac{A}{RT}$, $\bar{B}_0 = \dfrac{B}{RT}$, $\bar{\kappa} = \kappa C_{\max} RT$.

Based on Eq. (2.17), the dimensionless mass conservation law becomes

$$\frac{\partial \bar{C}}{\partial \tau} + \frac{\partial \bar{J}_K}{\partial \bar{X}_K} = 0 \quad , \tag{2.22}$$

and dimensionless nominal flux is obtained from Eq. (2.20),

$$\bar{J}_K = -\bar{M}_{KL}\left\{\left[\frac{1}{1-\bar{C}} - 2\left(\bar{A}_0 - 2\bar{B}_0\right)\bar{C} + 6\left(\bar{A}_0 - \bar{B}_0\right)\bar{C}^2 + \frac{3\beta^2 \bar{C}\det\mathbf{F}\bar{\sigma}_h}{\left(1+\beta\bar{C}\right)^2}\right]\frac{\partial \bar{C}}{\partial \bar{X}_L} - \frac{3\beta\bar{C}}{1+\beta\bar{C}}\frac{\partial}{\partial \bar{X}_L}\left(\det\mathbf{F}\bar{\sigma}_h\right)\right\}, \tag{2.23}$$

2.3.2. An analogy between mass diffusion and heat transfer

The analogy between these two transport phenomena, namely mass diffusion and heat transfer, has been utilized dated back to Prussin in 1960s [182] when the coupled deformation and mass diffusion was studied, though it was for small deformation. This analogy must be carefully examined for large deformation, specifically for the implementation in ABAQUS.

The governing equation for heat transfer in ABAQUS is

$$\rho \frac{dU}{dT}\frac{\partial T}{\partial t} + \frac{\partial f_i}{\partial x_i} = r\,, \tag{2.24}$$

where ρ is the density, U is the heat energy, T is the temperature, t is the time, f_i is the true heat flux, and r is the production of heat source. It should be noted that this equation is written at current coordinates $\mathbf{x}$. However, it is by no means an Eulerian description but an updated Lagrangian description that is used when the large deformation is considered in ABAQUS.

To compare with Eq. (2.24), the mass conservation law (Eq. (2.22)) using the total Lagrangian description is expressed in the current configuration as

$$\frac{1}{\det \mathbf{F}}\frac{\partial \bar{C}}{\partial \tau} + \frac{\partial}{\partial \bar{x}_i}\left(\frac{F_{iK}\bar{J}_K}{\det \mathbf{F}}\right) = 0\,. \tag{2.25}$$

By comparing Eq. (2.24) for heat transfer and Eq. (2.25) for mass diffusion, an analogy can be made for large deformation: mass diffusion is analogical to heat transfer by the following equivalence,

$$\begin{aligned} &\bar{C} = T \\ &\tau = t \\ &\frac{F_{iK}\bar{J}_K}{\det \mathbf{F}} = f_i \\ &\frac{1}{\det \mathbf{F}} = \rho \frac{dU}{dT} \\ &r = 0 \end{aligned} \quad . \tag{2.26}$$

The mass diffusion problems then can be modeled as heat transfer problems in ABAQUS by defining temperature T as dimensionless concentration $\bar{C}$, time t as τ, true heat flux f_i as $\frac{F_{iK}\bar{J}_K}{\det \mathbf{F}}$, density of heat capacity $\rho \frac{dU}{dT}$ as $\frac{1}{\det \mathbf{F}}$, and vanishing heat source r. This specifically defined heat transfer behavior is implemented in ABAQUS via its user-defined heat transfer subroutine UMATHT.

UMATHT subroutine receives temperature T (or equivalently $\bar{C}$ in this analogy) and its spatial gradient $\frac{\partial T}{\partial x_i}$ (i.e., $\frac{\partial \bar{C}}{\partial \bar{x}_i}$) from ABAQUS and defines heat capacity per volume $\rho \frac{dU}{dT}$ (i.e., $\frac{1}{\det \mathbf{F}}$), heat flux f_i (i.e., $\frac{F_{iK}\bar{J}_K}{\det \mathbf{F}}$) and its derivatives respective to temperature $\frac{\partial f_i}{\partial T}$ and temperature gradient $\frac{\partial f_i}{\partial\left(\frac{\partial T}{\partial x_i}\right)}$.Thus in addition to the equivalence given by Eq. (2.26), the equivalence

$$\begin{aligned} &\frac{\partial f_i}{\partial T} = \frac{\partial}{\partial \bar{C}}\left(\frac{F_{iK}\bar{J}_K}{\det \mathbf{F}}\right) \\ &\frac{\partial f_i}{\partial\left(\frac{\partial T}{\partial x_i}\right)} = \frac{\partial\left(\frac{F_{iK}\bar{J}_K}{\det \mathbf{F}}\right)}{\partial\left(\frac{\partial \bar{C}}{\partial \bar{x}_i}\right)} \end{aligned} \tag{2.27}$$

also needs to be included.

This user-defined heat transfer behavior depends on deformation and stress since the deformation gradient $\mathbf{F}$ and stresses (true stress $\boldsymbol{\sigma}$ and second Piolar-Kirchhoff stress $\mathbf{S}$) appear in the equivalence (Eq. (2.26) and Eq. (2.27)), which can also be realized in UMATHT through some practical techniques. It should be noted that even the deformation gradient $\mathbf{F}$ and stresses can be passed into UMATHT, the appearance of the gradient of stress and deformation (i.e., $\frac{\partial(\det\mathbf{F}\bar{\sigma}_h)}{\partial\bar{X}_L}$ in Eq. (2.23)) makes the implementation challenging since deformation gradient and stresses are defined at the integration points, not nodal variables as displacement. Therefore, its derivatives have to be calculated via interpolation using shape functions or the pointwise least squares (PLS) method. Appendix 2A details these practical techniques to implement UMATHT.

Using this user-defined heat transfer subroutine UMATHT and existing coupled deformation and heat transfer module in ABAQUS, the coupled deformation and mass diffusion can be realized in ABAQUS. To correctly implement this numerical method, the thermal expansion in heat transfer that is analogical to the compositional expansion in mass diffusion must be reconsidered in ABAQUS as we will discuss in the next section.

2.3.3. An analogy between compositional expansion and thermal expansion

The compositional expansion and thermal expansion are all eigen deformation, in which they are analogical. In Li-ion batteries, particularly for electrodes as Si that experience large volumetric change, the compositional expansion is extremely large, such as up to 400% volumetric expansion for Si electrode, which is far beyond the small deformation range for thermal expansion. Therefore, the analogy between composition expansion and thermal expansion must be carefully reexamined regarding the numerical aspect for large deformation.

Eq. (2.8) assumes a linear compositional expansion. Using the undeformed electrode as the reference (i.e., vanishing Li concentration), at a given Li concentration $\bar{C}$ (or equivalently, temperature T using the analogy as discussed), the compositional strain is

$$\varepsilon_{compositional} = \lambda^c - 1 = \beta \bar{C}. \tag{2.28}$$

For thermal expansion, linear relation between temperature change and thermal strain is commonly used. For nonlinear problem, it is solved by dividing into many incremental steps and at each increment step, e.g., at the increment step N, the thermal strain is given by

$$\varepsilon_{thermal}^{(N)} = \alpha \Delta T^{(N)}, \tag{2.29}$$

where α is the coefficient of thermal expansion and $\Delta T^{(N)} = T^{(N)} - T^{(N-1)}$ is the temperature increment at the current increment step N with the superscript as the number of the increment. Despite that Eq. (2.28) and Eq. (2.29) are similar in formality, a simple equivalence cannot be established in the numerical method since different strain measurements are used.

The compositional strain Eq. (2.28) is based on total Lagrangian description, i.e., the strain measurement is regarding the undeformed state. However, updated Lagrangian algorithm is used in many commercial finite element package (e.g., ABAQUS), in which the reference state is not the undeformed state and every time step is treated as a problem with an infinitesimal increment in displacement. When doing that, converged coordinates from last time step is used as the reference state and a small Green strain at time step N is defined in the principle coordinates as

$$\varepsilon^{(N)} = \frac{\partial x^{(N)}}{\partial x^{(N-1)}} - 1. \tag{2.30}$$

In order to correctly express the compositional strain Eq. (2.28) as a thermal strain in ABAQUS, thermal strain must be re-defined. It could be derived from Eq. (2.30) that

$$1+\varepsilon^{(N)}=\frac{\partial x^{(N)}}{\partial x^{(0)}}/\frac{\partial x^{(N-1)}}{\partial x^{(0)}}=\lambda^{(N)}/\lambda^{(N-1)} \tag{2.31}$$

Based on this equation, the thermal strain should be defined as following

$$\varepsilon_{thermal}^{(N)}\approx\ln\left(1+\varepsilon_{thermal}^{(N)}\right)=\ln\left(1+\beta T^{(N)}\right)-\ln\left(1+\beta T^{(N-1)}\right). \tag{2.32}$$

This re-defined thermal strain is able to correctly represent the compositional strain Eq. (2.28) and can be embedded in ABAQUS via its user-defined thermal expansion subroutine UEXPAN.

2.3.4. Prescribed flux boundary condition

Prescribed flux boundary condition represents a type of important experimental process, namely, constant current during charge and discharge, or galvanostatic charge and discharge. Depending on the mass and theoretical capacity (e.g., 4,200 mAh/g for Si) of the active electrode materials, a current is pre-determined to conduct the galvanostatic charge and discharge. In the modeling, current is the applied flux of Li on the surface of electrodes. In other words, the flux is pre-determined before the deformation and thus the prescribed flux is calculated in the undeformed state. However, the updated Lagrangian algorithm in ABAQUS uses an updating state as the reference. Thus, the prescribed flux boundary condition at the undeformed state has to be re-calculated at the current state.

Starting from the conservation of total flux

$$\bar{j}da=\bar{J}dA\,. \tag{2.33}$$

Here *da* and *dA* are the areas of an element of surface after and prior to deformation, $\bar{j}$ is the flux at the current configuration to be determined, and $\bar{J}$ is the prescribed flux calculated at the undeformed reference state. Using the Nanson's formula, the deformation dependent flux at the current state is given by

$$\bar{j} = \frac{\bar{J}}{\det \mathbf{F} \sqrt{\left(N_K F_{Ki}^{-1}\right)\left(N_L F_{Li}^{-1}\right)}} . \tag{2.34}$$

Quantities involved in this expression are either accessible in ABAQUS or provided by users. A user subroutine UFLUX is utilized to implement this formula. Appendix 2A further discusses this implementation with more details.

By the implementation of the above discussed aspects, the coupled large deformation and mass diffusion in electrodes for Li-ion batteries can be rigorously realized in ABAQUS. It should be noted that a static problem with a pre-determined state of charge only needs to re-define the thermal expansion to correctly represent the compositional expansion as discussed in the Section 2.3.3, while the transient problems have to include all the aspects discussed in this section. Appendix 2B gives a benchmark the numerical methods and the involved user subroutines are available upon request to the authors. Through these examples in Appendix 2B, it is verified that each of the three user subroutines UMAT, UEXPAN, and UFLUX is properly programmed. Furthermore, in order to verify that all these subroutines work properly in a coordinated way, we set up a simple example for benchmark by comparing results using the present approach and using COMSOL Multiphysics 4.2a.

2.4. Benchmark of the Numerical Implementation

2.4.1. Material parameters and element

In our simulation, we focus on the Si electrode. All the parameters used in examples in this section are listed in Tab. 2.1.

Table 2.1. Parameters used in Section 2.2.4.

Parameters	Values
E, Young's modulus of Si	$130\ GPa$
E_p, plastic modulus of Si	$1.83\ GPa$
ν, Poisson's ratio of Si	0.3
ε_Y, yielding strain of Si	0.2%
υ, molar volume of Si	$12\times10^{-6}\ m^3/mole$
$C_{\max}$, maximum nominal Li concentration	$0.3667\times10^{6}\ mole/m^3$
R, gas constant	$8.314 J/K\cdot mole$
T, room temperature	$300K$
β, compositional expansion coefficient	0.5874
D_0, diffusivity of Li	$10^{-12}\ cm^2/s$

It is assumed that the Si anode is amorphous, as it becomes amorphous after the first cycle of charge in experiments. The phase transformation of Si anode from crystal to amorphous during the first cycle is not considered in this chapter. We assume a bilinear plastic-elastic constitutive relation for Si, as described in Section 2.2.4. For material properties in the elastic range, we refer to the literature for amorphous Si [202] with elastic modulus $E=130\ GPa$ and Poisson's ratio $\nu=0.3$. However, the material properties in the plastic range are not fully available yet so that we adopt some typical values: the yielding strain $\varepsilon_Y=0.2\%$ as a typical one for metal plasticity, and a "plastic" modulus $E_p=1.83\ GPa$ as a reasonable value to fit some experiments [181, 203].

In all user subroutines, both moduli and stresses are normalized by $C_{\max}RT$, which is estimated as follows. The volume of one mole Si atoms in solid is given by $\upsilon = \frac{M_{Si}}{\rho_{Si}} \approx 12\times10^{-6} m^3/mole$, where M_{Si} and ρ_{Si} are molar mass and density of Si, respectively. It is known that the compound with maximum Li concentration among all the possible Li/Si compounds during the electrochemical reactions is $Li_{22}Si_5$. Thus the maximum nominal Li concentration is determined by $C_{\max} = \frac{4.4}{\upsilon} = 0.3667\times10^6 mole/m^3$ and $C_{\max}RT = 0.915\ GPa$. Therefore, normalized elastic and plastic moduli are $\bar{E} = 142.15$ and $\bar{E}_p = 14.215$, which are the material parameters used in the examples presented in this chapter.

It is also known that the maximum volumetric expansion for lithiated Si is as high as 400% associated with compound $Li_{22}Si_5$ [13], which determines the coefficient of compositional expansion $\beta = 0.5874$ via $\left(\lambda^c_{\max}\right)^3 = (1+\beta)^3 = 400\%$. Since this model does not consider electrical process, the maximum capacity 4,200 mAh/g of Si does not explicitly enter the picture. The parameters A_0 and B_0 are taken to be zero as there are no meaningful reference values available.

To normalize time, the factor $t_d = \frac{L^2}{D_0}$ is estimated in the following. As listed in reference [204, 205], the diffusivity of Li in Si is $1.7\times10^{-11} cm^2/s$ and $6.4\times10^{-11} cm^2/s$ at discharge capacity of 800 mAh/g and 1,200 mAh/g, respectively (in bulk material), and $2\times10^{-10} cm^2/s$ at average discharge capacity of 1,882 mAh/g (in nano material). By extrapolating these data, it is estimated that the stress free diffusivity or the diffusivity at

vanishing Li concentration is $D_o \approx 10^{-12} cm^2/s$. Therefore, for the range of characteristic length scale $L = 10nm \sim 10\mu m$, the diffusion time ranges $t_d = 1 \sim 10^6 s$.

The physical meanings for normalized time τ and flux $\bar{J}$ are the following. In normalized time $\tau = \frac{D_o t}{L^2}$, the real time *t* has a physical meaning, such as total charge time *T*, e.g., 3,600s for 1C charge rate and 360s for 10C charge rate, respectively; *L* has a physical meaning as a characteristic length scale, such as the thickness of a Si anode. Thus, for total charge time *T*, the corresponding normalized total charge time τ_{total} becomes $\tau_{total} = \frac{D_o T}{L^2}$. For a Si anode with 100 nm in thickness (i.e., *L* = 100 nm), unit normalized total charge time (i.e., $\tau_{total} = 1$) actually means that it takes 100s to fully charge this Si anode, which provides a charge rate 36C. For the same unit normalized total charge time, it takes 10,000s to fully charge a Si anode with 1 μm in height, which corresponds to 0.36C. The nominal flux *J*, total charge time *T* and maximum nominal Li concentration $C_{\max}$ are related via

$$JAT = C_{\max} AL, \tag{2.35}$$

where *A* is the cross-sectional area in the reference state. Considering the normalized flux $\bar{J} = \frac{L}{C_{\max} D_o} J$ (discussed in Section 3.1), one obtains that

$$\bar{J}\tau_{total} = 1. \tag{2.36}$$

Thus a unit normalized total charge time is accompanied by a unit normalized flux on the Si anode. In the following simulations, without specific statement, all variables are normalized.

Quadratic brick element with temperature as an additional degree of freedom is used. Specifically, element C3D20T in ABAQUS is used throughout the simulations in this chapter. This element has 20 nodes and 27 integration points. However, any element with coupled displacement and temperature as active degree of freedom can be utilized.

2.4.2. Benchmark using a simple example

For an essentially coupled multi-field problem with large deformation, elasticity and plasticity, as described in Section 2.2, to the best of our knowledge, there is no verified numerical tool available to solve it. In order to benchmark the present numerical approach, we formulate a simple coupled problem, in which the deformation field can be explicitly determined from the concentration field. In other words, this problem is analytically decoupled and reformulated into a nonlinear diffusion problem. Therefore, this problem could be readily solved by commercial software, such as COMSOL Multiphysics through its PDE module. Meanwhile, this problem can still be treated as a coupled multi-field problem and solved by the present numerical approach. Thus, the present numerical approach is benchmarked by comparing with COMSOL Multiphysics.

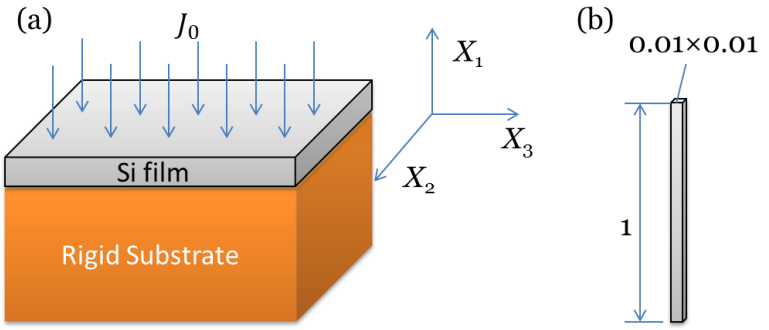

Figure 2.2. (a) Illustration of a silicon thin film on a rigid substrate lithiated by constant flux. (b) Geometry used to model the system in ABAQUS and COMSOL.

The example we consider here is illustrated in Fig. 2.2a, where an infinite large thin Si film is firmly bonded on a rigid thick substrate. A uniform lithium flux J_o is

applied from the top surface of Si thin film. The interface between Si thin film and the rigid substrate is assumed to be impermeable to lithium. A computational model shown in Fig. 2.2b is meshed into 100 (100×1×1) quadratic elements, and used for both ABAQUS and COMSOL simulation.

Appendix 2C provides details of this problem with some core equations in the following. The governing equations are given by

$$\frac{\partial \bar{C}}{\partial \tau}+\frac{\partial \bar{J}_1}{\partial \bar{X}_1}=0 \tag{2.37}$$

$$\bar{J}_1=-\left[\frac{1}{1-\bar{C}}+\frac{3\beta^2\bar{C}\lambda_1\bar{\sigma}_h}{\left(1+\beta\bar{C}\right)^2}\right]\frac{\partial \bar{C}}{\partial \bar{X}_1}+\frac{3\beta\bar{C}}{1+\beta\bar{C}}\frac{\partial}{\partial \bar{X}_1}\left(\lambda_1\bar{\sigma}_h\right) \tag{2.38}$$

with boundary conditions

$$\bar{J}_1=\bar{J}_0 \text{ at } \bar{X}_1=1$$

$$\bar{J}_1=0 \text{ at } \bar{X}_1=0$$

Where

$$\lambda_1\bar{\sigma}_h=\begin{cases}-\bar{E}\dfrac{2\bar{E}\ln\lambda_{Y0}+4\bar{E}^p\ln\left(1+\beta\bar{C}\right)}{3\bar{E}+6\left(1-\nu\right)\bar{E}^p}\left(\lambda_{Y0}\right)^{\frac{(4\nu-2)\bar{E}}{\bar{E}+2(1-\nu)\bar{E}^p}}\left(1+\beta\bar{C}\right)^{\frac{3\bar{E}+2(1+\nu)\bar{E}^p}{\bar{E}+2(1-\nu)\bar{E}^p}}, & \\ \qquad\qquad if\ \dfrac{1}{1-\nu}\ln\left(1+\beta\bar{C}\right)>\ln\lambda_{Y0} & \\ -\dfrac{2\bar{E}}{3\left(1-\nu\right)}\ln\left(1+\beta\bar{C}\right)\left(1+\beta\bar{C}\right)^{\frac{1+\nu}{1-\nu}}, & \\ \qquad\qquad if\ \dfrac{1}{1-\nu}\ln\left(1+\beta\bar{C}\right)\le\ln\lambda_{Y0} & \end{cases} \tag{2.39}$$

Results from COMSOL and ABAQUS are plotted in Fig. 2.3. From Fig. 2.3a-d, normalized lithium concentration, total logarithm strain and logarithm plastic strain along thickness direction, and the in-plane true stress solved from COMSOL and ABAQUS are plotted at different state of charges (SOCs), respectively. It is shown that

the two sets of solutions from independent approach agree very well with each other. Thus the numerical implementation embedded in ABAQUS as described in Section 2.3 is benchmarked.

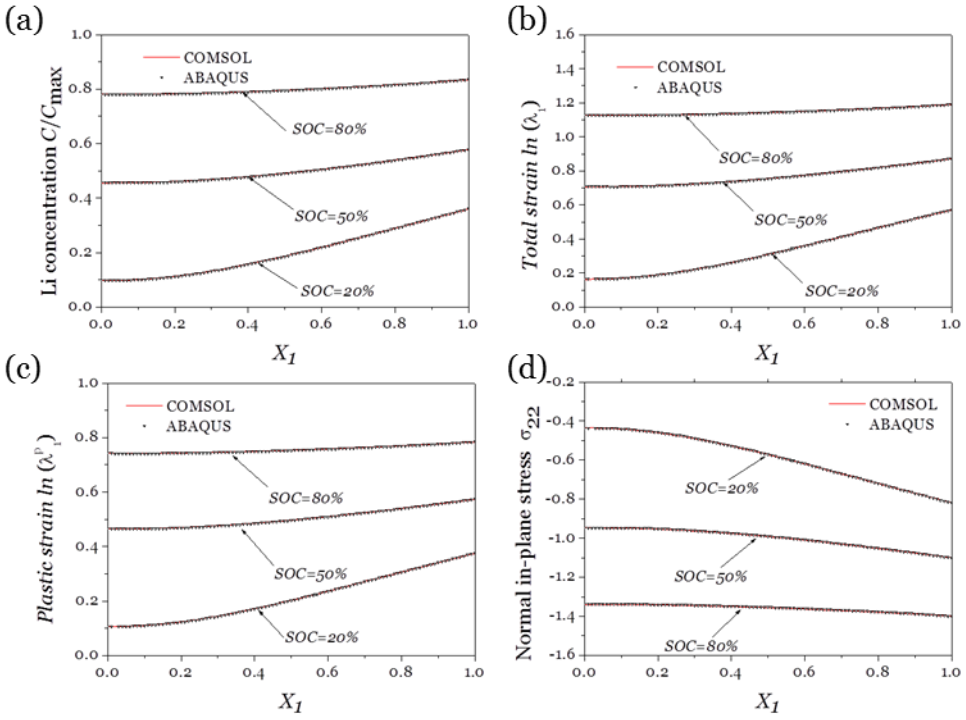

Figure 2.3. Comparison between the results obtained from the present approach via ABAQUS and COMSOL Multiphysics 4.2: (a) normalized concentration, (b) total logarithm total strain in the thickness direction, (c) logarithm plastic strain in the thickness direction, and (d) true in-plane normal stress in the thickness direction at different state of charge (SOC), 20%, 50%, and 80%, respectively.

2.5. Practical Examples – Capabilities and Implications

To demonstrate the capability of the present numerical approach, we study two cases with more practical significance in this section. Fig. 2.4a shows the problem that we are studying, in which an array of Si patches is patterned as anode materials on a copper substrate as the current collector. The configuration of patterned Si patches on substrate has already been used in experiments [206].

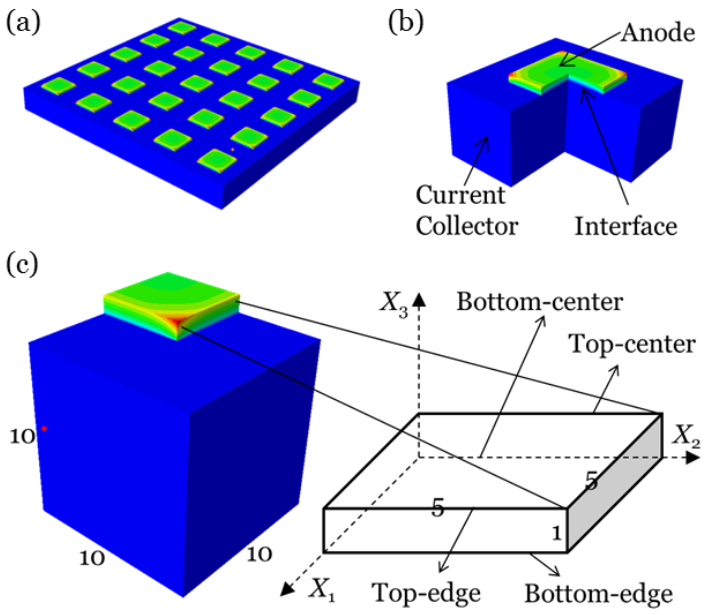

Figure 2.4. (a) Illustration of an array of silicon patches on copper current collector. (b) A representative unit. (c) A quarter unit used in the finite element simulations with four representative lines defined.

2.5.1. Firmly or compliantly bonded Si on current collector

In this section, we study two cases for different bonding between Si and the current collector. One is that Si is directly and firmly bonded with the current collector and the other one is that there is a compliant and conductive binder between Si and the current collector. In finite elements simulations, the above difference is reflected by the different treatment on the interface between Si and the current collector, as shown in a representative unit cell of this periodical structure in Fig. 2.4b consisting of anode, current collector, and the interface. We only study a quarter of the unit as shown in Fig. 2.4c by applying the symmetric boundary conditions. Also because of the symmetry, four representative lines in the quarter of the unit, namely top-edge, top-center, bottom-edge, and bottom-center are focused in these two cases. All additional parameters used in this section are listed in Tab. 2.2.

Table 2.2. Parameters used in Section 2.5.

Parameters	Values
E_{Cu}, Young's modulus of Cu	$110GPa$
ν_{Cu}, Poisson's ratio of Cu	0.34
ε^{pl}, equivalent plastic strain for damage initiation in Si	10%
u^{pl}, maximum plastic displacement for total failure in Si	six times of element size
K_T, tension rigidity of compliant binder	$15GN/m$
K_S, shear rigidity of compliant binder	$5GN/m$
E_{Cr}, Young's modulus of Cr	$279\ GPa$
G_{Cr}, shear modulus of Cr	$115\ GPa$
$\varepsilon_n^0, \varepsilon_s^0, \varepsilon_t^0$, normal, shear, transverse strain for damage initiation in binder and crack	1%
$\varepsilon_n^{\max}, \varepsilon_s^{\max}, \varepsilon_t^{\max}$, normal, shear, transverse strain for total failure in binder and crack	10%

In finite element simulations, the current collector copper is modeled as a linear elastic material with Young's modulus $E_{Cu} = 110GPa$, and Poisson's ratio $\nu_{Cu} = 0.34$, by using typical values. The dimension of copper is 10×10×10, meshed into 8,000 (=20×20×20) C3D8R elements. The bottom of the copper ($X_3 = -10$) is fixed and the symmetric boundary conditions are applied on its side surfaces.

The Si anode has the same mechanical properties as discussed in the section 2.4.1 besides the damage of Si is considered here. Due to the lack of experimental data on the damage behavior of Si and the main point of this section is to demonstrate the capability of the present numerical approach rather than to discuss quantitative physics, here we adopt a simple damage model that is commonly used for metals. We assume that the damage is initiated when the equivalent plastic strain ε^{pl} reaches a threshold ($\varepsilon^{pl} = 0.1$ in these two cases). Once the damage is initiated, the modulus of Si is subjected to a linear degradation described by the accumulated damage. The evolution of the damage is

driven by plastic displacement and the failure criterion is the maximum plastic displacement u^{pl} ($u^{pl}=6$ in these two cases). The dimension of Si is 5×5×1, meshed into 20×20×4 C3D20T elements. A constant flux is applied on the top surface of Si.

The interface between Si and current collector is treated differently in two cases. The firmly bonded case is realized by "tie" constraint in finite element simulations. The compliant binder between Si and current collector is realized by cohesive elements in ABAQUS. Specifically, we use zero thickness cohesive elements to model the contacting area of 5×5, meshed into one layer of 741 COH3D8 cohesive elements. The traction separation relation is used to model the cohesive elements. The tension rigidity $K_T=15GN/m$, and shear rigidity $K_S=5GN/m$ are used, corresponding to a linear material with normalized modulus $\bar{E}_{binder}=15$ and Poisson's ratio $\nu_{binder}=0.5$. For the sake of simplicity of simulations, element elimination is not considered here.

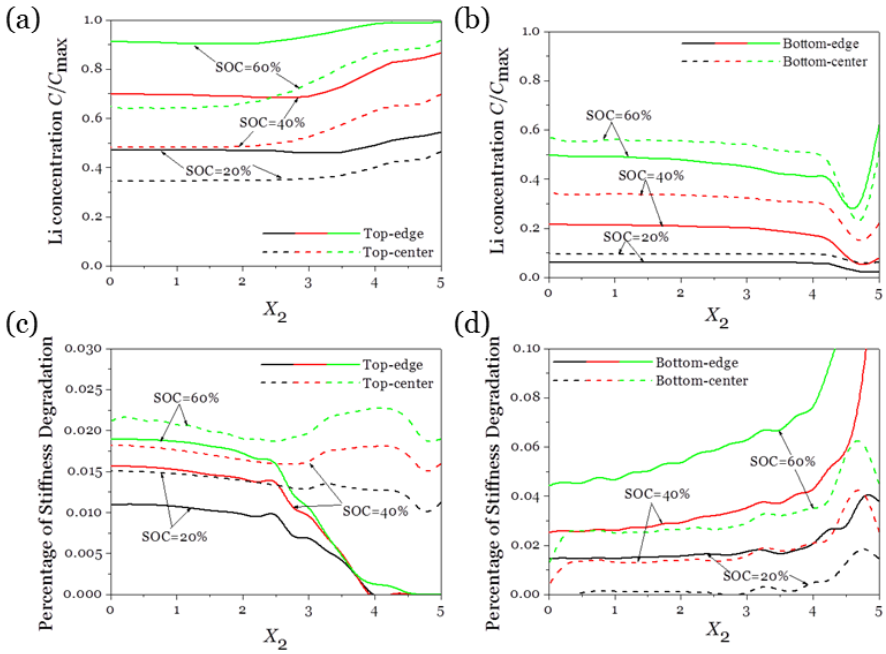

Figure 2.5. Profiles of normalized lithium concentration (C/C_{max}) (a and b) and percentage of stiffness degradation (c and d) in X_2 direction along four representative

lines at different state of charge (SOC), respectively. The interface between Si and the current collector is firmly bonded.

Fig. 2.5 provides the profiles of normalized Li concentration ($C/C_{\max}$) and the percentage of the stiffness degradation in X_2 direction along four representative lines for different SOCs. Fig. 2.5a showes that the Li concentration is higher at the outer ($X_2 = 5$) than the inner ($X_2 = 0$) on both top-edge and top-center lines since the outer is more free and less constrained and thus the Li is easier to diffuse in. As going from top-edge to top-center, it is found that the difference in Li concentration from the outer to the inner increases and the absolute value of the Li concentration decreases for the same reason of constraints. The center of the top-edge ($X_2 = 0$) and the edge of the top-center ($X_2 = 5$) occupy the same situation, i.e., with two free surfaces; thus they show the same Li concentrations. For example, normalized Li concentration is 0.91 for the center of the top-edge ($X_2 = 0$) and the edge of the top-center ($X_2 = 5$) when SOC = 60%. Because the relatively free for the top surface, the percentage of stiffness degradation is low (only a few percent), as shown in Fig. 2.5c. Near the edge of the top-edge ($X_2 = 5$), there is even no degradation. This suggests a critical size that below this size, the degradation can be avoided on the top surface.

Compared with Fig. 2.5a where Li concentrations show significant difference between the edge and center, the Li concentrations for the bottom surface, i.e., bottom-edge and bottom-center as in Fig. 2.5b, show less difference, which is resulted from the strong constraints at the bottom. Freedom in the lateral direction at the bottom-edge does not provide too much advantage in the stress relaxation. The absolute value of the Li concentration on the bottom as a whole is lower than that on the top for the same SOCs. Fig. 2.5d shows the percentage of stiffness degradations at the bottom-edge and

bottom-center. As we can see, a significant degradation is observed on bottom-edge. Due to the stress concentration at the edge of the bottom-edge ($X_2 = 5$), the degradation is even higher, such as over 20% for SOC = 60% according to numerical results (truncated in the figure). Due to the lack of stress concentration at the bottom-center, the percentage of stiffness degradation is not very high, on the order of a few percent. These results indicate that the bonding between Si and the current collector is a critical point of failure and the failure may start from the corner of the electrode. The solutions to avoid or delay fracture may include electrodes without corners (e.g., round pillar) or compliant binders as to be discussed in the following.

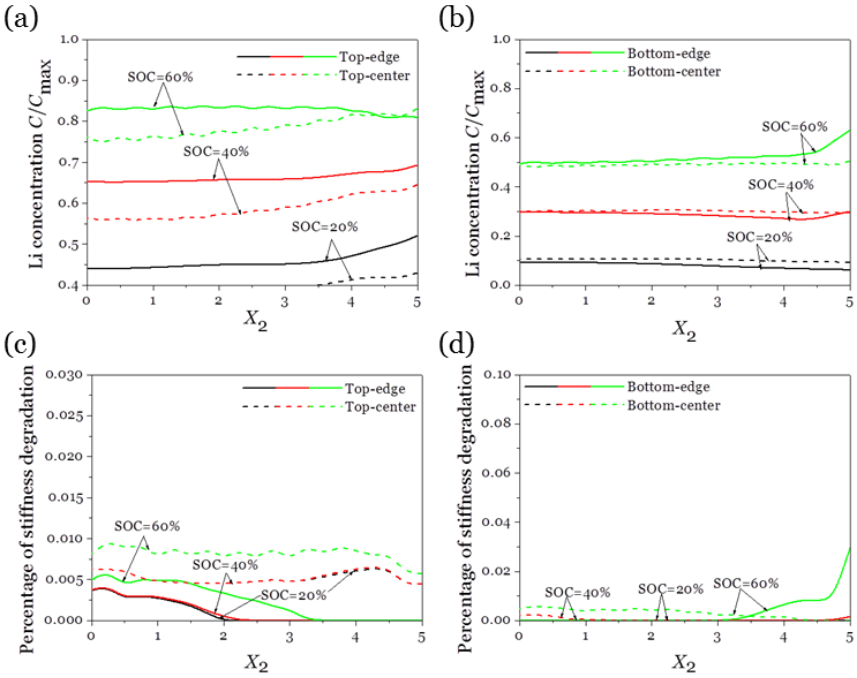

Figure 2.6. Profiles of normalized lithium concentration (C/C_{max}) (a and b) and percentage of stiffness degradation (c and d) in X_2 direction along four representative lines at different state of charge (SOC), respectively. The interface between Si and the current collector is compliant binder. To compare with the stiffness degradation shown in Fig. 2.5c and Fig.2.5d, the same scale is used.

When the bonding between Si and current collector is changed from firmly bonded to elastic binder, the results are very different as shown in Fig. 2.6, which provides the profiles of normalized Li concentration ($C/C_{\max}$) and the percentage of the stiffness degradation in X_2 direction at four representative lines for different SOCs. Fig. 2.6a shows that the Li concentration is relatively uniform along both top-edge and top-center, which is very different from the obvious nonuniformly distributed Li shown in Fig. 2.5a. The explanation is that the elastic binder reduces the constraint to the Si anode from the current collector; thus the stress level and its gradient are lower than the case with firmly bonded interface. Without the stress and its gradient as driving force for diffusion, diffusion in X_2 direction thus does not exhibit apparent difference. It is also found from Fig. 2.6a that the Li concentration at the top-edge (solid line) is overall higher than that at the top-center (dashed line) since the top-edge is less constrained. Again, the center of the top-edge ($X_2 = 0$) and the edge of the top-center ($X_2 = 5$) occupy the same situation, i.e., with two free surfaces; thus they show the same Li concentrations. Because the Si is relatively free when the elastic binder is used, the percentage of stiffness degradation for both top-edge and top-center as in Fig. 2.6c is much smaller than that in the case of firmly bonded (Fig. 2.5c). The percentage of stiffness degradation is on the order of 1%. This result suggests that elastic binder can significantly reduce the mechanical degradation of Si anode by creating a more “free’ situation to let Si expand during electrochemical reactions. Thus the cyclic retention can be improved.

Compared with the Li concentration given by Fig. 2.6a for the top surface, the Li concentrations for the bottom surface, i.e., bottom-edge and bottom-center in Fig. 2.6b, show similar relatively uniform distribution in X_2 direction, which is resulted from stress

relaxation at the bottom. The absolute value of the Li concentration on the bottom as a whole is lower than that on the top for the same SOCs. As shown in Fig. 2.6d, the percentage of stiffness degradation on the bottom surface is much smaller than the case for firmed bonded interface but larger than that on the top surface, because of more constraint on the bottom.

By comparison between the results for firmly bonded interface and elastic binders as interface, it seems to suggest that the elastic bonding is able to help to homogenize the concentration distribution and mediate the electrode damage, which makes us believe that the cyclic retention of Li ion batteries can be greatly improved. In fact, the elastic binders [207] or similarly elastic substrates [180] have been used in recent experiments and very good cyclic retention has been realized.

2.5.2. Si bonded on current collector with multiple failure mechanisms

There are two limitations of the cases presented in Section 2.5.1. First, the failure of binders is not considered. Second, Si anodes are assumed intact before lithiation, which does not hold as there are some flaws serving as the sites for stress concentration. The interaction between the failure of binders and flaws of Si anodes may provide a variety of failure mechanisms in the anode-binder-collector assembly. In this Section, the interplay between different failure mechanisms is studied.

To fulfill the failure in the anode-binder-collector assembly, two modifications are employed in Fig. 2.4. First, the failure behavior of the binder that is modeled as a layer of cohesive element is now considered through stiffness degradation. The stiffness degradation is initialized when the nominal strain (either normal strain ε_n, shear strain ε_s, or transverse strain ε_t) reaches a critical values, ε_n^0, ε_s^0, or ε_t^0, respectively. A linear damage evolution is assumed and the binder fails completely when the nominal strain

reaches the maximum values, $\varepsilon_n^{\max}$, $\varepsilon_s^{\max}$, or $\varepsilon_t^{\max}$. In this Section, the binder is assumed to be Chromium, which is a widely used adhesive material for Si and Cu. The traction-separation relation is given based on Young's modulus and shear modulus of Chromium, $E_{Cr} = 279\ GPa$, $G_{Cr} = 115\ GPa$. For simplicity, the criteria for damage initiation is taken as $\varepsilon_n^o = \varepsilon_s^o = \varepsilon_t^o = 1\%$ and that for failure is $\varepsilon_n^{\max} = \varepsilon_s^{\max} = \varepsilon_t^{\max} = 10\%$. 2,500 (=50×50×1) COH3D8 elements are used to model the cohesive layer with 0.1 in thickness. Second, two pre-existing planar cracks are placed in the symmetrical planes of Si anode, i.e., in X_1X_3 and X_2X_3 planes, which are also modeled as cohesive elements with vanishing thickness. The traction-separation relation is used for these cohesive elements based on the property of Si. Similar damage initiation and evolution rules are used with $\varepsilon_n^o = \varepsilon_s^o = \varepsilon_t^o = 1\%$ and $\varepsilon_n^{\max} = \varepsilon_s^{\max} = \varepsilon_t^{\max} = 10\%$. 500 (=50×10×1) COH3D8 elements are employed to model each pre-existing crack.

A series of lithiation and delithiation simulations are conducted. Fig. 2.7 shows the contour plots of percentage of stiffness degradation for the two pre-existing cracks and binder at different states of lithiation and delithiation. Fig. 2.8 shows the overall deformation of the Si-binder-collector system at three lithiation/delithiation states listed in Fig. 2.7. Before lithiation starts, cracks and binders are not damaged as shown in Fig. 2.7a where all elements are in blue. During lithiation (Fig. 2.7a-f), damage mainly occurs in the binder and increases monotonically as lithiation. At 90% lithiation (Fig. 2.7f), the majority of binder has been damaged.

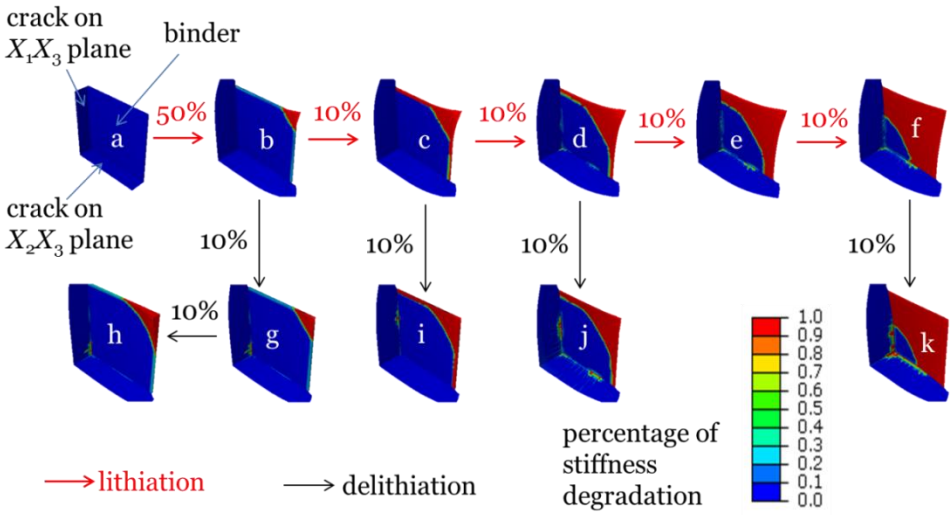

Figure 2.7. Contour plots of percentage of stiffness degradation in binder and pre-existing cracks at different degree of lithiation ((a)-(f)) and delithiation ((g)-(j)).

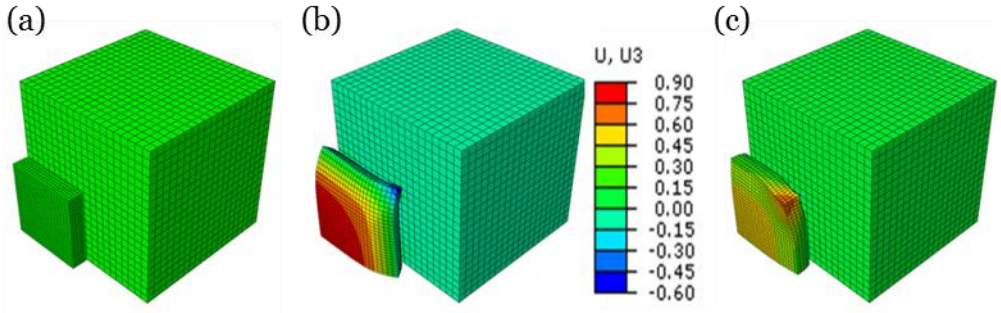

Figure 2.8. Morphology of the silicon-binder-collector at selected degree of lithiation/delithiation: (a) initial state, (b) lithiation state corresponding to Fig. 2.7b, and (c) delithiation state corresponding Fig. 2.7h.

The failure of the binder is attributed to the shear between Si patch and copper substrate, which can be observed in Fig. 2.8. Fig. 2.8a shows the Si-binder-collector assembly before lithiation and Fig. 2.8b is for the assembly at 50% lithiation. It is obvious that the area of the Si patch increases significantly upon lithiation and bends towards current collector due to the constraint from it, which leads to great sliding at the interface between the Si patch and the substrate. As observed from Fig. 2.7b, the failure zone initializes from the corner of the binder where the largest sliding occurs. It is also

observed that there is no significant failure in the pre-existing cracks during lithiation since the Si patch is subjected to compressive stress caused by the compositional expansion and constraint from the collector. Fig. 2.7g-k show the delithiation processes. It is interestingly found that there is still no significant failure in the pre-existing cracks no matter from which state the delithiation starts, at least for 10% and 20% delithiation. This surprising observation is because once the binder is damaged during lithiation, the Si patch above the damaged binder can deform freely and thus "peeling-off" occurs, which can be seen in Fig. 2.8c. Fig. 2.8c corresponds to the state of delithiation given by Fig. 2.7h, in which the corner of the binder has been completely damaged. Therefore, upon delithiation, Si patch bends against the current collector as a response to the compositional contraction, which leads to compressive stress on the pre-existing cracks and thus prevents damages in the pre-existing cracks. On the other hands, the "peeling-off" further damages the binder, which is tension controlled and different from the sliding during lithiation.

The results in this section seem to imply that the introduction of damage in some areas of the binder in a controllable way could prevent the damage of the active materials. It should be noticed that some parameters (particularly the damage initiation and evolution parameters) are not available yet and chosen in a somewhat arbitrary way. Thus this Section mainly shows the capability and potential of the present numerical approach.

2.6. Concluding Remarks

In this chapter, we develop a finite element based numerical method to study the coupled large deformation and diffusion of electrodes in Li ion batteries under the framework of ABAQUS. The coupling is realized by an analogy between diffusion and

thermal transfer in ABAQUS. Due to the large deformation, this analogy is carefully examined and the corresponding relation is established. It is found that this formulation is able to realize the coupled deformation and diffusion in large deformation using several user-defined subroutines in ABAQUS, namely user-defined thermal transport (UMATHT), user-defined flux (UFLUX) and user-defined expansion (UEXPAN). Because the present formulation does not involve any element development in ABAUQS, many built-in modules can be directly utilized. A system comprising three components, namely, Si electrode, binder, and current collector, is studied using the cohesive elements and the damage of the electrode is considered. It is anticipated that this formulation is able to model many coupled large deformation and diffusion problems in electrodes with complex spatial and temporal conditions, such as damage evolution, fracture, and electrodes/binder delamination, among others. When this formulation is combined with experimental work, it is expected that the constitutive relations (e.g., stress versus SOC) can be extracted from various techniques, such as micro-indentation.

We here have to emphasize again that the results presented in this chapter by no means intend to explain the real mechanisms occurred in the electrodes during electrochemical reactions. The main point of this chapter is to examine a rigorous implementation of coupled deformation and diffusion through a commonly used coupled deformation and heat transfer when the extremely large deformation presents. When the theoretical model is changed, the implementation can be revised correspondingly. However, since the major field variables have been used in the present implementation, such as stress, deformation gradient, concentration and their gradient, the modification of the implementation is fairly straightforward.

CHAPTER 3

ANISOTROPIC INTERFACE REACTION AND GEOMETRY DESIGN OF NANO ELECTRODES

The first lithiation of crystal silicon is known involving huge volume expansion, plastic flow of material, electrochemical amorphization of crystal structure, and mass diffusion of lithium ions. Recent in situ TEM experiments and first-principles simulations have both revealed the existence of the sharp interface during this process and quantified the orientation dependence of the interface velocity. In this chapter, we assume interface controlled kinetics for electrode with nano size, propose an anisotropic solid reaction model for the first lithiation of crystal silicon, in which the orientation dependent interface velocity is constructed by both adopting the interface velocities measurable in experiments and taking into account the requirement from crystallographic symmetry. This three dimensional continuum model has the merit of being coherent in formulation and parameterized with clear physical background, compared to existing models. The concurrent anisotropic interface motion and large plastic flowing are simulated by implementation of this model in commercial finite element package. Exemplary results on popular nano electrode structures uncover interesting phenomena such as the formation of faceted crystal core and plastic necking in particular directions, and are compared with experiments on the same subjects. Based on the insight obtained through these examples, we propose a new principle for the geometry design of silicon electrode, and demonstrate the benefits both in 2D and 3D electrode structures.

3.1. Introduction

The rapidly increasing demand in the ever-spreading applications of lithium (Li) ion batteries (LIBs) in portable electronics, electrical/hybrid vehicles, and storage devices in smart grid for green energies, calls for the development of electrode materials with significantly improved performance on the energy density, the power density, and the life span [174, 175, 208]. As one of the Li-alloying electrode materials in LIBs, silicon (Si) has attracted a great deal of interest in recent years [13, 25, 54], due to its much larger volumetric and gravimetric Li storage capacity than Li-intercalation materials [209], including graphite and $LiFePO_4$ in commercial LIB [10, 79]. To avoid the problem of mechanical failure caused by the huge volume change commonly seen in Li-Alloying electrode [82], various approaches for design of Si electrode have been explored [210], such as improving the interaction between active Si and other electrode components [211], and engineering silicon nanowires and nanoparticles [157]. Additionally, a great deal of effort has been focused on the experimental characterization of the lithiation behavior of crystal Si [21, 26, 30, 36]. It has been repeatedly shown that the first lithiation of nano crystal Si exhibits very strong anisotropy, such as the dumbbell shape along the <112> orientation in lithiated Si.

The anisotropic lithiation behavior has been studied through atomic and continuum approaches [36, 39, 40]. For the continuum models, specialized numerical techniques are employed such as anisotropic lithiation induced strain [36], and orientation-dependent interfacial diffusivity [39], and successfully reproduced the anisotropic morphology of silicon nano wires/pillars with particular orientations. However, these models bear some intrinsic limitations that hinder them applications to more general case. For the anisotropic lithiation-induced strain model [36], particular

values of anisotropic lithiation strain were assigned in <110> and <111> directions to recreate the dumbbell shape of the lithiated <112>. This practice is unclear in physical picture as the lithiated silicon is known to be amorphous and no local orientations in that material. For the orientation-dependent interfacial diffusivity model [39], an artificial thin layer with orientation dependent diffusivity, $D^F_{<110>} \approx 6D^F_{<100>} \approx 60D^F_{<111>}$, is used in order for this model to capture the anisotropic interface velocity. Despite the unclear physical picture of this treatment, and inevitable inconsistency when interfacial diffusivity is interpolated for other directions, the arbitrariness of the parameters in the model makes the time scale lose physical significance, which is not desired for simulation of kinetic process.

To overcome the limitations the aforementioned models suffer, a new continuum anisotropic interface reaction model is developed in the present chapter, which is substantiated in physical pictures, and self-consistent in formulation. Thanks to the recent in situ TEM imaging of lithiated silicon nanowire [40] and first-principles calculations on reactive energy barrier for lithiation of silicon in different crystal orientation [136], the lithiation behavior of crystal silicon is depicted at atomic scale, and the development of such a model is made possible.

3.2. Model Description

When crystal Si (*c*-Si) is lithiated electrochemically as shown in Fig. 3.1, Li ions in the electrolyte enter and alloy with the Si, forming a layer of amorphous Li_xSi alloy (*a*-LixSi) on the surface of *c*-Si. Thus two interfaces are developed during electrochemical lithiation. One interface is formed at the *a*-Li_xSi and *c*-Si interface (ACI), and the other is at the *a*-Li_xSi and electrolyte interface (AEI). During lithiation, Li ions are continuously

provided, *c*-Si is lithiated to *a*-Li_xSi, propagating the ACI inwards. On the contrary, due to the volume expansion of Si upon lithiation, the AEI propagates outwards. The evolution of AEI determined mainly by coupled mass diffusion and lithiation assisted plasticity in a-LixSi has been widely examined [147, 153, 190]. In this chapter, we will develop a new model to describe the evolution of ACI by considering the effect of anisotropy of *c*-Si.

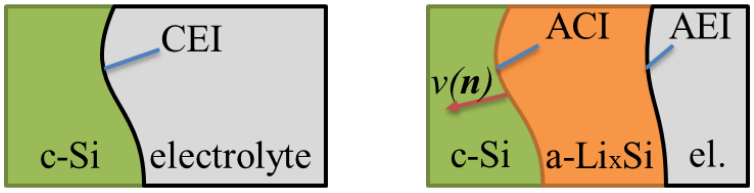

Figure 3.1. Illustration of three interfaces, CEI, ACI, and AEI.

At the ACI, a solid chemical reaction occurs to convert *c*-Si into *a*-Li_xSi, formulated in $xLi^+ + xe^- + Si \rightarrow Li_xSi$. As pointed out by Cui *et al* [148], the velocity of ACI in its normal direction is given by $v = V_m R_s$, where V_m is the molar volume of *c*-Si, and R_s is the rate of interfacial chemical reaction [unit: mole/(area×time)]. The theory of chemical kinetics [212, 213] states that the rate of interfacial reaction R_s is given by $R_s = k[Li^+]^l[e^-]^m[Si]^n$, where *k* is the rate constant, quantities inside the square bracket [...] represent the concentrations of all reactants (i.e., Li^+, e^-, and Si), and l,m,n are the reaction orders depending on reaction mechanism. As revealed by first-principles calculation [136], the rate constant k is associated with the orientation dependent reactive energy barrier $E_a(\mathbf{n})$ through Arrhenius relation, i.e., $k = A\exp(-E_a / RT)$, where A is the frequency factor, R is gas constant, T is absolute temperature. Here $\mathbf{n}$ is the normal vector of the ACI, and related to the Miller index (hkl) of the crystal side

of the interface through $\mathbf{n}=(n_1,n_2,n_3)=(h,k,l)/\sqrt{h^2+k^2+l^2}$. Thus the rate constant k depends on orientation and so does the velocity of ACI.

Without taking into account the process at the Solid Electrolyte Interfaces (SEIs), there are two competing kinetic mechanisms in the lithiation of Si, namely, Li ion diffusion controlled kinetics through the bulk a-Li_xSi, and the solid state chemical reaction controlled kinetics at the ACI [29, 148]. The rate of mass diffusion of Li ion through a-Li_xSi is characterized by diffusivity of Li, D [unit: length^2/time]; while the rate of solid chemical reaction is described by velocity of ACI, v [unit: length/time]. The ratio of the two quantities gives an characteristic length, $a_c=\frac{D}{v}$. When the characteristics length of the electrode is much greater than a_c, the kinetics of lithiation is controlled by mass diffusion. On the other hand, when the characteristic length of the electrode is much smaller than a_c, the kinetics of lithiation is mostly controlled by the interface reaction. The representative values [40, 138, 214] are $D=1\times10^{-12}cm^2/s$, and $v_{\max}=5nm/\min$, which gives approximately $a_c=1\mu m$. This chapter focuses on conductive nano Si electrode with characteristics size $a<<a_c$, in which the diffusion of Li and conduction of electron are both fast enough that the influence of concentration on reaction rate is assumed constant at the ACI. As a result, the velocity of ACI exclusively depends on its local orientation, i.e., $v=v(\mathbf{n})$.

The cubic symmetry of crystal Si imposes some requirements on the specific expression of $v=v(\mathbf{n})$. Various approaches can be employed to construct the expression to satisfy the symmetry requirements, such as Cubic Harmonics [215] or some polynomials [216]. In our model, similar to the polynomial method [216], the velocity of

ACI is expanded into a polynomial form of three invariants (I_1, I_2, and I_3) of the normal vector $\mathbf{n}$, as $v(\mathbf{n}) = A_1 I_1 + A_2 I_2 + A_3 I_3 + A_4 I_2^2 + \ldots$, following the invariant theory [217, 218]. The definitions of these invariants and their values in directions of interest are listed in Tab. 3.1. In a spherical system as defined in Fig. 3.2a, $\mathbf{n} = (\cos\theta\cos\varphi, \cos\theta\sin\varphi, \sin\theta)$. Three surfaces defined by $r = I_{1,2,3}(\theta,\varphi)$ are plotted (Fig. 3.2b-d) to illustrate the directional dependence of the three invariants.

Table 3.1. Miller index, directional vector, and definitions of the three invariants and their values in representative directions.

$<hkl>$	$<100>$	$<110>$	$<111>$	$<112>$
(n_1, n_2, n_3)	$(1,0,0)$	$\left(\frac{1}{\sqrt{2}}, \frac{1}{\sqrt{2}}, 0\right)$	$\left(\frac{1}{\sqrt{3}}, \frac{1}{\sqrt{3}}, 1\right)$	$\left(\frac{1}{\sqrt{6}}, \frac{1}{\sqrt{6}}, \frac{2}{\sqrt{6}}\right)$
$I_1 = n_1^2 + n_2^2 + n_3^2$	1	1	1	1
$I_2 = n_1^2 n_2^2 + n_2^2 n_3^2 + n_3^2 n_1^2$	0	1/4	1/3	1/4
$I_3 = n_1^2 n_2^2 n_3^2$	0	0	1/27	1/54

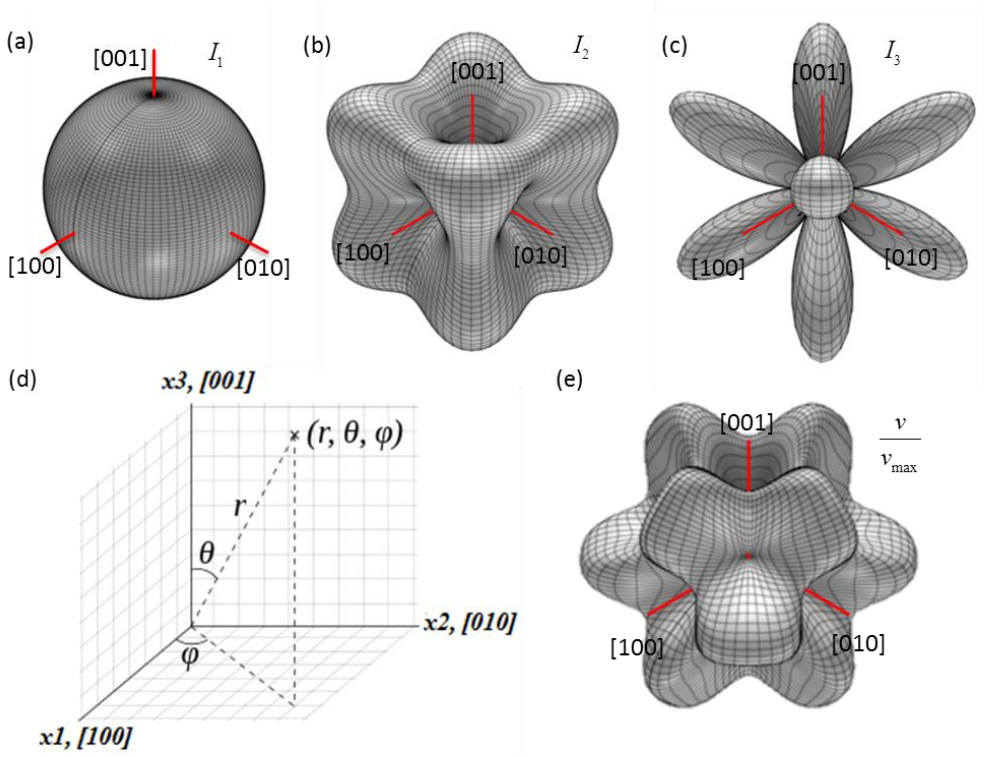

Figure 3.2. Surfaces defined in a spherical coordinate system (d) by (a) $r = I_1(\theta,\phi)$; (b) $r = I_2(\theta,\phi)$; (c) $r = I_3(\theta,\phi)$, showing the directional dependence of three invariants; (e) $r = v(\theta,\phi)/v_{\max}$, showing directional dependence of the ACI velocity for parameter $\eta = 1/6$.

The *in-situ* experiments of the first electrochemical lithiation of Si nanowire [40] have found that the velocity of ACI in <111> directions is vanishingly small and that in <110> directions reaches maximum, about 3-5 nm/min. Based on the experimental observations, the velocities of ACI along different orientations are assumed as: i. $v_{<111>} = v_{\min} = 0$; ii. $v_{<110>} = v_{\max}$; iii. $v_{<100>} = \eta v_{\max}$ with $0 \le \eta \le 1$. Here the subscripts in < > indicate orientations, and "min"/"max" represent minimum and maximum, respectively. These assumptions are in consistence with other models [21, 26, 30, 36]. Using these

assumptions, $v(\mathbf{n})$ is described by a fourth order polynomial expansion, $v = v_{\max}\left(1-16(1-\eta)\left(I_2-\frac{1}{4}\right)^2-3(8+\eta)I_3\right)$. Here the parameter η can be used to tune the velocities of ACI in other directions. For example, the surface defined by normalized velocity of ACI $r = v(\mathbf{n})/v_{\max}$ for $\eta = 1/6$ is plotted in a spherical system as in Fig. 3.2e.

3.3. Numerical Implementation

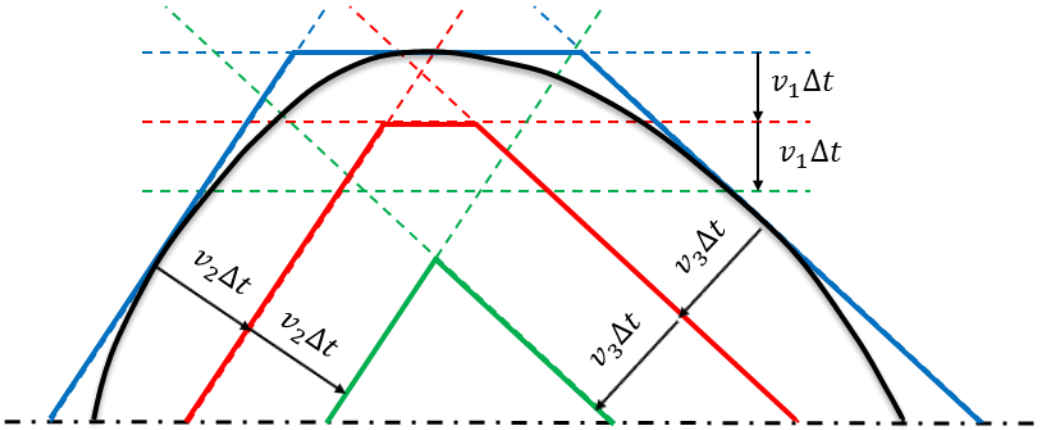

Figure 3.3. Illustration of the evolution of ACI when numerical implemented.

Once the velocities of ACI are explicitly constructed as functions of orientations, the evolution of ACI can be readily determined by moving the ACI positions based on the assumed ACI velocity. As illustrated in Fig. 3.3, the initial ACI position or equivalently the original boundary of the *c*-Si electrode is described by a curve (for 2D, or curved surface for 3D), as represented by a solid black line. Many tangential lines (i.e., solid blue lines) are used to approximate this curve. In order to accurately describe a curve, high resolution of tangential lines have been used. For example in the following analysis, 360 lines and 360×180 planes are used for 2D and 3D cases, respectively. Each tangential line has distinct normal direction and thus may have different ACI velocity. As

lithiation proceeds, these planes move inwards and the updated positions are determined by the ACI velocity and the lithiation time, as shown by the red dashed lines in Fig. 3.3. As each plane may have different ACI velocity, the position of ACI at the each time step is determined by the minimum envelop, such as that shown by the solid green lines in Fig. 3.3. With the position of ACI updated as function of lithiation time, the normalized Li concentration $\bar{c} = c / c_{\max}$ with value $\bar{c} = 0$ is assigned inside the envelope for *c*-Si phase due to the small solubility of Li in *c*-Si, and $\bar{c} = 1$ outside the envelop for *a*-Li_xSi by assuming saturation. An artificial ultrathin layer across the ACI is employed for a smooth transition. We used the commercial software ABAQUS to implement this process based on an simple and robust algorithm, which is different from other techniques for moving boundary problem such as fast matching method/level set method [219], or phase field method [151, 220-222]. ABAQUS user subroutine UTEMP is used to describe the Li concentration and UEXPAN is employed to characterize the lithiation induced volumetric expansion in *a*-Li_xSi, under rigorous large deformation description (detailed discussion is provided in the previous work [153]). *c*-Si is modeled as linear elastic material with Young's modulus $E_c = 130GPa$ and Poisson's ratio $\nu = 0.28$. *a*-Li_xSi is modeled as perfect elastic-plastic material with Young's modulus $E_a = 12GPa$, Poisson's ratio $\nu = 0.28$, and yielding stress $Y = 0.5GPa$ for simplicity, as suggested by previous work [28, 137, 223]. The mechanical constitutions of *c*-Si and *a*-Li_xSi are implemented by ABAQUS build-in modules with the concentration dependent properties. Here typical values are chosen from literature [170, 223, 224]. Material properties are interpolated between values of *c*-Si and *a*-Li_xSi for intermediate Li concentration at the artificial thin layer for smooth transition. ABAQUS/Standard is used as the nonlinear

plastic-elastic solver with the nonlinear geometry option turned on for large deformation problem.

3.4. Results and Discussion

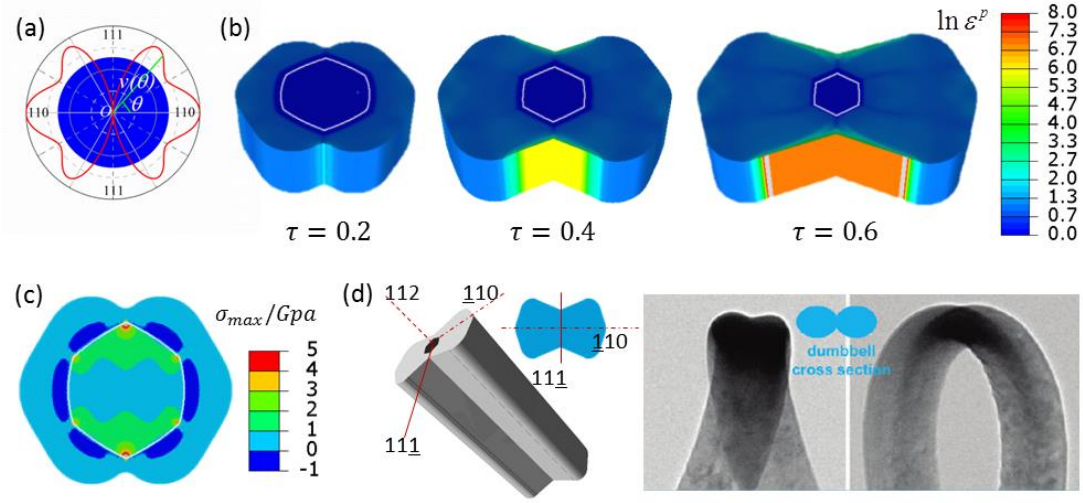

Figure 3.4. Lithiation of <112> crystal nanowire with circular cross-section. (a) Distribution of interface velocity $v(\theta)$ along different interface directions with angle θ from [110] crystal direction. Blue circle is the initial cross-section geometry. (b) Snapshots of nanowire morphologies, and interface profiles (white solid line), and colormaps of equivalent plastic strain at different normalized lithiation time τ = 0.2, 0.4, 0.6. (c) Colormap of maximum in-plane stress over the nanowire cross-section at time τ = 0.2. (d) Comparison of the simulated morphology of <112> nanowire (left panel) with the reported TEM observation of the anisotropic swelling of <112> nanowire from literature [36] (right panel) . Dumbbell cross section is successfully captured by our simulation.

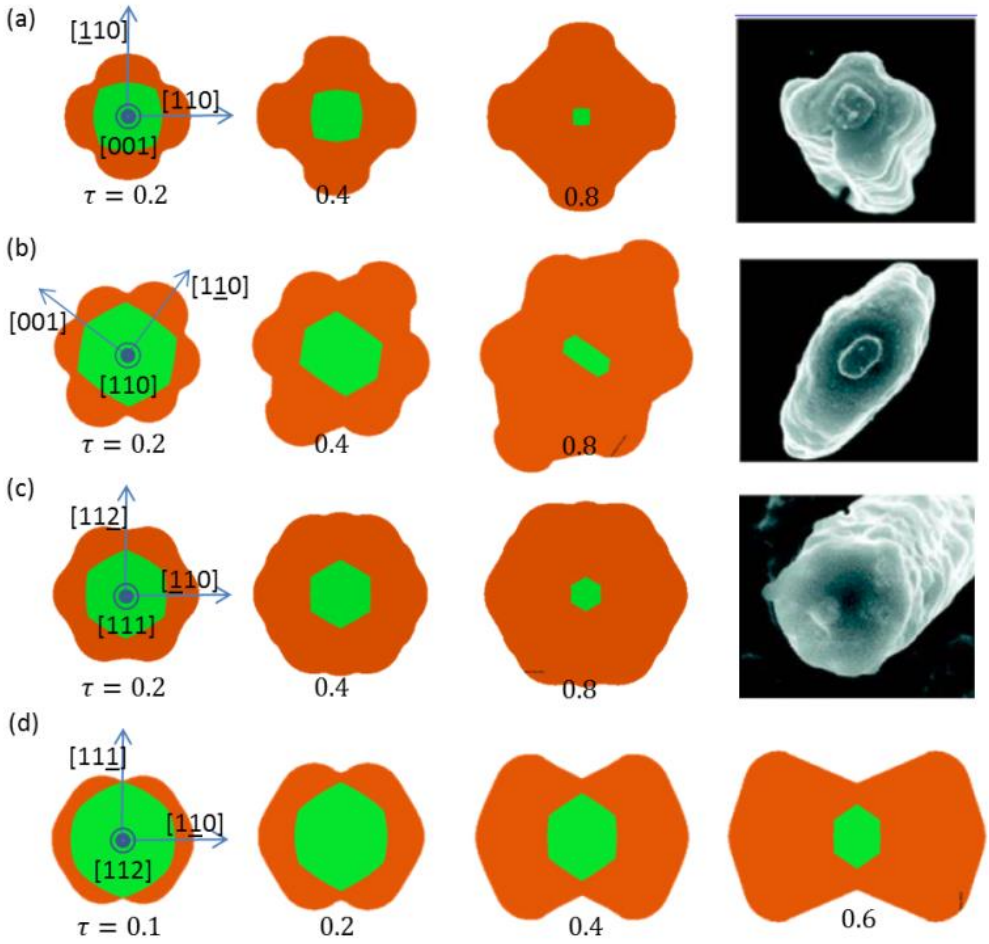

Figure 3.5. Anisotropic lithiation of nanowire with four typical orientations. Snapshots of nanowire morphologies, interface profiles and phase transitions of (a) <100> ; (b) <110>; (c) <111>; (d) <112> wires at selected normalized lithiation time. Experimental observation of the anomalous shape change in silicon nanowires (last panel in (a-c)) are compared with simulations, showing the shape change for <100>, <110>, and <111> nanowires are captured.

We first study the initial lithiation of crystal Si nanowires with circular cross-sections. Four nano wires with radius $a = 100nm$, orientated along <100>, <110>, <111>, <112> directions are studied. Here we take the results for <112> nanowire as an example, presented in details in Fig. 3.4, and put the rests in Fig. 3.5. Without losing accuracy, plane strain condition is applied for simplicity. Fig. 3.4a shows the orientation

dependent normalized ACI velocity in the cross section plane of the wire, $r = v(\theta)/v_{\max}$, where a butterfly-liked shaped is found, indicating that within the {112} plane, the ACI velocity for <112> nano wires has the first extreme (i.e., $r = 1$ or $v(\theta) = v_{\max}$) in <110> directions (the global maximum), the second extreme (with $r = 0.91$) in directions 55^o away from <110> directions (the local maximum), and a global minimum (with $r = 0$) in <111> directions. The two directions with maximums are referred as the first and the second primary directions in the following. As shown in Fig. 3.5d, from normalized lithiation time $\tau = tv_{\max}/a$ = 0.1, 0.2, 0.4, to 0.6, the ACIs (the line separating orange and green regions) along the two primary directions gradually become dominant as lithiation proceeds and eliminate the ACIs in other neighboring directions, forming faceted *c*-Si core (green region) enclosed by *a*-Li_xSi shell (orange region). As lithiation proceeds, the ACI moves inwards faster along the primary directions compared with the <111> direction, which means at any given time, *a*-Li_xSi swells larger along the primary directions. As indicated by the colormap of maximum in-plane stress over the wire cross-section at representative time $\tau = 0.2$ in Fig. 3.4c, upon first lithiation, the crystal core is constantly subjected to tensile stress due to the lithiation induced expansion along ACI (in white line), while the stress state of amorphous shell differs in two separated regions in amorphous layer. In the region right behind the moving ACI (in dark blue), the stress is compressive while in the region away from the ACI (in light blue), the stress is tensile, as a result of the lithiation induced expansion, dissipative plastic flow of amorphous phase, and the constraint enforced by geometry compatibility within the electrode. Driven by the tensile stress, material near the surface of the *a*-Li_xSi shell flows plastically from the directions with less total expansion, which is directions with minimum ACI

velocity, namely, <111> directions, to directions with more total expansion, which is the primary directions. Therefore, as illustrated by the colormap of Equivalent Plastic Strain (PEEQ) on the surface and the cross section of the wire at time $\tau = 0.2$, 0.4, and 0.6 in Fig. 3.4b, anisotropic evolution of ACI (in white line) leads to highly concentrated plastic strain in the outmost amorphous shell around planes bisecting the two closest <110> directions. Constrained by the volume conservation of plastic deformation, the flow in the hoop direction induces the necking in the radical direction. The severe plastic necking in the <111> direction, thins down the *a*-Li_xSi shell in that direction, and gives rise to sharp convex corners in *a*-Li_xSi shell. The morphology of the lithiated <112> nanowire from our simulations (left panel in Fig. 3.4d), agrees well with the dumbbell shape of lithiated <112> nanowires observed using TEM (right panel in Fig. 3.4d), suggesting the anisotropy induced plastic necking accounts for the shape change, instead of the orientation dependent lithiation strain as suggested previously [36]. Fig. 3.5a-c show the initial lithiation results for Si nanowires with other orientations. The features demonstrated by simulation result of <112> nanowire are also seen in wires with other orientations, such as formation of faceted *c*-Si cores, anisotropic morphology evolution of the *a*-Li_xSi shell, plastic necking in certain directions. Faceted *c*-Si cores with square, hexagon, and irregular polygon ($\theta = 64^o$) cross section are formed respectively for <100>, <111>, and <110> wires. The simulation successfully reproduces the morphologies of lithiated electrodes observed in experiments [21].

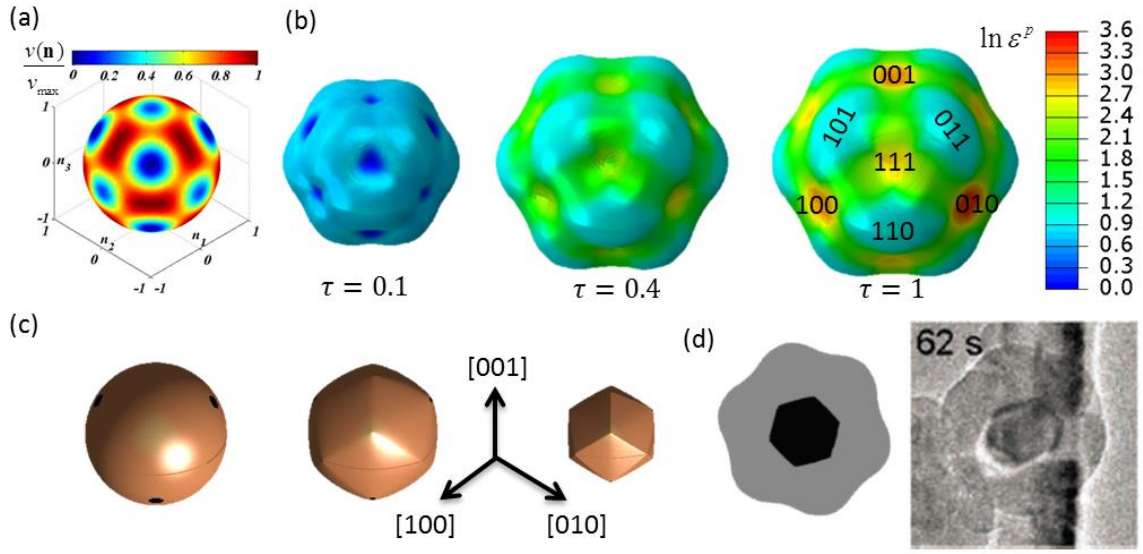

Figure 3.6. Lithiation of 3D spherical crystal nanoparticle. (a) Distribution of the interface velocity along different spatial angle, colormapped on the surface of a unit sphere with the same spherical geometry of the initial crystal particle. (b) Colormaps of equivalent plastic strain on the deformed surface of the particle at different normalized lithiation time τ = 0.1, 0.4, 0.6. (c) Morphologies of interfaces between amorphous shell and crystal core at different normalized lithation time τ = 0, 0.1, 0.4. Interface vanishes at time τ = 1. Arrangement of crystal orientation is illustrated in inset between panels τ = 0.1, 0.4, and interfaces in different octants are painted with different darknesses. (d) Comparison of simulated morphology of amorphous shell and crystal core at time τ = 0.4, with TEM image of lithiated nanoparticle from literature. Both profiles of the amorphous and crystal phases are captured precisely.

As another commonly used electrode geometry, spherical nano particles (radius $a = 100nm$) is simulated to explore the anisotropic lithiation behavior of crystal Si in a 3D case. The distribution of the interface velocity along different spatial angle, is color mapped on the surface of a unit sphere whose appearance is adjusted to be the same spherical geometry of the initial crystal particle, as shown in Fig. 3.6a, showing local minimum $v/v_{\max} = 1/6$ in <100> directions, global minimum $v/v_{\max} = 0$ in <111> directions, and global maximums of $v/v_{\max} = 1$ in <110> directions. As shown by colormaps of the PEEQ on the deformed surface of the particle at selected times $\tau = 0.1$,

0.4, and 1 (Fig. 3.6b), the particle continuously swells as lithiation proceeds, with "bumps" formed in all <110> directions and "pits" formed in <100> and <111> directions due to the differences in ACI velocity along different directions. The relative magnitude of the PEEQ on the surface in these different directions has a transition at time approximately $\tau = 0.2$. At early stage, PEEQ has large value in <110> directions as shown in panel $\tau = 0.1$ in Fig. 3.6b, while at late stage PEEQ has smaller value in <110> directions as shown in panels $\tau = 0.4$, and 1 in Fig. 3.6b. By the snapshots of the morphology of the crystal core at the same lithiation time (Fig. 3.6c), similar to the 2D case, the *c*-Si core enclosed by ACI continuously and anisotropically shrinks as lithiation proceeds. Eventually, a rhombic dodecahedron shaped *c*-Si core is formed. When the snapshots of the our surface morphology and the core morphology at $\tau = 0.4$ are put together centrically and rotated 15^o clockwise (left panel in Fig. 3.6d), both the profiles of the *a*-Li_xSi layer and the *c*-Si core look astonishingly similar to the TEM image of the lithiated spherical nano particle [17] (right panel in Fig. 3.6d). To our best knowledge, it is the first time for a simulation work to successfully capture the morphology of both crystal core and amorphous shell of 3D nano particles.

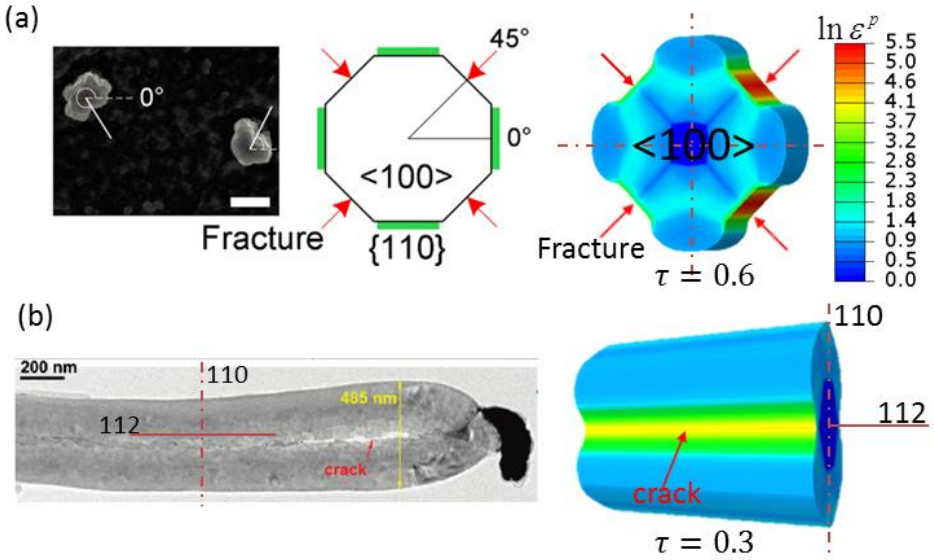

Figure 3.7. Comparison of the directional fracture behavior of circular nanowires from experiments with simulation results. (a) <100> (b) <112> circular nanowires fracture along planes bisecting two nearest in plane <110> directions in experiments (left panels) and equivalent plastic strain concentrates on the surface of nanowires along the same directions by simulation (right panels), at time (a) τ = 0.6 (b) τ = 0.3, suggesting the concentrated plastic strain on the surface accounts for the fracture of the circular nanowires.

As one of the main reasons that hinder the broad application of silicon electrode in LIB, fracture or mechanical degradation is widely studied. It is found that even for nanowires the fracture is severe, and highly anisotropic [26, 36]. In Fig. 3, we list the TEM images from literature showing the directional fracture behavior of two typical electrodes, namely, <100>, and <112> nanowires. To compare, color map of PEEQ on the surface of the wire at representative time is plotted. It is found that the nanowires fracture in the exactly same directions where the most concentrated plastic strain exists, which suggests that mitigation of the catastrophic plastic flow could possibly improve the fracture performance of the silicon nanowires as electrodes. Both our simulation and other experimental studies have shown that crystal Si nanowires with circular original cross section deform anisotropically after initial lithiation and the strong anisotropic

deformation leads to catastrophic fracture. Here we propose to rationally design the original geometry of the nanowires, which accommodates the anisotropic initial lithiation of *c*-Si better so that relative isotropic morphology is produced and the concentrated plastic flow is mitigated. A simple first step is to use less material in the primary lithiation directions and more materials in the slow lithiation directions.

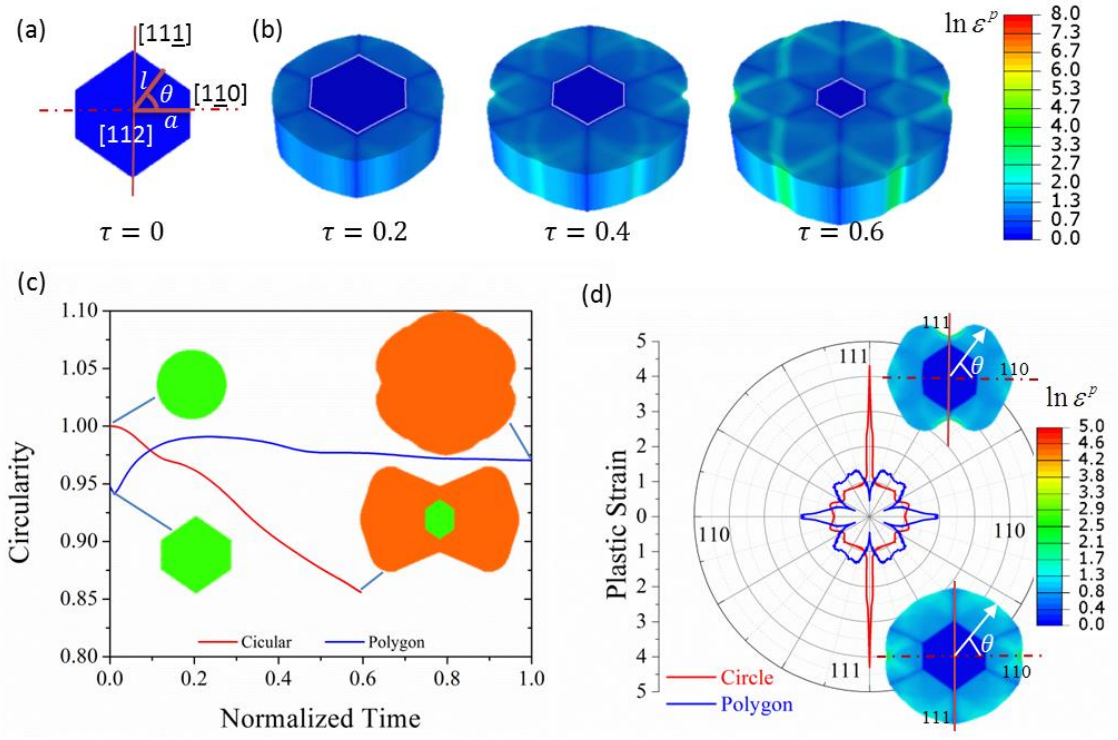

Figure 3.8. Lithiation of <112> crystal nanowire with designed polygon cross-section. (a) Design of <112> crystal nanowires with polygon cross-section, in which angles and lengths marked in white satisfy θ=55° and $l/a = 0.91$, determined by the interface velocity profile as in Fig. 1a. (b) Snapshots of nanowire morphologies, and interface profiles (white solid line), and colormaps of equivalent plastic strain at different normalized lithiation time τ = 0.2, 0.4, 0.6. (c) Comparison of the circularity of <112> nanowires with circular and polygon cross-sections as function of time, suggesting polygon nanowire has much isotropic geometry after lithiation. (d) The equivalent plastic strain on the perimeter of the circle and polygon cross section of the <112> nanowires as a function of the angle away from in plane <110> directions (marked in white), at time τ = 0.3, with two insets showing the colormaps of equivalent plastic strain on cross section at the same time, suggesting the polygon design helps to repress the high concentration of plastic strain in certain directions.

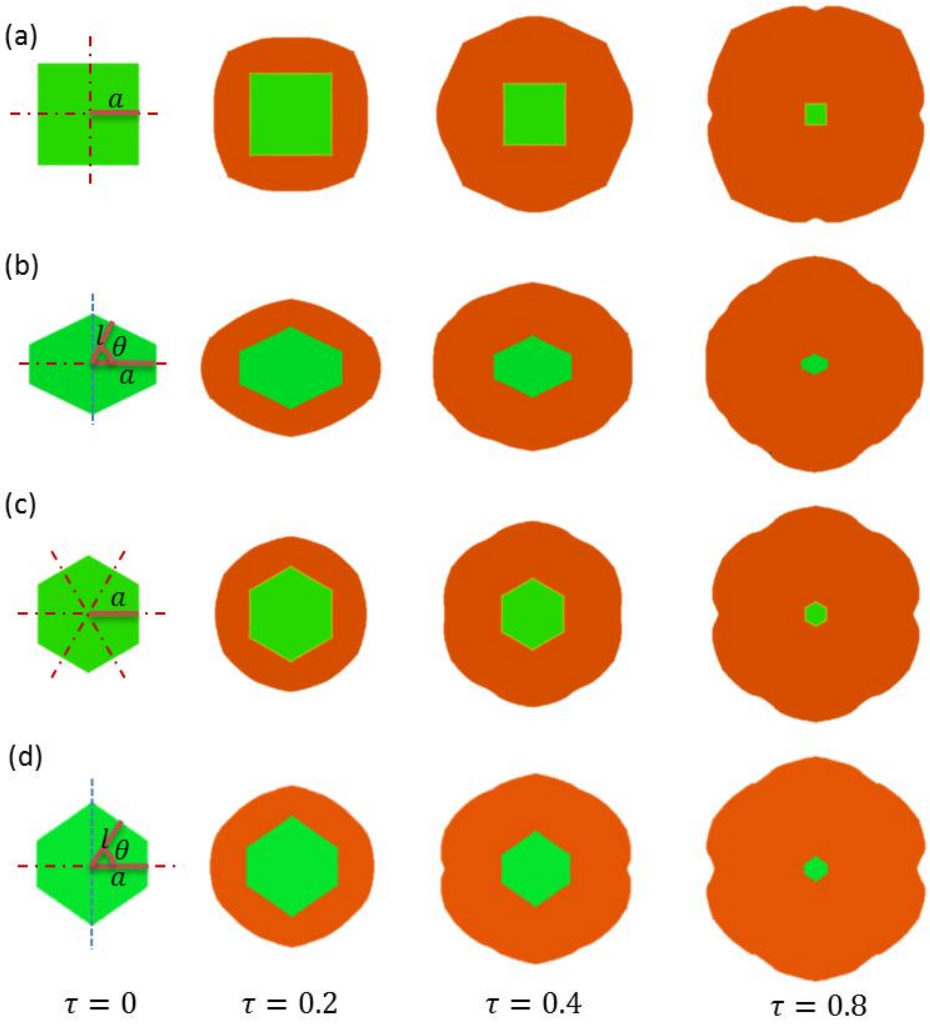

Figure 3.9. Design of (a) <100> nanowire with square cross-section; (b) <110> nanowire with polygon cross-section (θ=64° and $l/a = 0.72$) (c) <111> nanowire with hexagonal cross-section. Snapshots of nanowire morphologies, interface profiles and phase transitions at normalized lithiation time τ = 0.2, 0.4, 0.8 for nanowires with different orientations, with the τ = 0 panel showing the original geometry.

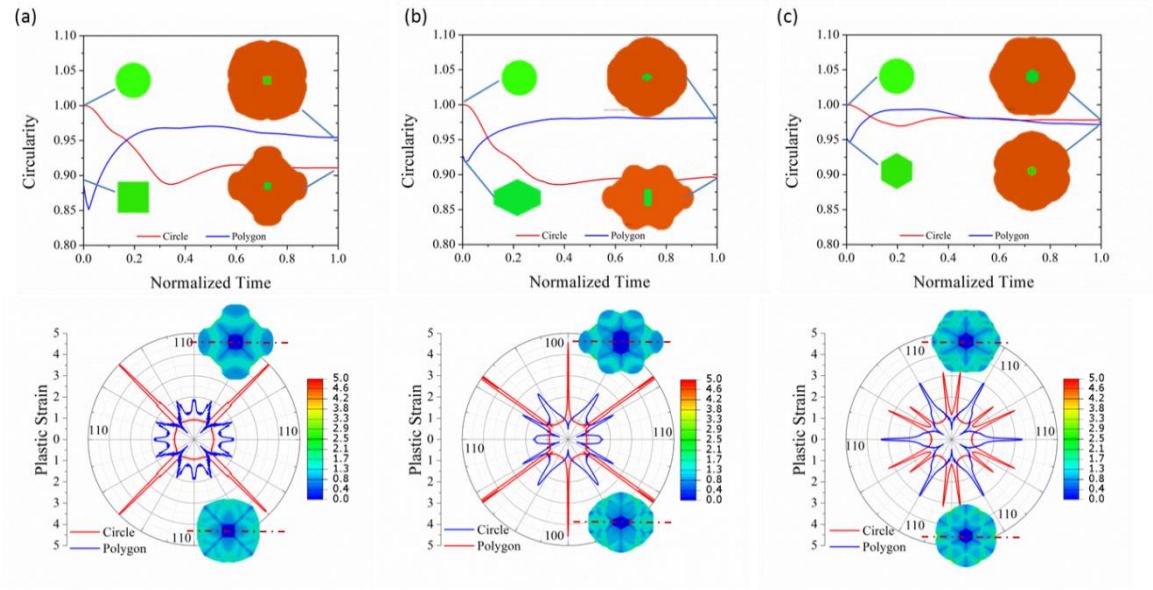

Figure 3.10. Comparison of the circularity as function of time (upper panel), and plastic strain on the perimeter of cross-section as function of in-plane angle at time τ = 0.6 (lower panel), for (a) <100>; (b) <110>; (c) <112> nanowires with circular and polygon cross-sections. It is shown that designed polygon nanowire has much isotropic geometry after lithiation, and helps to repress the high concentration of plastic strain in certain directions. The benefits from polygon geometry for <111> wire are marginal because interface velocity in the cross-section is much less anisotropic.

Therefore, for 2D nanowire electrode, the proposed geometry is the polygon cross section (Fig. 3.8 and Fig. 3.9). In those polygons, all the sides are perpendicular to the primary directions, with the distance of each side to the center of the cross-section being proportional to the ACI velocity in that direction. Taking the <112> orientated wire/pillar for instance, whose newly designed geometry is shown in Fig. 3.8a. There are two types of sides for the polygon cross-section. Some are the {110} planes with distance to the center $a = 100nm$; while the others are the planes rotated 55^{o} angle from {110} planes, with distance $l = 0.91a$ from the center. Parameters are predetermined by the profile of ACI velocity projected onto the {112} plane (Fig. 3.4a), and are selected in the way that all the sides of the polygon ACI reach the center of the cross-section simultaneously and

pertain the self-similar shape of the crystal core without forming any singular shape at the late stage of initial lithiation. The evolution of ACI and the electrode morphology is demonstrated in Fig. 3.9d. As shown by the colormap of PEEQ on the deformed surface of polygon nanowire at time $\tau = 0.1$, 0.4, and 0.6 in Fig. 3.8b, the lithation of the nanowires with designed polygon cross-section gives a much more isotropic morphology compared to the original circular wires (Fig. 3.4b), and significantly decreases the magnitude of PEEQ. To quantify the isotropy of the morphology of electrode cross section, here the circularity C_{2D} of a 2D object with area A_{2D} and perimeter L_{2D} defined as $C_{2D} = \frac{2\pi\left(A_{2D}/\pi\right)^{1/2}}{L_{2D}}$, the ratio of perimeter of a circle with the same area to the perimeter of this 2D object. It can be shown that the maximum circularity for any 2D object is one, for perfect circle. The more isotropic a 2D object is, the greater its circularity is. In Fig. 3.8c, the circularity of the originally circular and polygon <112> nanowires are potted as function of time, clearly showing that designed polygon geometry improves the isotropy of the electrode. Insets are the morphologies of the electrodes at the beginning and the end of the lithiation process for two different geometries respectively. In Fig. 3.8d, PEEQ on the perimeter of the two different <112> nanowire electrode is plotted as function of the in-plane angle away from <110> direction at time $\tau = 0.3$, clearly showing the PEEQ highly concentrated in some particular directions in circular nanowire is effectively mitigated when the proposed polygon geometry is applied. Insets are the comparison of the PEEQ over the cross-section of circular and polygon nanowires at the same time. The original polygon geometry, and the evolution of the ACI and electrode morphology for <100>, <110>, and <112> wires are shown in Fig. 3.9a-c. The circularity of the electrode morphology and the

angular distribution of the PEEQ on the perimeter of other polygon electrodes are compared with their circular counterparts in Fig. 3.10, showing significantly improved isotropy of the electrode morphology and the magnitude of the PEEQ for all the electrode orientations, except for the <111> wire in which the interface velocity is much less anisotropic.

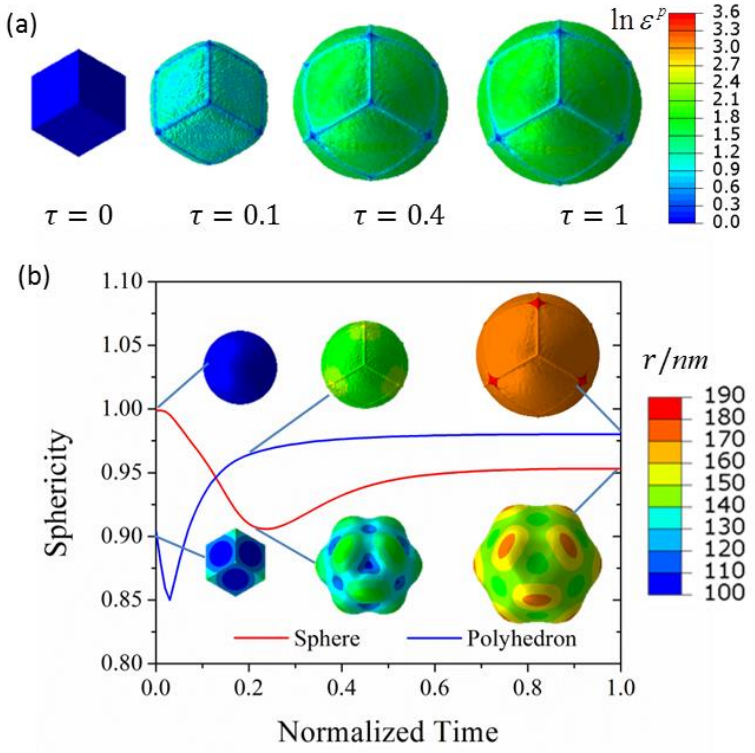

Figure 3.11. Lithiation of 3D crystal nanoparticle with designed rhombic dodecahedron geometry. (a) Colormaps of equivalent plastic strain on the deformed surface of the particle at different normalized lithiation time τ = 0, 0.1, 0.4, 0.6, with the τ = 0 panel showing the original electrode geometry. By Comparison with the spherical particle (Fig. 4b), plastic strain is significantly reduced. (b) Comparison of the sphericity nanoparticles with geometries of sphere and polyhedron as function of time, suggesting polyhedron nanoparticle has much isotropic geometry after lithiation. Insets are the colormaps of distance of deformed surface to the center of the particle at selected times.

Following the same philosophy, the rhombic dodecahedron geometry is proposed for 3D nano particle electrode, with all the twelve faces orientated in <110> directions

and positioned at distance $a = 100nm$ from the center (Panel $\tau = 0$ in Fig. 3.11a). This design is inspired by the convergent shape of the crystal core for the spherical particle. As shown by the colormaps of PEEQ on the deformed surface of the electrode at different lithiation time, $\tau = 0.1$, 0.4, and 1, in Fig. 3.11a, the electrode with rhombic dodecahedron shape bumps out in <110> directions as lithiation proceeds, gradually grow into the shape approximately to a sphere, with some small corners and edges inherited from the original geometry which could be totally avoided in practice by rounding them at the first place. Compared with the colormap of PEEQ on the surface of spherical particles at the same time under the same scale (Fig. 3.11b), the PEEQ on the surface of the polyhedron particle is greatly decreased and uniformly distributed. Without explicitly showing here, one should note the crystal core enclosed by the ACI is shrinking continuously in this process in the self-similar rhombic dodecahedron shape. Similarly as in the 2D case, to quantatively characterize the isotropy of the morphology of particle electrode, here the sphericity S_{3D} of a 3D object with volume V_{3D} and surface area A_{3D} is defined as $S_{3D} = 4\pi\left(\frac{3V_{3D}}{4\pi}\right)^{1/3} / A_{3D}$, the ratio of surface area of a sphere with the same amount of volume to the surface area of this 3D object. It can be shown that the maximum sphericity for any 3D object is 1, for perfect sphere. The more isotropic a 3D object is, the greater its sphericity is. In Fig. 3.11b, the sphericity of the originally sphere and polyhedron nanoparticles are potted as function of time, definitely showing designed polyhedron geometry improves the isotropy of the electrode. Insets are the morphologies of the electrodes at selected stages of the lithiation process for two different geometries respectively.

The new polygon/polyhedron design provides several benefits compared to the old circular/spherical geometry. First, the magnitude of plastic strain accumulated on the surface of the electrode is effectively mitigated by the designed polygon/polyhedron for both nanowire and nanoparticle electrodes compared to their circular/spherical counterparts, and no apparent strain concentration is observed on all the polygon/polyhedron. This helps to maintain the mechanical integrity of the electrode during the first lithiation. Our recent work on silicon micropillars [225] did confirm that the morphology of the <100> square pillars after first lithiation is much more isotropic, and volume expansion for crack initiation during the first lithiation is improved by 88%, compared to the circular pillars. Second, the much more isotropic geometry of the polygon/polyhedron electrode after initial lithiation, is expected to homogenize the stress distribution within the electrode in the subsequent isotropic delithiation/lithiation cycles, therefore improve the long term stability of the electrode. Third, the much more isotropic geometry of the polygon/polyhedron electrode after the first lithiation gives less surface area, reducing the formation of solid-electrolyte-interface which is considered to hinder the kinetics of electrode.

There are several possible routes to realize above proposed geometry. Silicon pillars with bigger feature size can be directly fabricated by photolithography and try etching as in our previous work [225]. For smaller electrode, direct growth controlled in a desired anisotropic fashion as suggested in literature [226], or controlled anisotropic etching of silicon wafers/particles [227-229] can be are more desirable.

3.5. Conclusion

By incorporating the information from both experiments and calculations at atomic scale, and taking into account the crystallography of silicon, a new continuum

model for reaction controlled interface migration is developed in this chapter, with both the theoretical formulation and numerical implementation applicable to structures with any two/three dimensional geometry. Compared to previous works [39], our model has the following merits . I. It represents a truly 3D model formulated self-consistently and generally. II. All the model parameters have clear physical significance and measurable directly in experiments. III. The model can be extended easily under the same numerical implementation as long as more information on the ACI velocity is available, from experiments or atomic calculations. When applied to circular/spherical electrode, our model discovers some very interesting phenomena such as formation of faceted crystal core and plastic instability, and successfully captures the morphology evolution and the kinetics in the electrode, well agreed with the reported experiments. A new polygon/polyhedron design philosophy is proposed based on the findings from simulation, and is demonstrated to be beneficial to the electrode in short/long term mechanical integrity and rate performance.

CHAPTER 4

ENHANCED LITHIATION AND FRACTURE BEHAVIOR OF SILICON PILLARS VIA ATOMIC LAYER COATINGS AND GEOMETRY DESIGN

Crystalline silicon nanostructures are commonly known to exhibit anisotropic expansion behavior during the lithiation that leads to grooving and fracture. Here we report surprisingly relatively uniform volume expansion behavior of large aspect-ratio (~25), well-patterned, n-type (100) silicon micropillars (~2 μm) during the initial lithiation. The comparison results with and without atomic layer metal oxides (Al_2O_3 and TiO_2) coatings reveal drastically enhanced solid electrolyte interphase (SEI) formation, higher volume expansion, and increased anisotropy. Square-pillars are found to exhibit nearly twice volume expansion without fracture compared to circular-pillars, partially verified the geometry design principle we proposed in Chapter 3. Models are invoked to qualitatively address these beneficial or detrimental properties of silicon for lithium ion battery. Our experiments and computer simulations point at the critical relevance of SEI and pristine geometry in regulating volume expansion and failure, suggesting new ways of designing electrodes for high-performance lithium ion battery applications.

4.1. Introduction

The large lithium storage capacity (~4200 mAh/g theoretically) and industry scalable manufacturing capability of various silicon materials (including micro- and nano-scale structures) have inspired intense research in these materials as anodes for lithium-ion batteries (LIB) [25, 40]. The enormous potential of silicon as energy storage materials has however been counteracted by several known challenges, including a rather large volume expansion (VE ~300%) during lithiation that inevitably degrades the structural integrity of silicon electrodes during the cycling, highly anisotropic lithiation/delithiation behavior witnessed in single crystalline silicon, and poor solid electrolyte interphase (SEI) layer formation. To overcome the first two shortcomings, a wide variety of nanostructures or amorphous silicon (e.g., nanowires, nanotubes, nanoparticles, and nanoporous structures) have been intensively investigated where much valuable information has been garnered [26, 38, 211, 230, 231]. Unfortunately nanostructured silicon is expensive to scale-up and also suffers from intrinsically low tap density (leading to low volumetric capacity). Furthermore, high surface area nanostructures inevitably induce worse SEI layers that are known to degrade the performance of secondary batteries [163]. In comparison, the electrochemical and electromechanical behavior of mesoscale (e.g., micrometer-sized) silicon is less well understood. To date a limited amount of experiments have been conducted [232, 233]. Because of the clear size, stress and subsequent phase boundary curvature differences, the lithiation kinetics of microsized silicon is expected to be different from that of nanostructures. Such information could bear critical relevance to the commercial applications due to the high energy density needs that call for thick electrodes (e.g., commercial electrodes are typically over 100 micrometers thick).

Another critical challenge yet little understood to the long cycle life of silicon-based LIBs is to overcome the poor SEI layers that are intrinsically associated with large volume change electrodes. Such SEI layers are unstable both mechanically and thermally as the SEI layer is an organic/inorganic composite (e.g., containing Li_2CO_3, LiF, $(CH_2OCO_2Li)_2$, polycarbonates) [163, 166] that could decompose at a relatively low temperature. The continuous re-exposure of fresh silicon to electrolyte due to the instability of SEI leads to low Coulombic efficiency and may promote subsequent exothermal reactions that lead to "thermal runaway" and cause fire and explosion of LIBs due to the chain reactions of oxidative cathode materials (if a full cell configuration is used). As such, the thermal and mechanical stability of SEI layers on anodes is of importance to the safety of LIBs. To this end, few studies have been performed to address these SEI issues, with existing effort focused on carbon or silicon oxide coatings as the potential front-runner solutions. The former is electrically conductive such that it may not be able to impede the growth of SEI at low potentials [233], while the latter has low fracture toughness, Tab. 4.1 [214, 234-239], and can be reactive to fluoride species, and thus requires strict structural designs [25]. Another important class of coating materials is metal oxides, which can not only offer high thermal stability, but also possess other beneficial properties such as high mechanical strength and fracture toughness, low electrical conductivity, and high lithium diffusivity (Tab. 4.1 [240]). These unique properties render them as excellent surface protection materials for anodes (as well as cathodes). Enhanced cycling performance and high Coulombic efficiency have indeed been reported in Al_2O_3-coated silicon nanostructures [241, 242]. Nonetheless, there exists limited understanding of the impact of metal oxide coatings on the lithiation and fracture/failure behavior of silicon materials.

Table 4.1. Selected properties of silicon, SiO_2 and metal oxides

Materials	Fracture toughness (MPa $m^{1/2}$)	Electrical conductivity (S/cm)	Li ion conductivity (S/cm)
Al_2O_3	2.7 - 4.2 [238]	10^{-14} (crystalline) [237]	10^{-6} (amorphous) [234]
TiO_2	2.38 [238]	10^{-6} [235]	10^{-5} - 10^{-7} (Rutile) [236]
SiO_2	0.7 [240]	10^{-14} [237]	-
Si	<110>: 0.73 <100>: 0.89 [239]	2 (our data)	~3 × 10^{-7} [214]

By using atomic layer deposition (ALD), here we report on the substantially enhanced lithiation and fracture behavior of silicon micropillar arrays that are ALD-ed with an ultrathin layer (<1 nm) of Al_2O_3 and TiO_2, respectively. Silicon micropillars for this study were directly fabricated from (100) n-type silicon wafers with a diameter of 2 μm and a height of 50 μm, yielding a height/diameter aspect ratio of 25:1. To our knowledge, this is the highest aspect ratio silicon micropillars reported so far for investigation of lithiation behavior, which mechanistically ensures plane strain condition near the pillar top without having to take into account the substrate confinement effect. Similar pillars have been popularly used as thermal neutron detector materials with excellent performance [243]. The penetration ability of ALD technique to very high aspect ratio structures further makes these studies possible. We investigate two types of conformal coatings; i.e., 0.43-nm-thick Al_2O_3 and 0.75-nm-thick TiO_2, respectively (both thicknesses are nominal). To explore the initial pillar geometry effect on the lithiation/fracture behavior, square micropillars were also fabricated. Systematic and comparison experiments were performed on the bare silicon circular micropillars (bare-Circular-Si), Al_2O_3-coated (Al_2O_3-ALD-Circular-Si) and TiO_2-coated (TiO_2-ALD-Circular-

Si) silicon circular micropillars, and TiO_2-coated square micropillars (TiO_2-ALD-Square-Si). For the square-shaped pillars, the orientation of four sides is oriented along {110} crystallographic planes, which is considered as the fastest Li diffusion direction in silicon. Earlier studies have generally revealed that circular shape nanowires exhibit strong anisotropic expansion, leading to grooving and fracture. It is thus interesting and of technological importance whether similar behavior occurs in mesoscale pillars and whether one can take advantage of geometrical design to mitigate or even completely annihilate such anisotropic failure behavior.

4.2. Experimental Details

Preparation of Si micropillars: Bulk n-type (100) silicon wafers with the conductivity of 2 S/cm (determined by a four point probe method) were selected for micropillar fabrication. The pillar diameter and spacing were defined lithographically, followed by inductively coupled plasma etching. The etching process used a Bosch Process (also known as pulsed or time-multiplexed etching), alternating repeatedly between two modes to achieve vertical structures. This was accomplished by alternating between isotropically etching the silicon with a short duration of 25 sccm SF_6 plasma, and a short duration of polymerization using 80 sccm C_4F_8. The passivation layer protected the entire substrate from further chemical attack and protected further etching. Circular- and square-shaped pillars were fabricated according to the applied mask. The diameter, spacing and height of the pillars were 2 μm, 2 μm and 50 μm, respectively. The high quality and well-patterned nature of all as-fabricated pillars can be seen in Fig. 4.1a-c scanning electron microscopic (SEM) images.

TiO_2 and Al_2O_3 ALD coatings: To investigate the coating effect, silicon micropillars were coated with sub-nanometer-thick Al_2O_3 or TiO_2 films using the well-

established trimethyl-aluminum ($AlMe_3/H_2O$) [244] and titanium tetrachloride ($TiCl_4/H_2O$) [245] atomic layer deposition (ALD) processes in a warm wall reactor with the wall temperature of 100 °C and the sample stage temperature of 125 °C for Al_2O_3 and 110 °C for TiO_2. Long pump, pulse and purge times (20s/50s/50s) were used to ensure uniform coatings throughout the material. The nominal film thicknesses using 15 cycles for TiO_2 and 3 cycles for Al_2O_3 are 0.75 nm and 0.43 nm based upon the ALD rates reported in ref. [246] and [247], respectively.

Transmission electron microscopy (TEM) sample preparation: the TEM samples of TiO_2 ALD coated silicon micropillars were prepared by using a focused-ion-beam (FIB) (FEI, Nova 600) liftout method, where the target pillar arrays were first coated with a thin protection layer of e-beam Pt, followed by the further deposition of ion-beam Pt which helps to "weld" several pillars together, Fig. 4.1d. The cross-sectional samples were examined in a FEG Philips CM300 TEM with traditional bright-field (BF) and high-resolution (HR) imaging conditions. The BF TEM in Fig. 4.1e suggests the side surface of silicon pillars generally exhibit zig-zag etching features, which is in contrast to the atomic smoothness of the top surface of the pillars. The atomic coating layer of TiO_2 is generally visible in HRTEM image shown in Fig. 4.1f. However, the thickness of the ALD observed under TEM appears thicker than the nominal thickness of ALD layer calculated from the deposition rate of our processes, likely due to the compound effect of TEM sample thickness, tilting angles of the sample towards electron beam, and the fact that the side surface could also contain silicon native oxide layers.

Cell assembly and characterizations: The silicon micropillars standing on a Si wafer were directly assembled into a Swagelok-type half-cell (~71 mm^2 surface area) with lithium metal as the counter electrode. A commercial electrolyte (MTI Cor.) of 1 M $LiPF_6$

in a mixed solution of ethylene carbonate, diethyl carbonate and dimethyl carbonate (EC/DEC/DMC, v/v = 1:1:1) was adopted with a polypropylene separator (Celgard 3501, PP double layer, ~25 μm each). Cell assembly was completed in an argon-filled glove box (VAC Omni) with oxygen and water content less than 1 ppm. A Maccor 4304 battery cycler was used to perform the initial lithiation process from the open circuit potential (~ 3 V) to a target voltage of 50 mV at a constant scan rate of 0.1 mV/s, and then was held for 20 hrs. After electrochemical lithiation, cells were dissembled inside the glove box and the lithiated electrodes were washed by dimethyl carbonate (DMC) for imaging. The morphology change was characterized by a field-emission scanning electron microscope (SEM, JEOL 7401-F) operated at 2 kV. The same FIB machine was used to cross section some selected pillars for SEI examinations.

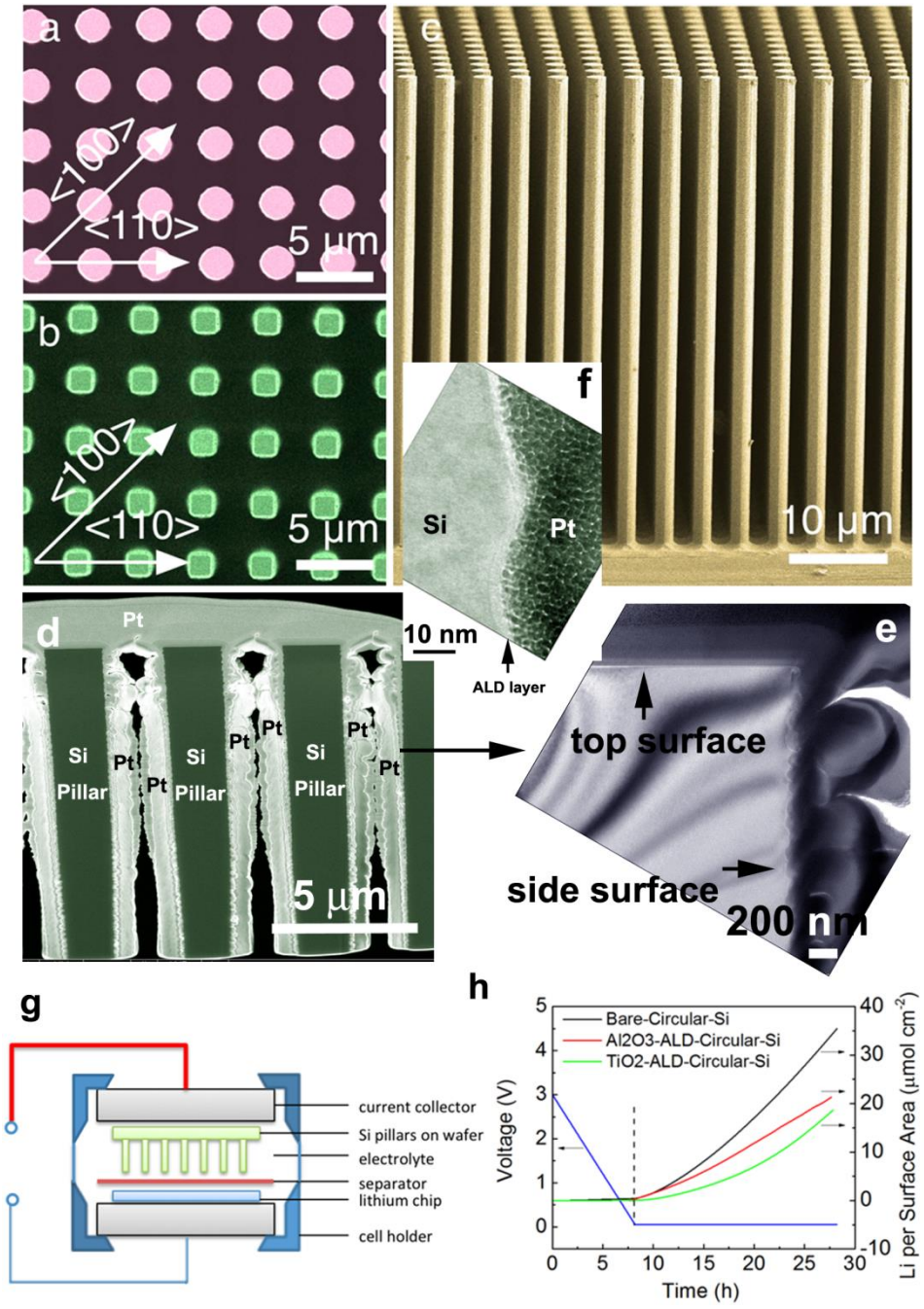

Figure 4.1. Initial morphology of silicon micropillars and the experimental setup. (a) and (b), top-view scanning electron micrograph (SEM) of circular and square pillars, respectively. The crystallographic orientations are labeled in the figure. (c) A side-view SEM image of circular pillars. (d) A cross-sectional SEM image of a liftout piece, showing several cut and welded silicon pillars. (e) A BF TEM image of silicon pillar with side- and top-surface marked. (f) A zoomed-in high-resolution TEM image of the side surface of silicon pillars. (g) An illustration of our experimental setup using a half-cell assembly.

(h) Voltage and lithiation profile of three types of circular pillars. Note that the apparent lithiation rate of ALD-coated samples seems lower compared to the bare-Circular-Si. This phenomenon could be caused by the formation of SEI layers without ALD coatings (see text for detailed discussion).

4.3. Experimental Results and Discussion

4.3.1 Unexpected lithiation behavior before and after ALD

With a half-cell configuration shown in Fig. 4.1g, we investigated the initial lithiation behavior of above silicon micropillars, including Li uptake, SEI formation, VE, and fracture behavior. The lithiation time for all pillars is fixed at 20 hrs, and the total Li uptake is estimated from the current profile for three types of circular pillars, as illustrated in Fig. 4.1h. By using the data in the figure, and assuming that the Li intake is mainly due to the silicon micropillars, we found that the apparent lithiation intake of bare Si can reach up to 8.8 Li per Si after 20 hrs of lithiation, which is well above the theoretical Li storage capacity (3.75 Li per Si by assuming $Li_{15}Si_4$ room-temperature product). Such a crude estimation however did not take into account of the potential current leakage and the lithium intake of the substrate. Nonetheless, this could also suggest the formation of massive SEI layers under the current low-voltage lithiation conditions (i.e., 50 mV). This SEI behavior is confirmed by SEM images shown in Fig. 4.2a, where the SEI layer appears rather rough for the bare silicon. In contrast, such SEI formation has been substantially mitigated in both Al_2O_3-coated and TiO_2-coated samples, Fig. 4.2b and Fig. 4.2c, respectively. The contrast behavior of SEI formation for bare silicon and ALD-coated samples can be better viewed from the side surface for all three samples, Fig. 4.3. Quantitative measurements of SEI for bare silicon reveal a thickness of up to ~0.5-0.8 μm (Fig. 4.3a), whereas the thickness of SEI layer in ALD-coated samples is no more than 150 nm, as indicated by the focused-ion-beam cutting

image shown in Fig. 4.3e. Unexpectedly, we observe relatively uniform VE behavior for the bare-Circular-Si before the fracture (Fig. 4.2a and Fig. 4.3a), in contrast to widely reported anisotropic expansion of silicon crystalline nanowires or nanopillars [26]. In our cases, strong anisotropic expansion is only observed for ALD-coated samples (Fig. 4.2b and 4.2c). The near uniform expansion behavior seen in the bare-Circular-Si suggests that the formation of SEI layers plays a crucial role in regulating lithium transport under the current experimental conditions, and that the lithiation behavior of these bare-Circular-Si micropillars may no longer be controlled by the phase-boundary mobility [40]. To quantify the anisotropic VE behavior in three types of samples, we define an anisotropic index factor χ as the ratio of pillar dimension along the <110> ($d_{<110>}$, preferentially swelling direction) and <100> direction ($d_{<100>}$, less expansion direction) right before the crack formation. Tab. 4.2 indicates that the bare-Circular-Si has a χ value of 1.02±0.03 (i.e., near uniform expansion), approximately 13% smaller compared to the values of Al_2O_3-ALD-Circular-Si (χ =1.15±0.03) and TiO_2-ALD-Circular-Si (χ =1.13±0.04) pillars. Moreover, we find that the overall achievable VE before fracture of both ALD-samples is about 10% higher than that of the bare-Circular-Si, suggesting the positive role of ALD coatings. The χ values measured in both ALD-samples suggest that the lithiation rate along [110] and [100] orientations is on average <~15% -- a value that seems substantially smaller than that reported in the literature [40, 232]. The present experimental results also indicate that, due to the excellent ionic conductivity but electronically insulating nature of metal oxides (see Tab. 4.1), these ultrathin ALD coatings not only help to form and stabilize thin SEI layers (leakage of electrons is one of the main causes that promote the decomposition of electrolytes), but

also enhance the VE of silicon micropillars (likely due to the suppression of surface defects after ALD, to be discussed later).

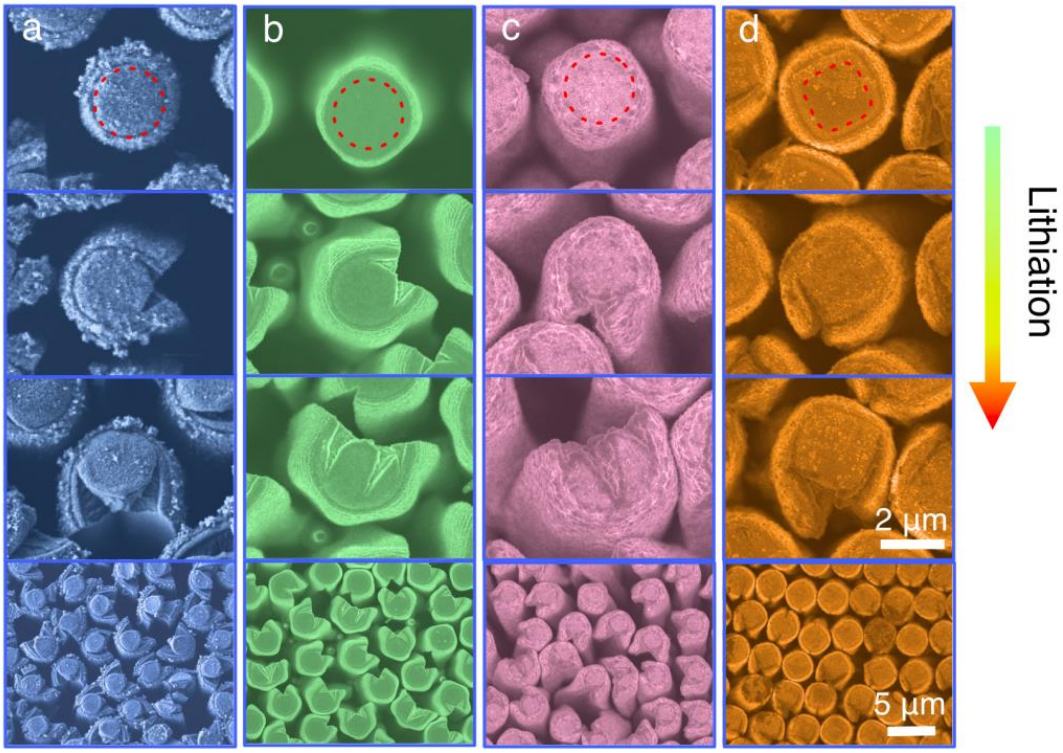

Figure 4.2. Cross-sectional morphology evoluations during the progressive lithation for four types of silicon pillars: (a) bare-Circular-Si, (b) Al_2O_3-ALD-Circular-Si, (c) TiO_2-ALD-Circular-Si, and (d) TiO_2-ALD-Square-Si. The red dashed lines in the first row denote the orignial size and shape of the respective pillars. The bottom row is the low magnification images of various pillars. The scale bar is the first three rows is 2 μm, and the last row is 5 μm. Note the very different shape change and fracture patterns/directions in these pillars.

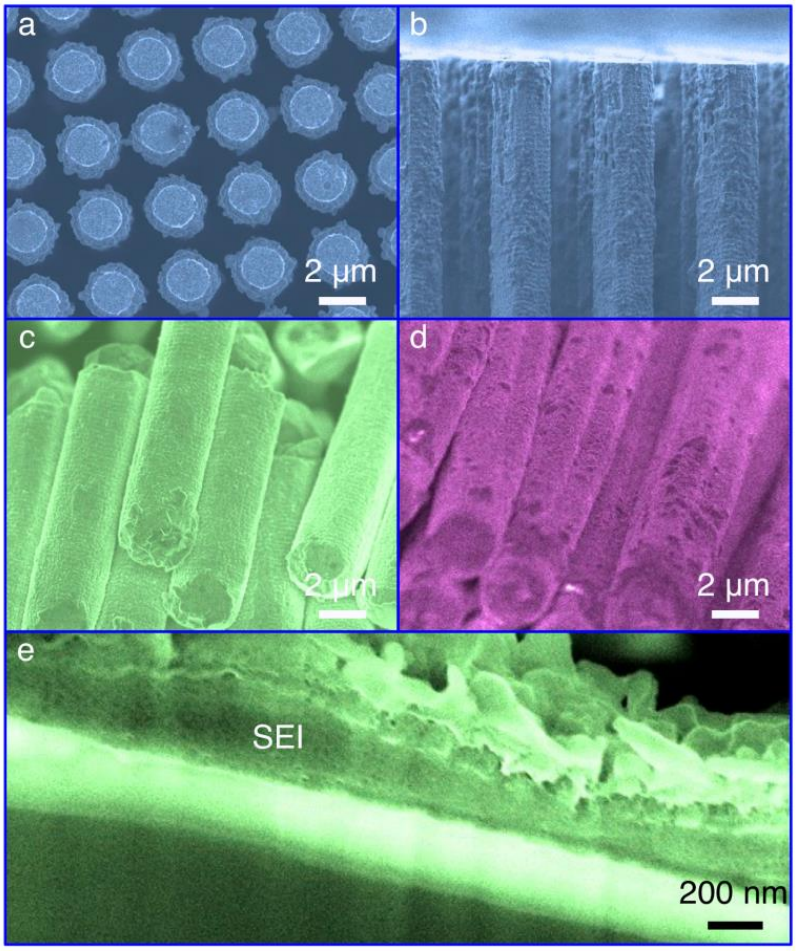

Figure 4.3. Formation of SEI in three types of circular pillars. (a) top- and (b) side-view of bare silicon after partial lithiation. Note the thick SEI layers observable from (a). (c) and (d) Side-view of Al_2O_3-ALD-Circular-Si and TiO_2-ALD-Circular-Si after partial lithiation. Note the smooth and clean nature of these surfaces. (e) Focused-ion-beam (FIB) cross-sectional cutting of Al_2O_3-ALD-Circular-Si sample after partial lithiation. Note that the sample has been exposed to the air for a few hours before the FIB sectioning, which may have increased the surface roughness of the SEI layer.

4.3.2 Square pillars vs. circular pillars (geometry effect)

Compared to circular pillars, the VE behavior of square pillars is quite intriguing. For meaningful comparison, we also ALD-ed square pillars with the same thickness of TiO_2 and carried out lithiation experiments under the same conditions as those of circular pillars. Interestingly, the square pillars become near circular shape after

lithiation due to the preferential expansion of {110} side surface, Fig. 4.2d. As a result, the χ value increases from 0.71 (square) to 0.95±0.02 (close to circular shape) after lithiation. Significantly, the overall VE of square pillars increases up to 165% before cracks initiate; this represents an impressive 88% increment over the circular pillars, Tab. 4.2. These results strongly argue that square shape (instead of circular one) is a better geometry for large Li storage in silicon – an interesting observation that has not been reported in the literature.

Table 4.2. Anisotropic shape index before (χ_{before}) and after (χ_{after}) lithiation for various silicon pillars, which is defined as the ratio of dimension along <110> and <100> directions: $\chi = d_{<110>}/d_{<100>}$. χ_{after} is measured at ΔV_c (the maximum volume expansion before the crack formation).

Pillar type	Geometry	χ_{before}	χ_{after}	Difference of average lithiation velocity between [110] and [100]
Bare-Circular-Si	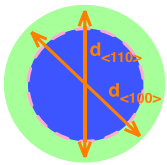	1	1.02 ± 0.03 @ ΔV_c = 82%	~0
Al_2O_3-ALD-Circular-Si	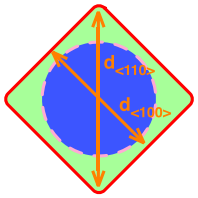	1	1.15 ± 0.03 @ ΔV_c = 92%	~15%
TiO_2-ALD-Circular-Si	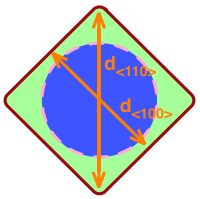	1	1.13 ± 0.04 @ ΔV_c = 88%	~13%
TiO_2-ALD-Square-Si	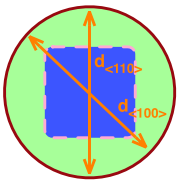	0.71	0.95 ± 0.02 @ ΔV_c = 165%	--

4.3.3 Fracture behavior

It is noted in Fig. 4.2a-c that all silicon pillars exhibit popcorn type fracture patterns, where cracks appear to initiate from the out surface of circular pillars, penetrating into the crystalline core and also propagating along the crystalline-amorphous interfaces. In addition, all pillars (including square ones) seem to fail from one major crack rather than multiple ones. To obtain more quantitative information, we have measured the crack orientations of all four types of silicon pillars. Fig. 4.4 illustrates the statistical crack orientation information for the bare-Circular-Si, ALD circular pillars (both), and TiO_2-ALD-square-Si. Due to the relatively uniform expansion behavior of the bare-Circular-Si, we observe that the crack orientation of these samples is somewhat stochastic with slight preference along <110> direction, Fig. 4.4a; i.e., the reported preferential fracture oriented 45° to <110> direction for (100)-type silicon nanopillars is not observed in our micropillars [26]. For ALD circular pillars, cracks seem to initiate unanimously along <110> direction (i.e., the most swelling direction), Fig. 4.4b, whereas for ALD square pillars, along <100> direction (i.e, one corner of the square), Fig. 4.4c. These fracture orientations are not only drastically different from those of our own bare silicon, but also differ from dominant fracture orientations reported so far in the literature [26], suggesting that the fracture process in silicon micropillars can be quite a complex, which seems affected by the sample size, initial geometry, surface coatings/defects, or even dopant type. In addition, different electrochemical reaction rate used in various experiments could also play a significant role. Note that the different fracture orientations reported in the literature are mainly observed in p-type silicon nanopillars [26], whereas our samples are n-type pillars. Furthermore, there are clear sample size and lithiation condition differences. The

experimental results here underscore the importance of taking into account the strong size effect, initial sample geometry, and electrochemical cycling conditions when designing silicon anode structures for LIBs.

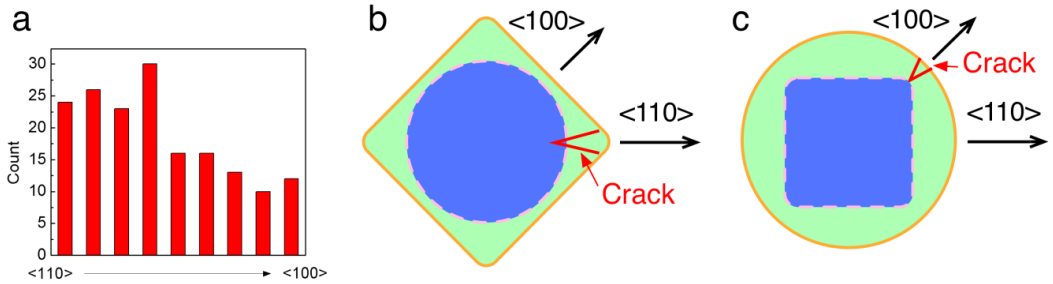

Figure 4.4. Crack orientations for three types of silicon pillars: (a) bare-Circular-Si, (b) ALD-Circular-Si (for both Al_2O_3 and TiO_2 coated), and (c) TiO2-ALD-Square-Si. Note that all ALD-coated pillars ubiqutiously fail along one orientation [either <110> in (b), or <100> in (c)], in contrast to the relatively random failure direction of bare silicon sample in (a).

To further grip the crack growth trends for all four types of pillars studied, we measured the crack length (L) (defined in Fig. 4.5a, where R is the original radius of the pillar) vs. VE for a number of randomly selected pillars. The results are summarized in Fig. 4.5b for all pillars. In the figure, one could gauge the easiness of the crack propagation through examining the slope (K) of L/R vs. VE. A larger K would mean that the crack is prone to propagation under the same VE. We note that, for the bare silicon, the cracks always nucleate from the out surface after a VE of less than 100% and start to grow inwards with a K value of ~2.7. Both ALD-coated samples follow a similar trend (K~2.3) but with a slightly larger x-axis offset compared to the bare silicon, suggesting that ALD coating might have helped to arrest the crack nucleation. We speculate that as our coating thickness is no more than 1 nm (i.e., negligibly thin compared to the sample dimension), the possible mechanical constraint effect is insignificant. This is consistent with similar K values observed for all three circular-shape samples. As mentioned above

and indicated in Fig. 4.5b, the ALD-square pillars reveal a critical VE of 165% that is much larger than the circular ones. This implies a strong delay of crack nucleation and propagation. In addition, we find a K value of ~1.5 for these square pillars, which is also substantially smaller than those of circular ones (2.3-2.7), testifying more difficult event of crack propagation in the square pillars. Based upon the critical VE without fracture (ΔV_c), one can estimate a reversible capacity of ~2300 mAh/g for ALD square pillars, in contrast to a much smaller capacity of ~1400 mAh/g for circular pillars.

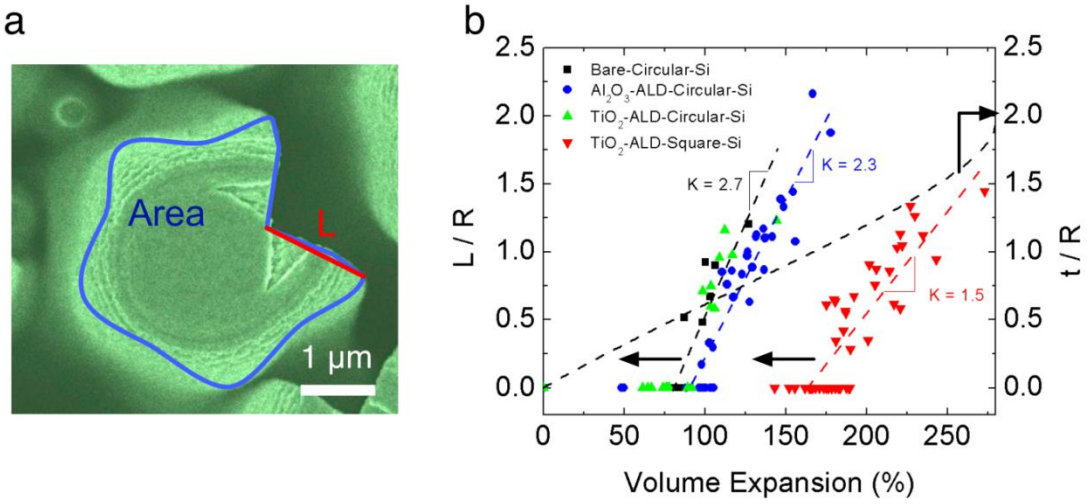

Figure 4.5. Crack nucleation and growth behavior in four types of silicon pillars. (a) The definition of L (crack length) and R (original pillar radius). The ΔV is measured by the change of pillar area on top-view using the ImageJ software. The amorphous shell thickness t is estimated according to eqn. 1 in the main text. (b) The distribution of L/R (y1-axis) and t/R (y2-axis) as a function of the VE. Three L/R dashed lines are the least-squares-fitting of the experimental data with the slope (K) marked in the figure.

Another important question pertaining to the crack propagation is whether the two phase boundary can effectively divert or obstruct the crack propagation. If this occurs, one would expect to see the crack length (L) equal or be smaller than the amorphous shell thickness (t; i.e., lithiated area). Assuming an isotropic VE (ΔV), one can estimate t/R from the total ΔV as:

$$t/R = \sqrt{1+\Delta V} - \sqrt{1-\Delta V/\Delta V_t} \tag{4.1}$$

where ΔV_t represents the theoretical VE of silicon. The calculated t/R trend follows the dashed line shown in Fig. 4.5b. Evidently, L/R values surpass the t/R line for all three circular pillars when the VE is above ~100%, suggesting that the cracks propagate well into the crystalline silicon core for circular pillars, consistent with the SEM image shown in Fig. 4.5a. In contrast, this behavior is not seen for square pillars, which again suggests the difficult event of crack propagation in square geometry. The contrast results between circular and square pillars promote us to argue that the stress state/distribution in these two types of pillars could be very different.

4.4. Theoretical Framework

To understand qualitatively the effect of ALD coating and initial geometry on the VE and stress evolution of silicon micropillars upon lithiation, a two-phase model is developed, following the literature [35, 167]. The model assumes that the rate-limiting processes during the lithiation involve the bulk diffusion of lithium ion through the pillars and the solid state reaction at the interface (i.e., other rate-controlling mechanisms such as adsorption of Li on the surface of silicon pillars are ignored) [148, 248]. As all micropillars used in our experiments have very large aspect ratio (25:1), the effect of the pillar height is negligible; that is, a cross-section representation is sufficient to portray the VE behavior, the Cartesian coordinate setup of which can be seen in the inset of Fig. 4.6a, with the origin coinciding with the geometric center of the cross-section and two axels along <110> directions. Coordinates (x,y) and angle θ are used to specify positions and directions. For the reaction controlled interface motion, interface velocity [148] is determined by $v(\theta) = \lambda_m R$, where λ_m is the molar volume of

crystalline silicon and $R=\kappa(\theta)f(c_{Li},c_{Si},c_{Li-Si})$ is the rate of chemical reaction [here $\kappa(\theta)$ is the orientation dependent rate constant for solid state chemical reaction, and the function $f(c_{Li},c_{Si},c_{Li-Si})$ describes the reaction rate which is a function of the concentrations of products and reactants]. Lithium concentration is assumed saturated in the amorphous phase and zero in the crystalline phase. Thus, function $f(c_{Li},c_{Si},c_{Li-Si})$ becomes a constant at the phase interface. Given the four fold symmetry of the crystal structure in the cross-section, the interface velocity can be described as

$$v(\theta)=\frac{1}{2}(v_{110}+v_{100})+\frac{1}{2}(v_{110}-v_{100})cos(4\theta) \tag{4.2}$$

Here $v_{100}=\lambda_m f\kappa(0)$ and $v_{110}=\lambda_m f\kappa(\pi/4)$ are the interface velocities at [110] and [100] orientations, respectively.

A large deformation method is used in our modeling [249]. The multiplicative decomposition of deformation is assumed so that the total deformation λ_i can be decomposed into three parts, namely, elastic deformation λ_i^e, plastic deformation λ_i^p, and compositional deformation λ_i^c as $\lambda_i=\lambda_i^e\lambda_i^p\lambda_i^c$ (i=1, 2, 3 denotes three principal directions). The compositional strain is given by $\lambda_i^c(x,y;t)=1+\beta c(x,y;t)$, with $c(x,y;t)$ as the normalized lithium concentration, and β as the coefficient of compositional expansion. Elastic and plastic deformation is partitioned by the specific material law. Crystalline silicon is modeled as an cubic elastic material; amorphous Li-Si alloy and ALD coatings are both modeled as isotropic perfectly elastic-plastic materials. The von Mises yielding criterion and the associated flow rules are used to describe the plastic

behavior of amorphous materials. Detailed formulation of equilibrium, compatibility, and constitutional models are available in the reference [249].

The model described above is implemented using the finite element package ABAQUS and two user-subroutines. We draw an analogy between concentration c in our problem and temperature in thermal analysis in ABAQUS. Therefore, a user subroutine UTEMP (user defined temperature) is used to evolve the interface according to the above equation with concentration $c=1$ assigned to the amorphous phase and $c=0$ to the crystalline phase. Another user subroutine UEXPAN is used to compute the compositional expansion based on the concentration field obtained from UTEMP, under rigorous finite deformation formulation. β=0.5874 is used to realize the 300% VE, as $(1+\beta)^3=1+300\%$. The field of compositional strain is passed into ABAQUS main program as the load to deform the electrode.

Table 4.3. Representative mechanical properties of some relevant materials used in simulations

Materials	Mechanical Properties
Amorphous TiO_2	E=65~147 GPa [250]
Amorphous Al_2O_3	E=150-155 GPa, σ_y=2.7 GPa [251]
Amorphous $Li_{15}Si_4$	E=12 GPa, σ_y=0.5-1.0 GPa [170, 223]
Single crystalline Si (100)	E=130 GPa, G=79.6 GPa, υ=0.28 [224, 252]

Tab. 4.3 lists the mechanical properties of materials involved in simulations. For ALD coatings, we choose Young's modulus E=150 GPa, yield strength σ_y=2.7 GPa [250, 251], and Poisson's ratio υ=0.25 as protocol values. For (100) crystalline silicon, E=130 GPa, Shear modulus G=79.6 GPa, and υ=0.28 [224, 252]. For Si-Li amorphous phase, we choose E=12 GPa, σ_y=0.5-1.0 GPa [170, 223], and υ=0.28. All length quantities in the simulations are normalized by a=1000 nm, which is the experimental radius for circular pillar and half-width of square pillar. $\tau=a/v_{110}$ is the time scale of full lithiation; thus time

is normalized by τ and velocity is normalized by a/τ, i.e., $\bar{v}_{110} = v_{110}\tau/a$, $\bar{v}_{100} = v_{100}\tau/a$. For bare and ALD-coated pillars, the same velocity in 110 orientation was used as $\bar{v}_{110} = 1$ while different values $\bar{v}_{100} = 0.9$ and $\bar{v}_{100} = 0.6$ were used respectively to recognize the different levels of the anisotropy in these two kinds of samples; i.e., the different rate-limiting mechanisms are represented in the model by controlling the levels of reaction front velocity anisotropy for simplicity. ALD coating was modeled as a thin layer of material with a normalized thickness of 0.005.

4.5. Modeling Results and Discussion

The key purpose of this phenomenological model is to help understand very different fracture behavior observed with and without ALD coatings, and the strong sample geometry effect observed in our work. Note that earlier in-situ transmission electron microscopy experiments revealed a strong orientation-dependent interface mobility during lithiation of silicon nanowires [36, 40], which has been the basis of many existing modeling effort [36, 39]. Our experiments here on the bare silicon pillars however indicate that the lithiation behavior of silicon materials is strongly influenced by the formation of SEI layers, which regulates/limits the lithium ion transport such that the interface mobility could become less relevant. In fact and as indicated by the modeling results shown in Fig. 4.6a-l, a relatively uniform VE behavior is obtained when the interface velocity difference is less than 10% along the <110> and <100> directions; i.e., the rate controlling mechanism in our bare silicon micropillars is likely to be the diffusion of lithium ion into the reaction front. Under these conditions, our simulations indicate that the corresponding hoop stresses (Fig. 4.6a) along <110> (σ_{110}) and <100> (σ_{100}) directions are initially compressive but quickly turn over to the positive territory

(i.e., tensile). Right before the fracture (i.e., at the VE ~82%), both stresses are clearly tensile and exhibit essentially the same values. These results agree quantitatively with relatively stochastic fracture orientations of bare silicon micropillars observed in our experiments. In contrast, an obviously anisotropic VE behavior is duplicated when the solid state reaction is assumed to control the VE behavior of ALD samples, Fig. 4.6e-l. Under this scenario, the hoop stresses go through a similar transition from compressive to tensile with the major difference that the hoop stress along <110> direction (i.e., σ_{110}) is appreciably higher than σ_{100}, leading to preferential fracture of these pillars long <110> orientation (as observed in our experiments).

Interestingly, the round shape expansion behavior of ALD square pillars is also reproduced when the solid state reaction is assumed to control the lithiation behavior of these pillars, the hoop stresses of which exhibit a cross-over behavior between <100> and <110> orientations. The hoop stress along <100> orientation is observed to be higher when the VE is less than ~125%, which is gradually overtaken by the stress along <110> direction. The gradual decrease of σ_{100} as VE increases is observed to be linked with the stress relaxation along the corner of the square (Fig. 4.6i), suggesting that the square pillars has the ability to homogenize the stress distribution and slow down the crack nucleation or growth. The final fracture of these pillars along <100> direction seems pertaining to the groove development observed in our simulations, Fig. 4.6j-l. Note that the fracture toughness in bulk silicon is orientation dependent, with the value along <110> direction slightly lower than that of <100> direction (Tab. 4.1). This small fracture toughness discrepancy however does not seem to affect the fracture orientation of square pillars. The rather complex stress evolution and much larger achievable VE in these pillars suggest that square geometry can be more desirable for applications in LIBs.

It is further suggested that investigations of other geometry pillars are useful in order to fully understand the initial geometric effect of silicon crystalline materials upon lithiation behavior.

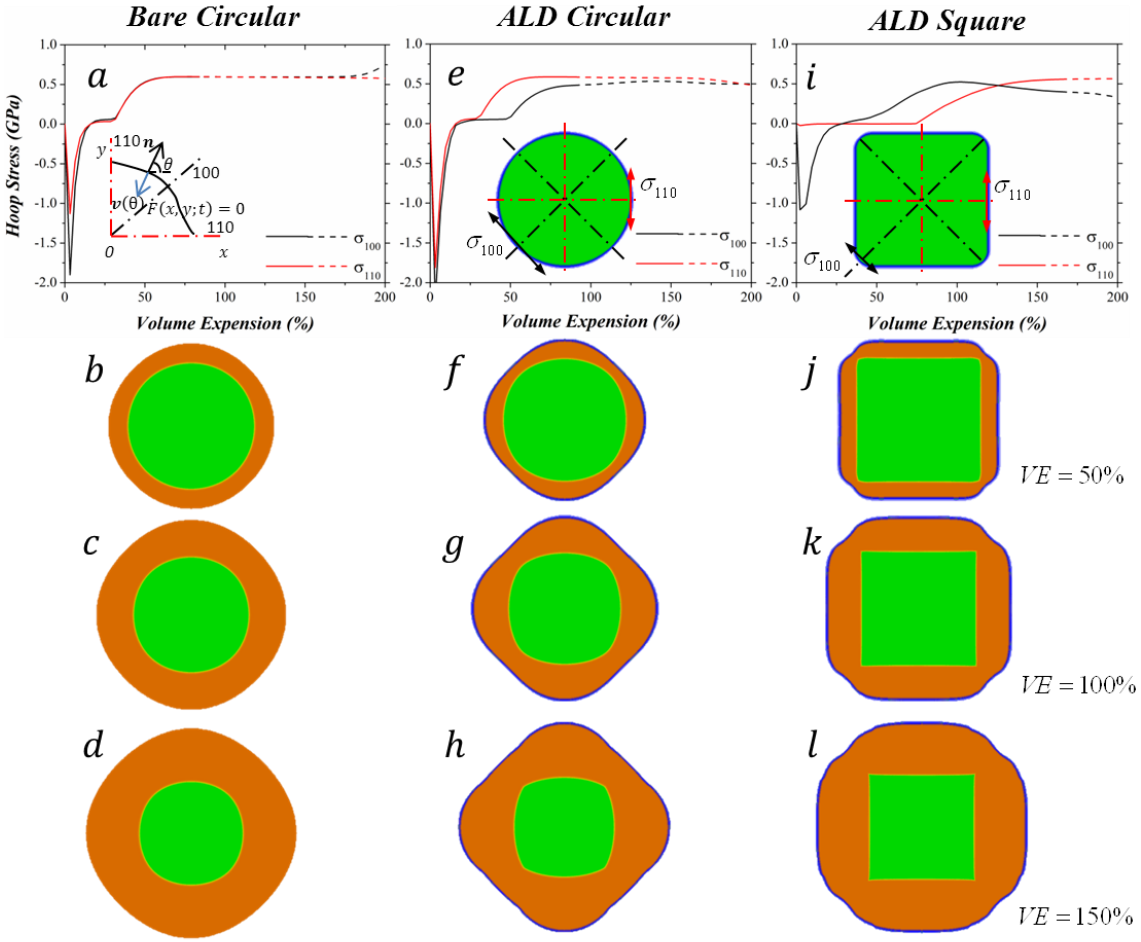

Figure 4.6. Finite element simulation results for (a-d) bare-Circular-Si, (e-h) ALD-coated circular pillars, and (i-l) ALD-coated square pillars. (a) Hoop stress as a function of VE at the surface of the bare-Circular-Si perpendicular to <100> (black line) and <110> (red line) directions, respectively. The inset is the coordinate setup for simulations. (b-d). The shape change in cross-section of the bare-Circular-Si, with crystalline Si in green and amorphous Li-Si in orange at different VE of 50%, 100%, 150%, respectively. The definition of hoop stress and shape change in (e-h) and (i-l) follows the same order as the bare-Circular-Si. Note the rather anisotropic expansion behavior after ALD-coating for circular pillars (f-h), and the near circle-like expansion behavior of the square pillars (j-l). The ALD thin coating in (f-h) and (j-l) is represented by the blue solid line.

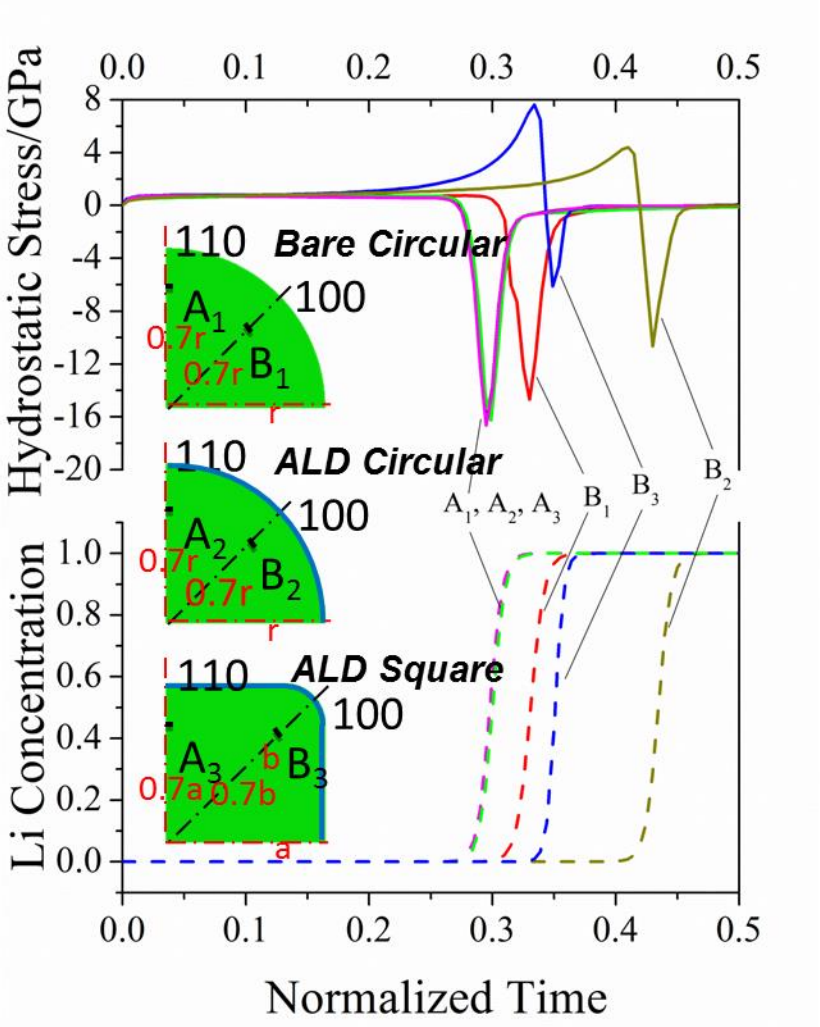

Figure 4.7. The hydrostatic stress distribution of two selected points for three types of silicon pillars. The reaction front propagation can be viewed from the Li concentration profile corresponding to each position (i.e., A_1, A_2, A_3, B_1, B_2, B_3). Note the development of tensile hydrostatic stress at point B_2 and B_3 as the reaction front propagates.

Although our models have not taken into account the change of the reaction-front velocity due to the development of compressive/tensile stresses and the effect of stress on diffusivity (which might influence the interface migration kinetics), our hydrostatic stress analysis of two different selected positions located at the trajectories (along <100> and <110> orientations) of the migrating reaction front interface shown in Fig. 4.7

indicates the development of tensile hydrostatic stress inside crystalline core along the [100] direction in both ALD-samples (see point B2 and B3 in Fig. 4.7) when the reaction front propagates, suggesting the possible speedup of reaction front velocity in that orientation – a behavior that seems to contrast with some reports in nanosized silicon (e.g., nanoparticles or nanowires) [17, 29, 149]. This could have several important implications for silicon micropillars compared to nanopillars. First, the reaction front velocity change seems to help promote less anisotropic expansion due to the reason mentioned above (i.e., the speedup tendency along [100] orientation). Second, the effect of hydrostatic compression on diffusivity stemming from the curvature of the reaction front interface could be less significant in micropillars due to the relatively low curvature of micro-sized pillars [29]. The relatively fast lithiation in the late stage of holding time seen in Fig. 4.1h appears consistent with this speculation. Note however that this type of accelerated lithiation processes could also be caused by the fracture of silicon pillars, leading to the relaxation of stresses and fresh free surface for fast surface lithium diffusion and continuous lithiation. Third, due to the much large dimensions associated with micropillars (compared to nanopillars), it is conceivable that diffusion controlled processes is expected to play more significant roles in the late stage of lithiation in micropillars, which could lead to less anisotropic expansion behavior. This seems to be true in both bare- and ALD-coated-samples where less anisotropy is observed compared to those reported in silicon nanopillars. In essence, the lithiation kinetics of silicon micropillars could be very different from those of silicon nanopillars. Because of above reasons, our model assumption of different levels of reaction front velocity anisotropy for different controlling mechanisms, i.e., less anisotropic velocity for the diffusion-controlled mechanism and more anisotropic velocity for the reaction-controlled

mechanism, and constant reaction front velocity seems reasonable to capture the essences of shape change of all three types of pillars, as well as the fracture orientations even though the time-dependent variation of the reaction front velocity in the case of the diffusion-controlled mechanism is not considered. We observe different rate controlling mechanisms in bare and ALD pillars, with very different hoop stress development that is closely related to the shape of the pillars. One additional point that is worth pointing out is most existing models do not account for crystallographic orientation dependent velocity change due to the different stresses development along different orientations, which could lead to less/more velocity discrepancy in [110] and [100] orientations. More complete models that can account for all above factors are clearly needed in the future in order to fully address the rather complicated lithiation behavior seen in microsized silicon pillars.

4.6. Conclusion and Outlook

In summary, we have investigated the initial lithiation behavior of (100) n-type silicon micropillars in three different forms: bare circular silicon, ALD-coated circular silicon, and ALD-coated square silicon pillars. In contrast to what has been reported in the literature on nanostructures, the bare silicon micropillars studied here exhibit a relatively uniform VE behavior before fracturing along somewhat stochastic directions, likely due to the regulation effect of SEI layers in controlling lithium ion flux. ALD coating of metal oxides (Al_2O_3 and TiO_2) help to form thin SEI layers and enhance lithium transportation, leading to a strong anisotropic VE behavior. With or without ALD coatings, the critical VE before fracture for all circular pillars reaches up to ~100%. With a further square-shaped geometry design, however, a critical VE of more than 165% can be reached, helped by the stress relaxation mechanisms around the corners of

squares. Models are developed that are able to rationalize the overall VE and fracture behavior of all pillars. Simulations further suggest that stress distributions in various pillars may play significant roles in the fracture behavior. These findings underscore the critical importance of SEI formation in regulating the transport and eventual failure mechanisms of various pillars. ALD-coated metal oxides can act as a gate that promotes fast Li-ion diffusion into the bulk electrode and subsequently change the lithium diffusion kinetics. Questions remain what the optimized thickness of these ALD coatings would be in order to maximize Li-ion transport yet help maintain the integrity of the electrodes. Nonetheless, our results offer new insights in designing silicon-based electrodes for high energy density and high-power density electrochemical energy storage.

CHAPTER 5

CONCLUSION

5.1. Summary

In summary, mechanics of silicon electrodes in LIBS are studied from three aspects in this dissertation, the coupling of finite deformation and mass diffusion in large silicon electrodes, the anisotropic interface reaction and geometry design of nano crystal electrodes, and enhanced lithiation and fracture behavior of silicon pillars via atomic layer coatings and geometry design.

In Chapter 2, we develop a finite element based numerical method to study the coupled large deformation and diffusion in large silicon electrodes in LIB. The coupling is realized by an analogy between diffusion and thermal transfer in ABAQUS. Due to the large deformation, this analogy is rigorously examined and the corresponding relation is established. It is found that this formulation is able to realize the coupled deformation and diffusion in large deformation using several user-defined subroutines in ABAQUS, namely user-defined thermal transport (UMATHT), user-defined flux (UFLUX) and user-defined expansion (UEXPAN). Because the present formulation does not involve any element development in ABAUQS, many built-in modules can be directly utilized. A system comprising three components, namely, Si electrode, binder, and current collector, is studied using the cohesive elements and the damage of the electrode is considered. It is anticipated that this formulation is able to model many coupled large deformation and diffusion problems in electrodes with complex spatial and temporal conditions, such as damage evolution, fracture, and electrodes/binder delamination, among others. When this formulation is combined with experimental work, it is expected that the constitutive

relations (e.g., stress versus SOC) can be extracted from various techniques, such as micro-indentation.

In Chapter 3, by incorporating the information from both experiments and calculation at atomic scale, and taking into account the crystallography of silicon, a new continuum model for reaction controlled interface migration is developed, with both the theoretical formulation and numerical implementation applicable to structures with any two/three dimensional geometry. Compared to previous works [39], our model has following merits. I. It is a truly 3D model formulated self-consistenlyt and generally. II. All the model parameters have clear physical significance and measurable directly in experiment. III. The model can be extended easily under the same numerical implementation as long as more information on the ACI velocity is available, from experiments or atomic calculations. When applied to circular/spherical electrode, our model finds some very interesting phenomena such as formation of faceted crystal core and plastic instability, and successfully captures the morphology evolution and the kinetics in the electrode, well agreed with the reported experiments. A new polygon/polyhedron design philosophy is proposed based on the findings from simulation, and is demonstrated to be beneficial to the electrode in short/long term mechanical integrity, and rate performance.

In Chapter 4, we have investigated the initial lithiation behavior of (100) n-type silicon micropillars in three different forms: bare circular silicon, ALD-coated circular silicon, and ALD-coated square silicon pillars. In contrast to what has been reported in the literature on nanostructures, the bare silicon micropillars studied here exhibit a relatively uniform VE behavior before fracturing along somewhat stochastic directions, likely due to the regulation effect of SEI layers in controlling lithium ion flux. ALD

coating of metal oxides (Al_2O_3 and TiO_2) help to form thin SEI layers and enhance lithium transportation, leading to a strong anisotropic VE behavior. With or without ALD coatings, the critical VE before fracture for all circular pillars reaches up to ~100%. With a further square-shaped geometry design, however, a critical VE of more than 165% can be reached, helped by the stress relaxation mechanisms around the corners of squares, the observation partially verified our proposed principle for geometry design in Chapter 3. Models are developed that are able to rationalize the overall VE and fracture behavior of all pillars. Simulations further suggest that stress distributions in various pillars may play significant roles in the fracture behavior. Nonetheless, our results offer new insights in designing silicon-based electrodes for high energy density and high-power density electrochemical energy storage.

5.2. Future Work

When the anisotropic interface reaction is considered for nano electrodes in Chapter 3, the influence of stress and deformation on the kinetics of the phase transformation were not considered. For the large deformation problem of silicon electrodes in LIB, the dependence of phase transformation on stress and deformation could bring interesting perspectives on this subject. For example, in Fig. 5.1, we plotted the color map of phases and maximum in-plane stress on the deformed cross section of circular nanowires of all four orientations at early stage of the lithiation, $\tau = 0.1$. As shown, there is severe stress concentration at the sharp corners of the crystal cores through all cases. This large magnitude of stress is somewhat unrealistic and expected to resist the local interface migration, and effectively round off the sharp corners, when the stress dependent kinetics of phase transformation is considered.

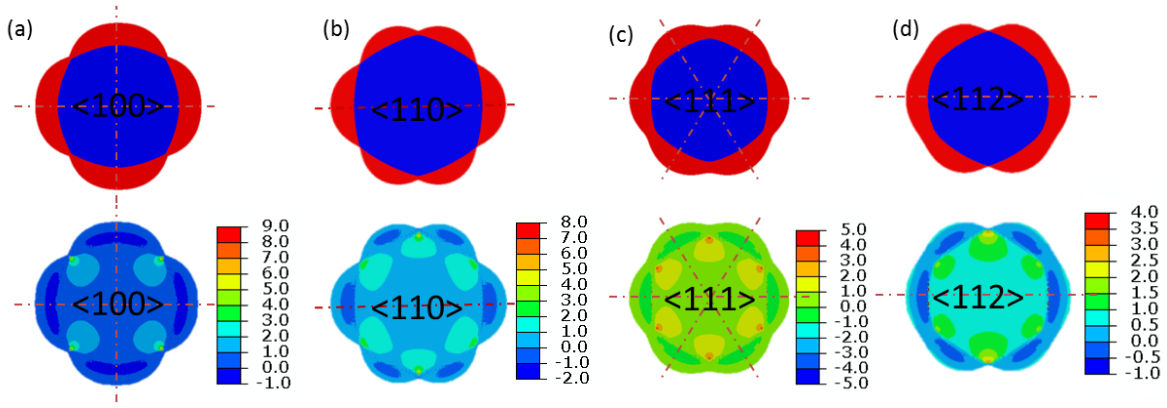

Figure 5.1. Color map of phases (amorphous phase in red, crystal in blue) and maximum in-plane stress (in unit of GPa) on the deformed cross section of (a) <100>; (b) <110>; (c) <111>; (d) <112> crystal silicon nanowires after partially lithiated ($\tau = 0.1$), with red dash line label the in-plane <110> orientations and stress concentrated at the sharp corners of the faceted crystal core.

In addition, we assumed in this dissertation the separated diffusion controlled and interface controlled kinetics for large electrodes and small electrodes respectively. A unified model is in need to consider the competition between the diffusion controlled kinetics and the interface controlled kinetics, with an intrinsic length scale. With the new model, the size effect as well as the transition between diffusion controlled and interface controlled kinetics in the silicon electrodes could be investigated thoroughly. Noting that the diffusion in silicon is isotropic while the interface reaction could be anisotropic, the size dependent anisotropy of the lithiation/delithiation kinetics is expected in this model.

REFERENCES

1. Whittingham, M.S., *Electrical Energy Storage and Intercalation Chemistry*. Science, 1976. **192**(4244): p. 1126-1127.

2. Zanini, M., S. Basu, and J.E. Fischer, *Alternate Synthesis And Reflectivity Spectrum Of Stage 1 Lithium—Graphite Intercalation Compound*. Carbon, 1978. **16**(3): p. 211-212.

3. Basu, S., et al., *Synthesis and properties of lithium-graphite intercalation compounds*. Materials Science and Engineering, 1979. **38**(3): p. 275-283.

4. Goodenough, J., et al., *Electrochemical cell with new fast ion conductors*. *US* 4302518, 1981.

5. Goodenough, J., et al., *Fast ion conductors*. *US* 4357215, 1981.

6. Yazami, R. and P. Touzain, *A reversible graphite-lithium negative electrode for electrochemical generators*. Journal of Power Sources, 1983. **9**(3): p. 365-371.

7. Thackeray, M.M., et al., *Lithium Insertion Into Manganese Spinels*. Materials Research Bulletin, 1983. **18**(4): p. 461-472.

8. Manthiram, A. and J.B. Goodenough, *Lithium insertion into Fe2(SO4)3 frameworks*. Journal of Power Sources, 1989. **26**(3–4): p. 403-408.

9. Padhi, A.K., K.S. Nanjundaswamy, and J.B. Goodenough, *Phospho-olivines as Positive-Electrode Materials for Rechargeable Lithium Batteries*. Journal of the Electrochemical Society, 1997. **144**(4): p. 1188-1194.

10. Chung, S.Y., J.T. Bloking, and Y.M. Chiang, *Electronically conductive phospho-olivines as lithium storage electrodes*. Nature Materials, 2002. **1**(2): p. 123-128.

11. Xu, Y.N., W.Y. Ching, and Y.M. Chiang, *Comparative studies of the electronic structure of LiFePO4, FePO4, Li3PO4, LiMnPO4, LiCoPO4, and LiNiPO4*. Journal of Applied Physics, 2004. **95**(11): p. 6583-6585.

12. Xu, Y.N., et al., *Electronic structure and electrical conductivity of undoped LiFePO4*. Electrochemical and Solid State Letters, 2004. **7**(6): p. A131-A134.

13. Chan, C.K., et al., *High-performance lithium battery anodes using silicon nanowires*. Nature Nanotechnology, 2008. **3**(1): p. 31-35.

14. Chan, C.K., et al., *Solution-Grown Silicon Nanowires for Lithium-Ion Battery Anodes*. Acs Nano, 2010. **4**(3): p. 1443-1450.

15. Hu, L.B., et al., *Thin, Flexible Secondary Li-Ion Paper Batteries*. Acs Nano, 2010. **4**(10): p. 5843-5848.

16. Liu, N.A., et al., *Prelithiated Silicon Nanowires as an Anode for Lithium Ion Batteries*. Acs Nano, 2011. **5**(8): p. 6487-6493.

17. McDowell, M.T., et al., *Studying the Kinetics of Crystalline Silicon Nanoparticle Lithiation with In Situ Transmission Electron Microscopy*. Advanced Materials, 2012. **24**(45): p. 6034-+.

18. Yao, Y., et al., *Improving the cycling stability of silicon nanowire anodes with conducting polymer coatings*. Energy & Environmental Science, 2012. **5**(7): p. 7927-7930.

19. Choi, N.S., et al., *One dimensional Si/Sn - based nanowires and nanotubes for lithium-ion energy storage materials*. Journal of Materials Chemistry, 2011. **21**(27): p. 9825-9840.

20. Ryu, I., et al., *Size-dependent fracture of Si nanowire battery anodes*. Journal of the Mechanics and Physics of Solids, 2011. **59**(9): p. 1717-1730.

21. Lee, S.W., et al., *Anomalous Shape Changes of Silicon Nanopillars by Electrochemical Lithiation*. Nano Letters, 2011. **11**(7): p. 3034-3039.

22. McDowell, M.T., et al., *In Situ TEM of Two-Phase Lithiation of Amorphous Silicon Nanospheres*. Nano Letters, 2013. **13**(2): p. 758-764.

23. Yang, Y., et al., *New Nanostructured Li2S/Silicon Rechargeable Battery with High Specific Energy*. Nano Letters, 2010. **10**(4): p. 1486-1491.

24. Pasta, M., et al., *A high-rate and long cycle life aqueous electrolyte battery for grid-scale energy storage*. Nature Communications, 2012. **3**.

25. Wu, H., et al., *Stable cycling of double-walled silicon nanotube battery anodes through solid-electrolyte interphase control*. Nature Nanotechnology, 2012. **7**(5): p. 309-314.

26. Lee, S.W., et al., *Fracture of crystalline silicon nanopillars during electrochemical lithium insertion*. Proceedings of the National Academy of Sciences of the United States of America, 2012. **109**(11): p. 4080-4085.

27. Yang, Y., et al., *Transparent lithium-ion batteries*. Proceedings of the National Academy of Sciences of the United States of America, 2011. **108**(32): p. 13013-13018.

28. Kushima, A., J.Y. Huang, and J. Li, *Quantitative Fracture Strength and Plasticity Measurements of Lithiated Silicon Nanowires by In Situ TEM Tensile Experiments*. Acs Nano, 2012. **6**(11): p. 9425-9432.

29. Liu, X.H., et al., *Self-Limiting Lithiation in Silicon Nanowires*. Acs Nano, 2013. **7**(2): p. 1495-1503.

30. Liu, X.H., et al., *Size-Dependent Fracture of Silicon Nanoparticles During Lithiation*. Acs Nano, 2012. **6**(2): p. 1522-1531.

31. Liu, X.H., et al., *In Situ TEM Experiments of Electrochemical Lithiation and Delithiation of Individual Nanostructures*. Advanced Energy Materials, 2012. **2**(7): p. 722-741.

32. Liu, X.H. and J.Y. Huang, *In situ TEM electrochemistry of anode materials in lithium ion batteries*. Energy & Environmental Science, 2011. **4**(10): p. 3844-3860.

33. Kushima, A., et al., *Leapfrog Cracking and Nanoamorphization of ZnO Nanowires during In Situ Electrochemical Lithiation*. Nano Letters, 2011. **11**(11): p. 4535-4541.

34. Liu, X.H., et al., *Reversible Nanopore Formation in Ge Nanowires during Lithiation-Delithiation Cycling: An In Situ Transmission Electron Microscopy Study*. Nano Letters, 2011. **11**(9): p. 3991-3997.

35. Liu, X.H., et al., *Ultrafast Electrochemical Lithiation of Individual Si Nanowire Anodes*. Nano Letters, 2011. **11**(6): p. 2251-2258.

36. Liu, X.H., et al., *Anisotropic Swelling and Fracture of Silicon Nanowires during Lithiation*. Nano Letters, 2011. **11**(8): p. 3312-3318.

37. Liu, Y., et al., *In Situ Transmission Electron Microscopy Observation of Pulverization of Aluminum Nanowires and Evolution of the Thin Surface Al2O3 Layers during Lithiation-Delithiation Cycles*. Nano Letters, 2011. **11**(10): p. 4188-4194.

38. Wang, J.W., et al., *Two-Phase Electrochemical Lithiation in Amorphous Silicon*. Nano Letters, 2013. **13**(2): p. 709-715.

39. Yang, H., et al., *Orientation-Dependent Interfacial Mobility Governs the Anisotropic Swelling in Lithiated Silicon Nanowires*. Nano Letters, 2012. **12**(4): p. 1953-1958.

40. Liu, X.H., et al., *In situ atomic-scale imaging of electrochemical lithiation in silicon*. Nature Nanotechnology, 2012. **7**(11): p. 749-756.

41. Zhong, L., et al., *Multiple-Stripe Lithiation Mechanism of Individual SnO2 Nanowires in a Flooding Geometry*. Physical Review Letters, 2011. **106**(24).

42. Thotiyl, M.M.O., et al., *A stable cathode for the aprotic Li-O-2 battery*. Nature Materials, 2013. **12**(11): p. 1049-1055.

43. Chen, Y.H., et al., *Charging a Li-O-2 battery using a redox mediator*. Nature Chemistry, 2013. **5**(6): p. 489-494.

44. Peng, Z.Q., et al., *A Reversible and Higher-Rate Li-O-2 Battery*. Science, 2012. **337**(6094): p. 563-566.

45. Chen, Y., et al., *Li-O-2 Battery with a Dimethylformamide Electrolyte*. Journal of the American Chemical Society, 2012. **134**(18): p. 7952-7957.

46. Armstrong, A.R., et al., *The lithium intercalation process in the low-voltage lithium battery anode Li1+xV1-xO2*. Nature Materials, 2011. **10**(3): p. 223-229.

47. Armstrong, A.R., et al., *Demonstrating oxygen loss and associated structural reorganization in the lithium battery cathode Li[Ni0.2Li0.2Mn0.6]O-2*. Journal of the American Chemical Society, 2006. **128**(26): p. 8694-8698.

48. Tompsett, D.A., et al., *Nanostructuring of beta-MnO2: The Important Role of Surface to Bulk Ion Migration*. Chemistry of Materials, 2013. **25**(4): p. 536-541.

49. Thotiyl, M.M.O., et al., *The Carbon Electrode in Nonaqueous Li-O-2 Cells*. Journal of the American Chemical Society, 2013. **135**(1): p. 494-500.

50. Choi, N.S., et al., *Challenges Facing Lithium Batteries and Electrical Double-Layer Capacitors*. Angewandte Chemie-International Edition, 2012. **51**(40): p. 9994-10024.

51. Bruce, P.G., et al., *Li-O-2 and Li-S batteries with high energy storage*. Nature Materials, 2012. **11**(1): p. 19-29.

52. Armstrong, A.R., et al., *Lithium Coordination Sites in LixTiO2(B): A Structural and Computational Study*. Chemistry of Materials, 2010. **22**(23): p. 6426-6432.

53. Kovalenko, I., et al., *A Major Constituent of Brown Algae for Use in High-Capacity Li-Ion Batteries*. Science, 2011. **334**(6052): p. 75-79.

54. Magasinski, A., et al., *High-performance lithium-ion anodes using a hierarchical bottom-up approach*. Nature Materials, 2010. **9**(4): p. 353-358.

55. Schauer, M.W., et al., *Carbon nanotube material for battery applications*. Abstracts of Papers of the American Chemical Society, 2013. **245**.

56. Evanoff, K., et al., *Ultra Strong Silicon-Coated Carbon Nanotube Nonwoven Fabric as a Multifunctional Lithium-Ion Battery Anode*. Acs Nano, 2012. **6**(11): p. 9837-9845.

57. Wei, L., N. Nitta, and G. Yushin, *Lithographically Patterned Thin Activated Carbon Films as a New Technology Platform for On-Chip Devices*. Acs Nano, 2013. **7**(8): p. 6498-6506.

58. Evanoff, K., et al., *Towards Ultrathick Battery Electrodes: Aligned Carbon Nanotube - Enabled Architecture*. Advanced Materials, 2012. **24**(4): p. 533-+.

59. Newman, J.S. and K.E. Thomas-Alyea, *Electrochemical systems*2004, Hoboken, N.J: J. Wiley.

60. Egashira, M., et al., *Measurement of the electrochemical oxidation of organic electrolytes used in lithium batteries by microelectrode*. Journal of Power Sources, 2001. **92**(1-2): p. 267-271.

61. Hayashi, K., et al., *Mixed solvent electrolyte for high voltage lithium metal secondary cells*. Electrochimica Acta, 1999. **44**(14): p. 2337-2344.

62. Imhof, R. and P. Novak, *Oxidative electrolyte solvent degradation in lithium-ion batteries - An in situ differential electrochemical mass spectrometry investigation*. Journal of the Electrochemical Society, 1999. **146**(5): p. 1702-1706.

63. Xu, K., *Nonaqueous liquid electrolytes for lithium-based rechargeable batteries*. Chemical Reviews, 2004. **104**(10): p. 4303-4417.

64. Garcia, B., et al., *Room temperature molten salts as lithium battery electrolyte*. Electrochimica Acta, 2004. **49**(26): p. 4583-4588.

65. Koch, V.R., et al., *The intrinsic anodic stability of several anions comprising solvent-free ionic liquids*. Journal of the Electrochemical Society, 1996. **143**(3): p. 798-803.

66. Markevich, E., V. Baranchugov, and D. Aurbach, *On the possibility of using ionic liquids as electrolyte solutions for rechargeable 5 V Li ion batteries*. Electrochemistry Communications, 2006. **8**(8): p. 1331-1334.

67. Stassen, I. and G. Hambitzer, *Metallic lithium batteries for high power applications*. Journal of Power Sources, 2002. **105**(2): p. 145-150.

68. Zinck, L., et al., *Purification process for an inorganic rechargeable lithium battery and new safety concepts*. Journal of Applied Electrochemistry, 2006. **36**(11): p. 1291-1295.

69. Armand, M.B., J.M. Chabagno, and M.J. Duclot, *Poly-ethers as solid electrolytes*. Fast Ion Transport in Solids. Electrodes and Electrolytes, 1979: p. 131-6.

70. Nishimoto, A., et al., *High ionic conductivity of new polymer electrolytes based on high molecular weight polyether comb polymers*. Electrochimica Acta, 1998. **43**(10-11): p. 1177-1184.

71. Wright, P.V., *Electrical conductivity in ionic complexes of poly(ethylene oxide)*. British Polymer Journal, 1975. **7**(5): p. 319-27.

72. Adachi, G.Y., N. Imanaka, and H. Aono, *Fast Li-circle plus conducting ceramic electrolytes*. Advanced Materials, 1996. **8**(2): p. 127-&.

73. Kim, Y., J. Saienga, and S.W. Martin, *Anomalous ionic conductivity increase in Li2S+GeS2+GeO2 glasses*. Journal of Physical Chemistry B, 2006. **110**(33): p. 16318-16325.

74. Machida, N., et al., *All-solid-state lithium battery with LiCo(0.3)Ni(0.7)O(2) fine powder as cathode materials with an amorphous sulfide electrolyte*. Journal of the Electrochemical Society, 2002. **149**(6): p. A688-A693.

75. Pradel, A. and M. Ribes, *Lithium Chalcogenide Conductive Glasses*. Materials Chemistry and Physics, 1989. **23**(1-2): p. 121-142.

76. He, L., J.Q. Lu, and H.Q. Jiang, *Controlled Carbon-Nanotube Junctions Self-Assembled from Graphene Nanoribbons*. Small, 2009. **5**(24): p. 2802-2806.

77. Stournara, M.E. and V.B. Shenoy, *Enhanced Li capacity at high lithiation potentials in graphene oxide*. Journal of Power Sources, 2011. **196**(13): p. 5697-5703.

78. Mukherjee, R., et al., *Photothermally Reduced Graphene as High-Power Anodes for Lithium-Ion Batteries*. Acs Nano, 2012. **6**(9): p. 7867-7878.

79. Dahn, J.R., et al., *Mechanisms for Lithium Insertion in Carbonaceous Materials*. Science, 1995. **270**(5236): p. 590-593.

80. Gu, W.T., N. Peters, and G. Yushin, *Functionalized carbon onions, detonation nanodiamond and mesoporous carbon as cathodes in Li-ion electrochemical energy storage devices*. Carbon, 2013. **53**: p. 292-301.

81. Bates, J.B., et al., *Thin-film lithium and lithium-ion batteries*. Solid State Ionics, 2000. **135**(1-4): p. 33-45.

82. Besenhard, J.O., J. Yang, and M. Winter, *Will advanced lithium-alloy anodes have a chance in lithium-ion batteries?* Journal of Power Sources, 1997. **68**(1): p. 87-90.

83. Benson, J., et al., *Chemical Vapor Deposition of Aluminum Nanowires on Metal Substrates for Electrical Energy Storage Applications*. Acs Nano, 2012. **6**(1): p. 118-125.

84. Green, M., et al., *Structured silicon anodes for lithium battery applications*. Electrochemical and Solid State Letters, 2003. **6**(5): p. A75-A79.

85. Kavan, L., et al., *Lithium storage in nanostructured TiO2 made by hydrothermal growth*. Chemistry of Materials, 2004. **16**(3): p. 477-485.

86. Poizot, P., et al., *Nano-sized transition-metaloxides as negative-electrode materials for lithium-ion batteries*. Nature, 2000. **407**(6803): p. 496-499.

87. Aydinol, M.K., et al., *Ab initio study of lithium intercalation in metal oxides and metal dichalcogenides*. Physical Review B, 1997. **56**(3): p. 1354-1365.

88. Idota, Y., et al., *Tin-based amorphous oxide: A high-capacity lithium-ion-storage material*. Science, 1997. **276**(5317): p. 1395-1397.

89. Boukhalfa, S., K. Evanoff, and G. Yushin, *Atomic layer deposition of vanadium oxide on carbon nanotubes for high-power supercapacitor electrodes*. Energy & Environmental Science, 2012. **5**(5): p. 6872-6879.

90. Ruffo, R., et al., *Electrochemical behavior of LiCoO2 as aqueous lithium-ion battery electrodes*. Electrochemistry Communications, 2009. **11**(2): p. 247-249.

91. Kim, D.K., et al., *Spinel LiMn2O4 Nanorods as Lithium Ion Battery Cathodes*. Nano Letters, 2008. **8**(11): p. 3948-3952.

92. Dubarry, M., et al., *Evaluation of commercial lithium-ion cells based on composite positive electrode for plug-in hybrid electric vehicle applications. Part I: Initial characterizations*. Journal of Power Sources, 2011. **196**(23): p. 10328-10335.

93. Kim, H., J.T. Lee, and G. Yushin, *High temperature stabilization of lithium-sulfur cells with carbon nanotube current collector*. Journal of Power Sources, 2013. **226**: p. 256-265.

94. Padhi, A.K., K.S. Nanjundaswamy, and J.B. Goodenough, *Phospho-olivines as positive-electrode materials for rechargeable lithium batteries*. Journal of the Electrochemical Society, 1997. **144**(4): p. 1188-1194.

95. Peng, H.L., et al., *Shape Evolution of Layer-Structured Bismuth Oxychloride Nanostructures via Low-Temperature Chemical Vapor Transport*. Chemistry of Materials, 2009. **21**(2): p. 247-252.

96. Kang, B. and G. Ceder, *Battery materials for ultrafast charging and discharging*. Nature, 2009. **458**(7235): p. 190-193.

97. Dong, Y.Z., et al., *The Prepared and Electrochemical Property of Mg Doped LiMnPO4 Nanoplates as Cathode Materials for Lithium-Ion Batteries*. Journal of the Electrochemical Society, 2012. **159**(7): p. A995-A998.

98. Liu, J.L., et al., *Electrochemical reaction of lithium with CoCl2 in nonaqueous electrolyte*. Electrochemistry Communications, 2011. **13**(3): p. 269-271.

99. Groult, H., et al., *Study of Co-Sn and Ni-Sn alloys prepared in molten chlorides and used as negative electrode in rechargeable lithium battery*. Electrochimica Acta, 2011. **56**(6): p. 2656-2664.

100. Cabana, J., et al., *Beyond Intercalation-Based Li-Ion Batteries: The State of the Art and Challenges of Electrode Materials Reacting Through Conversion Reactions*. Advanced Materials, 2010. **22**(35): p. E170-E192.

101. Yao, Y., et al., *Highly Conductive, Mechanically Robust, and Electrochemically Inactive TiC/C Nanofiber Scaffold for High-Performance Silicon Anode Batteries*. Acs Nano, 2011. **5**(10): p. 8346-8351.

102. Wang, D., et al., *Self-Assembled TiO2-Graphene Hybrid Nanostructures for Enhanced Li-Ion Insertion*. Acs Nano, 2009. **3**(4): p. 907-914.

103. Wang, H.L., et al., *Mn3O4-Graphene Hybrid as a High-Capacity Anode Material for Lithium Ion Batteries*. Journal of the American Chemical Society, 2010. **132**(40): p. 13978-13980.

104. Wang, H.L., et al., *Graphene-Wrapped Sulfur Particles as a Rechargeable Lithium-Sulfur Battery Cathode Material with High Capacity and Cycling Stability*. Nano Letters, 2011. **11**(7): p. 2644-2647.

105. Zheng, G.Y., et al., *Hollow Carbon Nanofiber-Encapsulated Sulfur Cathodes for High Specific Capacity Rechargeable Lithium Batteries*. Nano Letters, 2011. **11**(10): p. 4462-4467.

106. Liu, N., et al., *A Yolk-Shell Design for Stabilized and Scalable Li-Ion Battery Alloy Anodes*. Nano Letters, 2012. **12**(6): p. 3315-3321.

107. Kim, I.T., et al., *Synthesis and electrochemical performance of reduced graphene oxide/maghemite composite anode for lithium ion batteries*. Carbon, 2013. **52**: p. 56-64.

108. Lee, H.W., et al., *Ultrathin Spinel LiMn2O4 Nanowires as High Power Cathode Materials for Li-Ion Batteries*. Nano Letters, 2010. **10**(10): p. 3852-3856.

109. Kim, H. and J. Cho, *Superior Lithium Electroactive Mesoporous Si@Carbon Core-Shell Nanowires for Lithium Battery Anode Material*. Nano Letters, 2008. **8**(11): p. 3688-3691.

110. Shaju, K.M. and P.G. Bruce, *A stoichiometric nano-LiMn2O4 spinel electrode exhibiting high power and stable cycling*. Chemistry of Materials, 2008. **20**(17): p. 5557-5562.

111. McDowell, M.T. and Y. Cui, *Single Nanostructure Electrochemical Devices for Studying Electronic Properties and Structural Changes in Lithiated Si Nanowires*. Advanced Energy Materials, 2011. **1**(5): p. 894-900.

112. Yang, Y., et al., *Single Nanorod Devices for Battery Diagnostics: A Case Study on LiMn2O4*. Nano Letters, 2009. **9**(12): p. 4109-4114.

113. Hu, L.B., et al., *Si nanoparticle-decorated Si nanowire networks for Li-ion battery anodes*. Chemical Communications, 2011. **47**(1): p. 367-369.

114. Li, J.L., et al., *Optimization of multicomponent aqueous suspensions of lithium iron phosphate (LiFePO4) nanoparticles and carbon black for lithium-ion battery cathodes*. Journal of Colloid and Interface Science, 2013. **405**: p. 118-124.

115. Chan, C.K., et al., *Nanowire Batteries for Next Generation Electronics*. Ieee International Electron Devices Meeting 2008, Technical Digest, 2008: p. 175-178.

116. Hassoun, J., et al., *A lithium ion battery using nanostructured Sn-C anode, LiFePO4 cathode and polyethylene oxide-based electrolyte*. Solid State Ionics, 2011. **202**(1): p. 36-39.

117. Liu, X.H., et al., *Lithium fiber growth on the anode in a nanowire lithium ion battery during charging*. Applied Physics Letters, 2011. **98**(18).

118. Boyano, I., et al., *Preparation of C-LiFePO4/polypyrrole lithium rechargeable cathode by consecutive potential steps electrodeposition*. Journal of Power Sources, 2010. **195**(16): p. 5351-5359.

119. Xu, M.W., et al., *Na3V2O2(PO4)(2)F/graphene sandwich structure for high-performance cathode of a sodium-ion battery*. Physical Chemistry Chemical Physics, 2013. **15**(31): p. 13032-13037.

120. Rahman, M.M., et al., *LiFePO4-Fe2P-C composite cathode: An environmentally friendly promising electrode material for lithium-ion battery*. Journal of Power Sources, 2012. **206**: p. 259-266.

121. Park, K.S., et al., *LiFeO2-Incorporated Li2MoO3 as a Cathode Additive for Lithium-Ion Battery Safety*. Chemistry of Materials, 2012. **24**(14): p. 2673-2683.

122. Qiu, Y.J., et al., *High-capacity cathode for lithium-ion battery from LiFePO4/(C + Fe2P) composite nanofibers by electrospinning*. Journal of Materials Science, 2014. **49**(2): p. 504-509.

123. Koenig, G.M., et al., *Composite of LiFePO4 with Titanium Phosphate Phases as Lithium-Ion Battery Electrode Material*. Journal of Physical Chemistry C, 2013. **117**(41): p. 21132-21138.

124. Wessells, C.D., et al., *Tunable Reaction Potentials in Open Framework Nanoparticle Battery Electrodes for Grid-Scale Energy Storage*. Acs Nano, 2012. **6**(2): p. 1688-1694.

125. Conway, B.E., *Transition From Supercapacitor To Battery Behavior In Electrochemical Energy-Storage*. Journal of the Electrochemical Society, 1991. **138**(6): p. 1539-1548.

126. Magasinski, A., et al., *Toward Efficient Binders for Li-Ion Battery Si-Based Anodes: Polyacrylic Acid*. Acs Applied Materials & Interfaces, 2010. **2**(11): p. 3004-3010.

127. Arthur, T.S., et al., *Three-dimensional electrodes and battery architectures*. Mrs Bulletin, 2011. **36**(7): p. 523-531.

128. Yao, M., et al., *Long cycle-life LiFePO4/Cu-Sn lithium ion battery using foam-type three-dimensional current collector*. Journal of Power Sources, 2010. **195**(7): p. 2077-2081.

129. Cui, L.F., et al., *Light-Weight Free-Standing Carbon Nanotube-Silicon Films for Anodes of Lithium Ion Batteries*. Acs Nano, 2010. **4**(7): p. 3671-3678.

130. Hassoun, J., et al., *An advanced configuration TiO2/LiFePO4 polymer lithium ion battery*. Journal of Power Sources, 2012. **217**: p. 459-463.

131. Nam, K.T., et al., *Virus-enabled synthesis and assembly of nanowires for lithium ion battery electrodes*. Science, 2006. **312**(5775): p. 885-888.

132. Sethuraman, V.A., et al., *Real-time stress measurements in lithium-ion battery negative-electrodes*. Journal of Power Sources, 2012. **206**: p. 334-342.

133. Hu, C.W., et al., *Real-time investigation of the structural evolution of electrodes in a commercial lithium-ion battery containing a V-added LiFePO4 cathode using in-situ neutron powder diffraction*. Journal of Power Sources, 2013. **244**: p. 158-163.

134. Misra, S., et al., *In Situ X-ray Diffraction Studies of (De)lithiation Mechanism in Silicon Nanowire Anodes*. Acs Nano, 2012. **6**(6): p. 5465-5473.

135. Mo, Y.F., S.P. Ong, and G. Ceder, *First-principles study of the oxygen evolution reaction of lithium peroxide in the lithium-air battery*. Physical Review B, 2011. **84**(20).

136. Cubuk, E.D., et al., *Morphological Evolution of Si Nanowires upon Lithiation: A First-Principles Multiscale Model*. Nano Letters, 2013. **13**(5): p. 2011-2015.

137. Zhao, K.J., et al., *Lithium-Assisted Plastic Deformation of Silicon Electrodes in Lithium-Ion Batteries: A First-Principles Theoretical Study*. Nano Letters, 2011. **11**(7): p. 2962-2967.

138. Tritsaris, G.A., et al., *Diffusion of Lithium in Bulk Amorphous Silicon: A Theoretical Study*. Journal of Physical Chemistry C, 2012. **116**(42): p. 22212-22216.

139. Zhang, Q.F., Y. Cui, and E.G. Wang, *Anisotropic Lithium Insertion Behavior in Silicon Nanowires: Binding Energy, Diffusion Barrier, and Strain Effect*. Journal of Physical Chemistry C, 2011. **115**(19): p. 9376-9381.

140. Tipton, W.W., et al., *Structures, phase stabilities, and electrical potentials of Li-Si battery anode materials*. Physical Review B, 2013. **87**(18): p. 184114.

141. Cui, Z.W., et al., *A second nearest-neighbor embedded atom method interatomic potential for Li-Si alloys*. Journal of Power Sources, 2012. **207**: p. 150-159.

142. Johari, P., Y. Qi, and V.B. Shenoy, *The Mixing Mechanism during Lithiation of Si Negative Electrode in Li-Ion Batteries: An Ab lnitio Molecular Dynamics Study*. Nano Letters, 2011. **11**(12): p. 5494-5500.

143. Kim, S.P., A.C.T. van Duin, and V.B. Shenoy, *Effect of electrolytes on the structure and evolution of the solid electrolyte interphase (SEI) in Li-ion batteries: A molecular dynamics study*. Journal of Power Sources, 2011. **196**(20): p. 8590-8597.

144. Huang, S. and T. Zhu, *Atomistic mechanisms of lithium insertion in amorphous silicon*. Journal of Power Sources, 2011. **196**(7): p. 3664-3668.

145. Haftbaradaran, H., et al., *Continuum and atomistic models of strongly coupled diffusion, stress, and solute concentration*. Journal of Power Sources, 2011. **196**(1): p. 361-370.

146. Cui, Z.W., F. Gao, and J.M. Qu, *A finite deformation stress-dependent chemical potential and its applications to lithium ion batteries*. Journal of the Mechanics and Physics of Solids, 2012. **60**(7): p. 1280-1295.

147. Bower, A.F., P.R. Guduru, and V.A. Sethuraman, *A finite strain model of stress, diffusion, plastic flow, and electrochemical reactions in a lithium-ion half-cell*. Journal of the Mechanics and Physics of Solids, 2011. **59**(4): p. 804-828.

148. Cui, Z.W., F. Gao, and J.M. Qu, *Interface-reaction controlled diffusion in binary solids with applications to lithiation of silicon in lithium-ion batteries*. Journal of the Mechanics and Physics of Solids, 2013. **61**(2): p. 293-310.

149. Pharr, M., et al., *Kinetics of Initial Lithiation of Crystalline Silicon Electrodes of Lithium-Ion Batteries*. Nano Letters, 2012. **12**(9): p. 5039-5047.

150. Tang, M., et al., *Modeling the competing phase transition pathways in nanoscale olivine electrodes*. Electrochimica Acta, 2010. **56**(2): p. 969-976.

151. Tang, M., W.C. Carter, and Y.M. Chiang, *Electrochemically Driven Phase Transitions in Insertion Electrodes or Lithium-Ion Batteries: Examples in Lithium Metal Phosphate Olivines*. Annual Review of Materials Research, Vol 40, 2010. **40**: p. 501-529.

152. Bower, A.F. and P.R. Guduru, *A simple finite element model of diffusion, finite deformation, plasticity and fracture in lithium ion insertion electrode materials*. Modelling and Simulation in Materials Science and Engineering, 2012. **20**(4).

153. An, Y. and H. Jiang, *A finite element simulation on transient large deformation and mass diffusion in electrodes for lithium ion batteries*. Modelling and Simulation in Materials Science and Engineering, 2013. **21**(7): p. 074007.

154. Chandrasekaran, R., et al., *Analysis of Lithium Insertion/Deinsertion in a Silicon Electrode Particle at Room Temperature*. Journal of the Electrochemical Society, 2010. **157**(10): p. A1139-A1151.

155. Cui, L.F., et al., *Carbon-Silicon Core-Shell Nanowires as High Capacity Electrode for Lithium Ion Batteries*. Nano Letters, 2009. **9**(9): p. 3370-3374.

156. Cui, L.F., et al., *Crystalline-Amorphous Core-Shell Silicon Nanowires for High Capacity and High Current Battery Electrodes*. Nano Letters, 2009. **9**(1): p. 491-495.

157. Wu, H. and Y. Cui, *Designing nanostructured Si anodes for high energy lithium ion batteries*. Nano Today, 2012. **7**(5): p. 414-429.

158. Wu, H., et al., *Engineering Empty Space between Si Nanoparticles for Lithium-Ion Battery Anodes*. Nano Letters, 2012. **12**(2): p. 904-909.

159. Cui, L.F., et al., *Inorganic Glue Enabling High Performance of Silicon Particles as Lithium Ion Battery Anode*. Journal of the Electrochemical Society, 2011. **158**(5): p. A592-A596.

160. Yao, Y., et al., *Interconnected Silicon Hollow Nanospheres for Lithium-Ion Battery Anodes with Long Cycle Life*. Nano Letters, 2011. **11**(7): p. 2949-2954.

161. Choi, J.W., et al., *Metal current collector-free freestanding silicon-carbon 1D nanocomposites for ultralight anodes in lithium ion batteries*. Journal of Power Sources, 2010. **195**(24): p. 8311-8316.

162. Zhu, J., et al., *Nanoporous silicon networks as anodes for lithium ion batteries*. Physical Chemistry Chemical Physics, 2013. **15**(2): p. 440-443.

163. Nadimpalli, S.P.V., et al., *Quantifying capacity loss due to solid-electrolyte-interphase layer formation on silicon negative electrodes in lithium-ion batteries*. Journal of Power Sources, 2012. **215**: p. 145-151.

164. Wang, J.W., et al., *Sandwich-Lithiation and Longitudinal Crack in Amorphous Silicon Coated on Carbon Nanofibers*. Acs Nano, 2012. **6**(10): p. 9158-9167.

165. Park, M.H., et al., *Silicon Nanotube Battery Anodes*. Nano Letters, 2009. **9**(11): p. 3844-3847.

166. Chan, C.K., et al., *Surface chemistry and morphology of the solid electrolyte interphase on silicon nanowire lithium-ion battery anodes*. Journal of Power Sources, 2009. **189**(2): p. 1132-1140.

167. Limthongkul, P., et al., *Electrochemically-driven solid-state amorphization in lithium-silicon alloys and implications for lithium storage*. Acta Materialia, 2003. **51**(4): p. 1103-1113.

168. Zhang, Q.F., et al., *Lithium Insertion In Silicon Nanowires: An ab Initio Study*. Nano Letters, 2010. **10**(9): p. 3243-3249.

169. Shenoy, V.B., P. Johari, and Y. Qi, *Elastic softening of amorphous and crystalline Li-Si Phases with increasing Li concentration: A first-principles study*. Journal of Power Sources, 2010. **195**(19): p. 6825-6830.

170. Hertzberg, B., J. Benson, and G. Yushin, *Ex-situ depth-sensing indentation measurements of electrochemically produced Si-Li alloy films*. Electrochemistry Communications, 2011. **13**(8): p. 818-821.

171. Sethuraman, V.A., et al., *In situ measurement of biaxial modulus of Si anode for Li-ion batteries*. Electrochemistry Communications, 2010. **12**(11): p. 1614-1617.

172. Sethuraman, V.A., et al., *In situ measurements of stress evolution in silicon thin films during electrochemical lithiation and delithiation*. Journal of Power Sources, 2010. **195**(15): p. 5062-5066.

173. Narri, G.-A. and G. Pistoia, *Lithium Batteries: Science and Technology*2004: Springer.

174. Armand, M. and J.M. Tarascon, *Building better batteries*. Nature, 2008. **451**(7179): p. 652-657.

175. Tarascon, J.M. and M. Armand, *Issues and challenges facing rechargeable lithium batteries*. Nature, 2001. **414**(6861): p. 359-367.

176. Boukamp, B.A., G.C. Lesh, and R.A. Huggins, *All-Solid Lithium Electrodes with Mixed-Conductor Matrix*. Journal of the Electrochemical Society, 1981. **128**(4): p. 725-729.

177. Hatchard, T.D. and J.R. Dahn, *In situ XRD and electrochemical study of the reaction of lithium with amorphous silicon*. Journal of the Electrochemical Society, 2004. **151**(6): p. A838-A842.

178. Chan, C.K., et al., *Structural and electrochemical study of the reaction of lithium with silicon nanowires*. Journal of Power Sources, 2009. **189**(1): p. 34-39.

179. Lee, S.J., et al., *Stress effect on cycle properties of the silicon thin-film anode*. Journal of Power Sources, 2001. **97-8**: p. 191-193.

180. Yu, C., et al., *Silicon Thin Films as Anodes for High-Performance Lithium-Ion Batteries with Effective Stress Relaxation*. Advanced Energy Materials, 2012. **2**: p. 68–73.

181. Sethuraman, V.A., et al., *In Situ Measurements of Stress-Potential Coupling in Lithiated Silicon*. Journal of the Electrochemical Society, 2010. **157**(11): p. A1253-A1261.

182. Prussin, S., *Generation and Distribution of Dislocations by Solute Diffusion*. Journal of Applied Physics, 1961. **32**: p. 1876-1881.

183. Li, J.C.M., Matall. Trans. A, 1978. **9**: p. 1353-1380.

184. Wang, W.L., S. Lee, and J.R. Chen, Journal of Applied Physics, 2002. **91**: p. 9584-9590.

185. Yang, F., Mater. Sci. Eng. A, 2005. **409**: p. 153-159.

186. Swaminathan, N., J. Qu, and Y. Sun, *An electrochemomechanical theory of defects in ionic solids. Part II. Examples*. Philosophical Magazine, 2007. **87**(11): p. 1723-1742.

187. Haftbaradaran, H., H.J. Gao, and W.A. Curtin, *A surface locking instability for atomic intercalation into a solid electrode*. Applied Physics Letters, 2010. **96**(9).

188. Zhao, K., et al., *Reactive Flow in Silicon Electrodes Assisted by the Insertion of Lithium*. Nano Letters, 2012. **12**(8): p. 4397-4403.

189. Zhao, K., et al., *Lithium-Assisted Plastic Deformation of Silicon Electrodes in Lithium-Ion Batteries: A First-Principles Theoretical Study*. Nano Letters, 2011. **11**(7): p. 2962-2967.

190. Zhao, K.J., et al., *Large Plastic Deformation in High-Capacity Lithium-Ion Batteries Caused by Charge and Discharge*. Journal of the American Ceramic Society, 2011. **94**: p. S226-S235.

191. Zhao, K., et al., *Fracture and debonding in lithium-ion batteries with electrodes of hollow core-shell nanostructures*. Journal of Power Sources, 2012. **218**: p. 6-14.

192. Zhang, J.P., et al., *A finite element method for transient analysis of concurrent large deformation and mass transport in gels*. Journal of Applied Physics, 2009. **105**(9).

193. Kang, M.K. and R. Huang, *A Variational Approach and Finite Element Implementation for Swelling of Polymeric Hydrogels Under Geometric Constraints*. Journal of Applied Mechanics-Transactions of the Asme, 2010. **77**(6).

194. Hong, W., Z.S. Liu, and Z.G. Suo, *Inhomogeneous swelling of a gel in equilibrium with a solvent and mechanical load*. International Journal of Solids and Structures, 2009. **46**(17): p. 3282-3289.

195. Gao, Y.F. and M. Zhou, *Strong stress-enhanced diffusion in amorphous lithium alloy nanowire electrodes*. Journal of Applied Physics, 2011. **109**(1): p. 014310-014310-6.

196. Yang, H., et al., *Orientation-Dependent Interfacial Mobility Governs the Anisotropic Swelling in Lithiated Silicon Nanowires*. Nano Letters, 2012. **12**(4): p. 1953-1958.

197. Haftbaradaran, H., H.J. Gao, and W.A. Curtin, *A surface locking instability for atomic intercalation into a solid electrode*. Applied Physics Letters, 2010. **96**(9): p. 3.

198. Koretsky, M.D., *Engineering and chemical thermodynamics*. 2004.

199. Hong, W. and X. Wang, *A phase-field model for systems with coupled large deformation and mass transport*. Journal of the Mechanics and Physics of Solids, 2013. **61**(6): p. 1281-1294.

200. Brassart, L. and Z.G. Suo, *Reactive flow in solids*. Journal of the Mechanics and Physics of Solids, 2013. **61**(1): p. 61-77.

201. Bower, A.F. and P.R. Guduru, *A simple finite element model of diffusion, finite deformation, plasticity and fracture in lithium ion insertion electrode materials*. Modelling and Simulation in Materials Science and Engineering, 2012. **20**(4): p. 045004.

202. INSPEC, *Properties of silicon*1988, New York: Institution of Electrical Engineers.

203. Sethuraman, V.A., et al., *In situ measurements of stress evolution in silicon thin films during electrochemical lithiation and delithiation*. Journal of Power Sources, 2011. **195**(15): p. 5062-5066.

204. Ruffo, R., et al., *Impedance Analysis of Silicon Nanowire Lithium Ion Battery Anodes*. Journal of Physical Chemistry C, 2009. **113**(26): p. 11390-11398.

205. Dimov, N., et al., *Characterization of carbon-coated silicon: Structural evolution and possible limitations*. Journal of Power Sources, 2003. **114**(1): p. 88-95.

206. Haftbaradaran, H., et al., *Method to deduce the critical size for interfacial delamination of patterned electrode structures and application to lithiation of thin-film silicon islands*. Journal of Power Sources, 2012. **206**(0): p. 357-366.

207. Liu, G., et al., *Polymers with Tailored Electronic Structure for High Capacity Lithium Battery Electrodes*. Advanced Materials, 2011. **23**(40): p. 4679-4683.

208. Arico, A.S., et al., *Nanostructured materials for advanced energy conversion and storage devices*. Nature Materials, 2005. **4**(5): p. 366-377.

209. Winter, M., et al., *Insertion electrode materials for rechargeable lithium batteries*. Advanced Materials, 1998. **10**(10): p. 725-763.

210. Kasavajjula, U., C.S. Wang, and A.J. Appleby, *Nano- and bulk-silicon-based insertion anodes for lithium-ion secondary cells*. Journal of Power Sources, 2007. **163**(2): p. 1003-1039.

211. Yu, C.J., et al., *Silicon Thin Films as Anodes for High-Performance Lithium-Ion Batteries with Effective Stress Relaxation*. Advanced Energy Materials, 2012. **2**(1): p. 68-73.

212. Schmalzried, H., *Chemical kinetics of solids*1995, Weinheim ; New York: VCH. xvi, 433 p.

213. Laidler, K.J., *Chemical kinetics*. 3rd ed1987, New York: Harper & Row. xi, 531 p.

214. Ding, N., et al., *Determination of the diffusion coefficient of lithium ions in nano-Si*. Solid State Ionics, 2009. **180**(2-3): p. 222-225.

215. Haxhimali, T., et al., *Orientation selection in dendritic evolution*. Nature Materials, 2006. **5**(8): p. 660-664.

216. Qin, R.S. and H.K.D.H. Bhadeshia, *Phase-field model study of the effect of interface anisotropy on the crystal morphological evolution of cubic metals*. Acta Materialia, 2009. **57**(7): p. 2210-2216.

217. Zheng, Q.S., *Theory of Representations for Tensor Functions—A Unified Invariant Approach to Constitutive Equations*. Applied Mechanics Reviews, 1994. **47**(11): p. 545-587.

218. Truesdell, C. and W. Noll, *The non-linear field theories of mechanics*. 2nd ed1992, Berlin ; New York: Springer-Verlag. x, 591 p.

219. Sethian, J.A., *A review of level set and fast marching methods for image processing*. Modern Methods in Scientific Computing and Applications, 2002. **75**: p. 365-396.

220. Boettinger, W.J., et al., *Phase-field simulation of solidification*. Annual Review of Materials Research, 2002. **32**: p. 163-194.

221. Tang, M., J.F. Belak, and M.R. Dorr, *Anisotropic Phase Boundary Morphology in Nanoscale Olivine Electrode Particles*. Journal of Physical Chemistry C, 2011. **115**(11): p. 4922-4926.

222. Tang, M., et al., *Model for the Particle Size, Overpotential, and Strain Dependence of Phase Transition Pathways in Storage Electrodes: Application to Nanoscale Olivines*. Chemistry of Materials, 2009. **21**(8): p. 1557-1571.

223. Chon, M.J., et al., *Real-Time Measurement of Stress and Damage Evolution during Initial Lithiation of Crystalline Silicon*. Physical Review Letters, 2011. **107**(4): p. 045503.

224. Hopcroft, M.A., W.D. Nix, and T.W. Kenny, *What is the Young's Modulus of Silicon?* Journal of Microelectromechanical Systems, 2010. **19**(2): p. 229-238.

225. Ye, J.C., et al., *Enhanced lithiation and fracture behavior of silicon mesoscale pillars via atomic layer coatings and geometry design*. Journal of Power Sources, 2014. **248**(0): p. 447-456.

226. Kim, S.K., et al., *Tuning Light Absorption in Core/Shell Silicon Nanowire Photovoltaic Devices through Morphological Design*. Nano Letters, 2012. **12**(9): p. 4971-4976.

227. Seidel, H., et al., *Anisotropic Etching Of Crystalline Silicon In Alkaline-Solutions .2. Influence Of Dopants*. Journal of the Electrochemical Society, 1990. **137**(11): p. 3626-3632.

228. Seidel, H., et al., *Anisotropic Etching Of Crystalline Silicon In Alkaline-Solutions .1. Orientation Dependence And Behavior Of Passivation Layers*. Journal of the Electrochemical Society, 1990. **137**(11): p. 3612-3626.

229. Huang, Z., et al., *Metal-Assisted Chemical Etching of Silicon: A Review*. Advanced Materials, 2011. **23**(2): p. 285-308.

230. Xiao, X., et al., *Improved cycling stability of silicon thin film electrodes through patterning for high energy density lithium batteries*. Journal of Power Sources, 2011. **196**(3): p. 1409-1416.

231. He, Y., et al., *Shape evolution of patterned amorphous and polycrystalline silicon microarray thin film electrodes caused by lithium insertion and extraction*. Journal of Power Sources, 2012. **216**: p. 131-138.

232. Goldman, J.L., et al., *Strain Anisotropies and Self-Limiting Capacities in Single-Crystalline 3D Silicon Microstructures: Models for High Energy Density Lithium-Ion Battery Anodes*. Advanced Functional Materials, 2011. **21**(13): p. 2412-2422.

233. Yi, R., et al., *Micro-sized Si-C Composite with Interconnected Nanoscale Building Blocks as High-Performance Anodes for Practical Application in Lithium-Ion Batteries*. Advanced Energy Materials, 2013. **3**(3): p. 295-300.

234. Glass, A.M. and K. Nassau, *Lithium Ion Conduction in Rapidly Quenched Li2o-Al2o3,Li2o-Ga2o3, and Li2o-Bi2o3 Glasses*. Journal of Applied Physics, 1980. **51**(7): p. 3756-3761.

235. Shen, L.F., et al., *Design and Tailoring of a Three-Dimensional TiO2-Graphene-Carbon Nanotube Nanocomposite for Fast Lithium Storage*. Journal of Physical Chemistry Letters, 2011. **2**(24): p. 3096-3101.

236. Yildirim, H., J.P. Greeley, and S.K.R.S. Sankaranarayanan, *The effect of concentration on Li diffusivity and conductivity in rutile TiO2*. Physical Chemistry Chemical Physics, 2012. **14**(13): p. 4565-4576.

237. Samsonov, G.V., *The Oxide Handbook*. 2nd ed1982, New York: IFI/Plenum.

238. Cho, J., et al., *Zero-strain intercalation cathode for rechargeable Li-ion cell*. Angewandte Chemie-International Edition, 2001. **40**(18): p. 3367-3369.

239. TANAKA, M., et al., *Orientation dependence of fracture toughness measured by indentation methods and its relation to surface energy in single crystal silicon*. International Journal of Fracture, 2006. **139**: p. 383-394.

240. Weidlich, M.M.W.J.E., *Empirical evaluation of fracture toughness: the toughness of quartz*. American Mineralogist, 1982. **67**: p. 1065-1068.

241. Xiao, X.C., P. Lu, and D. Ahn, *Ultrathin Multifunctional Oxide Coatings for Lithium Ion Batteries*. Advanced Materials, 2011. **23**(34): p. 3911-+.

242. He, Y., et al., *Alumina-Coated Patterned Amorphous Silicon as the Anode for a Lithium-Ion Battery with High Coulombic Efficiency*. Advanced Materials, 2011. **23**(42): p. 4938-4941.

243. Shao, Q., et al., *High aspect ratio composite structures with 48.5% thermal neutron detection efficiency*. Applied Physics Letters, 2013. **102**(6): p. 063505.

244. George, S.M., *Atomic Layer Deposition: An Overview*. Chemical Reviews, 2010. **110**(1): p. 111-131.

245. Aarik, J., et al., *Atomic layer deposition of titanium dioxide from TiCl4 and H2O: investigation of growth mechanism*. Applied Surface Science, 2001. **172**(1-2): p. 148-158.

246. Ghosal, S., et al., *Controlling Atomic Layer Deposition of TiO2 in Aerogels through Surface Functionalization*. Chemistry of Materials, 2009. **21**(9): p. 1989-1992.

247. Groner, M.D., et al., *Low-temperature Al2O3 atomic layer deposition*. Chemistry of Materials, 2004. **16**(4): p. 639-645.

248. Gosele, U. and K.N. Tu, *Growth-Kinetics of Planar Binary Diffusion Couples - Thin-Film Case Versus Bulk Cases*. Journal of Applied Physics, 1982. **53**(4): p. 3252-3260.

249. Yonghao, A. and J. Hanqing, *A finite element simulation on transient large deformation and mass diffusion in electrodes for lithium ion batteries*. Modelling and Simulation in Materials Science and Engineering, 2013. **21**(7): p. 074007.

250. Anderson, O., et al., *Density and Young's modulus of thin TiO2 films*. Fresenius' Journal of Analytical Chemistry, 1997. **358**(1-2): p. 290-293.

251. Herrmann, C.F., et al., *Properties of atomic-layer-deposited Al2O3/ZnO dielectric films grown at low temperature for RF MEMS*. 2005: p. 159-166.

252. Wortman, J.J. and R.A. Evans, *Youngs Modulus Shear Modulus and Poissons Ratio in Silicon and Germanium*. Journal of Applied Physics, 1965. **36**(1): p. 153-&.

253. Pan, B., et al., *Digital image correlation using iterative least squares and pointwise least squares for displacement field and strain field measurements*. Optics and Lasers in Engineering, 2009. **47**: p. 865–874.

APPENDIX 2A

IMPLEMENTATION OF UMATHT

In the subroutine UMATHT, the standard parameters received from ABAQUS are temperature T and its spatial gradient at the current state $\frac{\partial T}{\partial x_i}$, or equivalently, $\bar{C}$ and $\frac{\partial \bar{C}}{\partial \bar{x}_i}$ using the analogy discussed in the Section 2.3.2, respectively. The variables that are needed to pass out to ABAQUS are heat capacity per volume $\rho\frac{dU}{dT}$, heat flux f_i and its derivatives respective to temperature $\frac{\partial f_i}{\partial T}$ and temperature gradient $\frac{\partial f_i}{\partial\left(\frac{\partial T}{\partial x_i}\right)}$. Using the analogy discussed in the Section 2.3.2., the output variables in UMATHT are $\frac{1}{\det(\mathbf{F})}$ (for $\rho\frac{dU}{dT}$), $\frac{F_{iK}\bar{J}_K}{\det\mathbf{F}}$ (for f_i), $\frac{\partial}{\partial\bar{C}}\left(\frac{F_{iK}\bar{J}_K}{\det\mathbf{F}}\right)$ (for $\frac{\partial f_i}{\partial T}$), and $\frac{\partial\left(\frac{F_{iK}\bar{J}_K}{\det\mathbf{F}}\right)}{\partial\left(\frac{\partial\bar{C}}{\partial\bar{x}_i}\right)}$ (for $\frac{\partial f_i}{\partial\left(\frac{\partial T}{\partial x_i}\right)}$). The flux $\bar{J}_K$ depends on deformation gradient $\mathbf{F}$, stress $\boldsymbol{\sigma}$, and second Piolar Kirchhoff stress $\mathbf{S}$, as shown in Eq. (2.23). Therefore, the implementation of UMATHT also needs to access the deformation gradient $\mathbf{F}$ and stress $\boldsymbol{\sigma}$ (and $\mathbf{S}$) to calculate their derivatives (specifically, $\frac{\partial(\det\mathbf{F}\bar{\sigma}_h)}{\partial\bar{X}_L}$ in Eq. (2.23)), which are not the standard parameters received from ABAQUS.

The access of deformation gradient $\mathbf{F}$ can be realized by a "dummy" user-defined material subroutine UMAT. Here the "dummy" indicates that this subroutine UMAT does not actually perform any calculations but access the deformation gradient $\mathbf{F}$ from ABAQUS since UMAT is one of the two ways in ABAQUS that can retrieve the deformation gradient $\mathbf{F}$ (UHYPER is the other way). The stress tensor is obtained by

using another ABAQUS subroutine USDFLD, user-defined field variables. The accessed deformation gradient **F** and stress are given for every integration points and passed through to the subroutine UMATHT.In addition to deformation gradient $\mathbf{F}$ and stress in UMATHT, the gradients of $\det(\mathbf{F})\bar{\sigma}_h$ with respect to the reference coordinates $\mathbf{X}$ needs to be calculated, which is the main challenge here. In finite element method, the calculation of derivatives is realized through the shape function that interpolates a nodal value of a variable to its value at the integration point. However, here the deformation gradient **F** and stress are given at the integration points, not at the nodal points. We have implemented two ways to calculate this gradient $\frac{\partial}{\partial \bar{X}_L}\left(\det(\mathbf{F})\bar{\sigma}_h\right)$.

The first approach is the shape function extrapolation (SFE) method. $\det(\mathbf{F})\bar{\sigma}_h$ is calculated at all integration points within an element. Then these values at the integration points are extrapolated to their nodes using the inverse of a certain shape function (depending on the type of elements). Once the nodal value of $\det(\mathbf{F})\bar{\sigma}_h$ is known, their derivatives at the integration points are calculated using the same shape function. This algorithm is equivalent to the spatial finite difference method. Though this method is straightforward, two drawbacks exist. One shortcoming is that this method is element dependent because of the shape function, which involves more efforts to implement this method for different types of elements. The second one is more critical. The present method of calculating derivatives only involves local information within one element, which causes unrealistic gradients even the deformation and stress fields are relatively smooth throughout few neighboring elements. This unrealistic gradient fluctuates and makes the convergence difficult.

The second approach is to calculate this gradient using the pointwise least squares (PLS) method. In order to calculate $\frac{\partial}{\partial \bar{X}_L}\left(\det(\mathbf{F})\bar{\sigma}_h\right)$ of an integration point, we first select a "gradient calculation window" that contains a few elements around it. Within this window, $\det(\mathbf{F})\bar{\sigma}_h$ is assumed to be distributed linearly, i.e.,

$$\det(\mathbf{F})\bar{\sigma}_h\left(\bar{X}_K\right) = a_0 + a_1\bar{X}_1 + a_2\bar{X}_2 + a_3\bar{X}_3 \tag{2A.1}$$

where $\bar{X}_K$ are the initial coordinates of an integration point within the "gradient calculation window" and $\det(\mathbf{F})\bar{\sigma}_h\left(\bar{X}_K\right)$ is the value of this function at $\bar{X}_K$, and $a_i\left(i=0,1,2,3\right)$ are four unknown polynomial coefficients to be determined using least squares method. The gradient $\frac{\partial}{\partial \bar{X}_L}\left(\det(\mathbf{F})\bar{\sigma}_h\right)$ at an integration point can therefore be calculated based on the obtained coefficients a_1, a_2, and a_3.Since this method involves non-local information, other than the first method that only uses the local information within one element, the fluctuation of the gradient can be largely removed and the accuracy of the gradient can be greatly improved. This method has been used in obtaining meaningful strain field from measured displacement field in digital image correlation (DIC) [253].

As sketched in Fig. 2.A1, a Si pillar with a square cross section is used. The pillar geometry is 0.25×0.25×1. The pillar is charged by a unit flux with lateral displacement totally confined. The material parameters involved are the same as those listed in section 4.1 and 4×4×40 C3D20T elements are used to mesh this pillar. Fig. 2.A2 compares the gradient $\frac{\partial}{\partial \bar{X}_L}\left(\det(\mathbf{F})\bar{\sigma}_h\right)$ calculated from SFE and PLS methods at

different state of charge. In SFE method, the standard quadratic shape function of C3D20T element is used; while for PLS method, averaging over second order neighboring elements is adopted. It is found that the gradients calculated from these two methods are very close. However, the gradient from PLS method is always smoother than that from SFE method, which usually makes the convergence easier in most of our simulations.

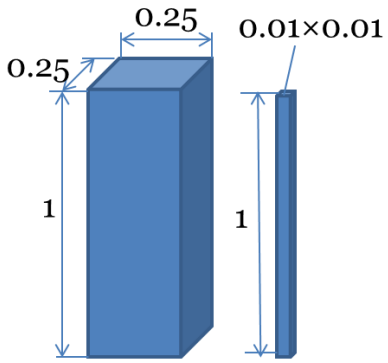

Figure 2.A1. Models used to examine the calculation of $\frac{\partial}{\partial \bar{\bar{X}}_3}\left(\det(\mathbf{F})\bar{\sigma}_h\right)$ in UMATHT in Appendix 2A, fat square pillar used to compare the shape function extrapolation (SFE) method and the pointwise least square (PLS) method, and thin square pillar used to examine the "gradient calculation window" in PLS method.

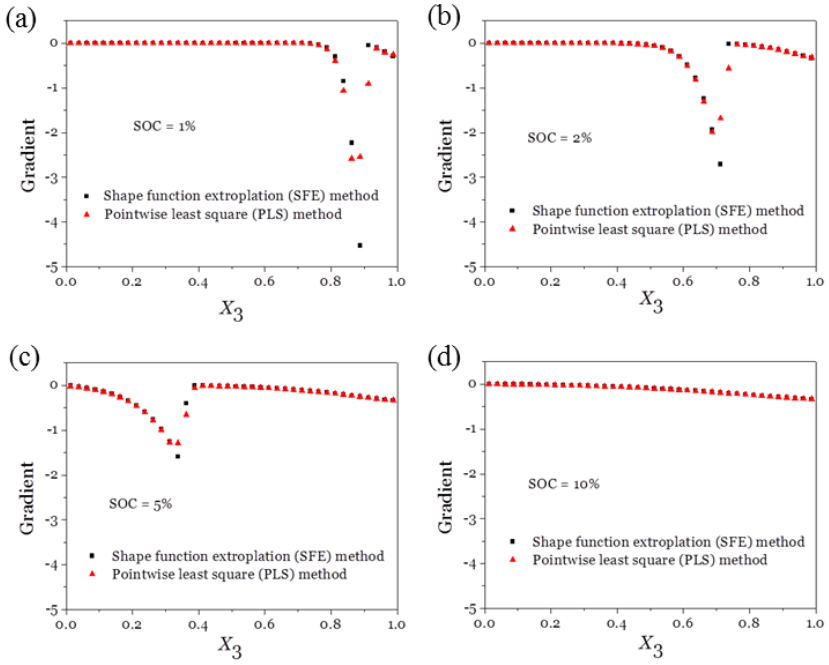

Figure 2.A2. Gradient $\frac{\partial}{\partial \bar{X}_3}\left(\det(\mathbf{F})\bar{\sigma}_h\right)$ profile in X_3 direction at different state of charge (SOC), calculated from shape function extrapolation (SFE) and pointwise least square (PLS) methods. SOCs are (a) 1%, (b) 2%, (c) 5%, and (d) 10%, respectively. Here the dimensionless time has been used.

It is important to note that to obtain reasonable and accurate gradients $\frac{\partial}{\partial \bar{X}_L}\left(\det(\mathbf{F})\bar{\sigma}_h\right)$ using the PLS method, the size of "gradient calculation window" is critical. There is a trade-off between the accuracy and smoothness of the gradient. Fig. 2.A3 shows a case study on the effect of "gradient calculation window" using an example of charging a laterally confined slender Si pillar (Fig. 2.A1). The dimension is 0.01×0.01×1 and the mesh is 1×1×100. A unit flux is applied on the top surface. The materials properties are given in the Section 2.4.1. The "gradient calculation window" is defined by the number of neighboring element, i.e., "0" means the element itself, "1" means the first order neighboring elements and so on. The profiles of Li concentration in

X_3 direction at different state of charge (SOC) are shown in Fig. 2.A3. The results show that for this relatively homogeneous deformation (1D problem), the size of "gradient calculation window" is insignificant. The difference only lies on the efficiency of convergence, namely, small "window" leads to much slower convergence rate than that for larger "window". The calculations presented in this paper normally use 2nd order or 3rd order neighboring elements to conduct the PLS method.

With all the necessary quantities accessed and calculated, the mass diffusion in large deformation is implemented in UMATHT through the analogy as discussed in the Section 2.3.2.

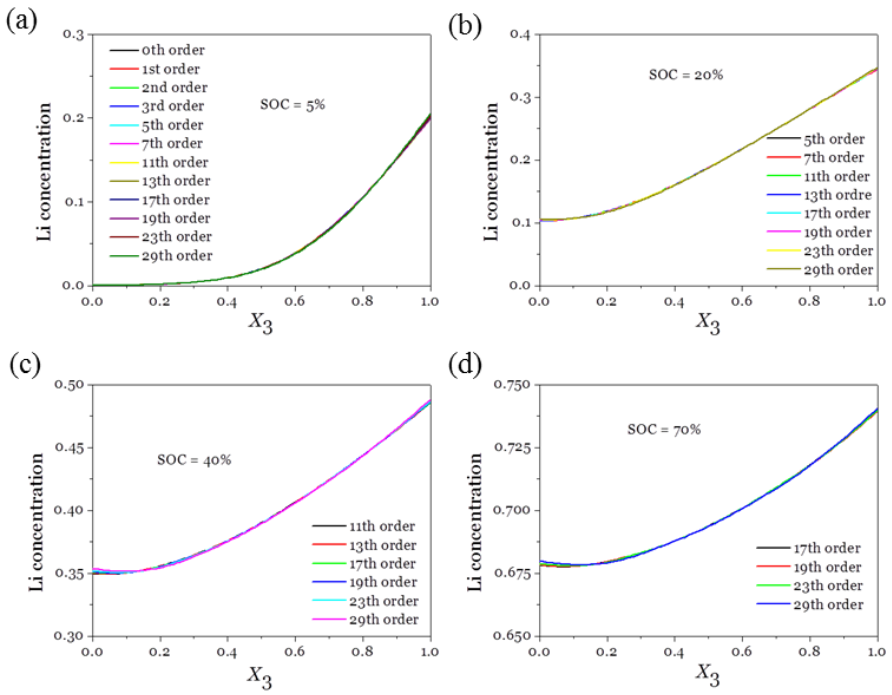

Figure 2.A3. The profile of Li concentration in X_3 direction at different state of charge (SOC) using various "gradient calculation window. The SOCs are (a) 5%, (b) 20%, (c) 40%, and (d) 70%.

APPENDIX 2B

BENCHMARK EXAMPLES

Several benchmark examples are conducted to show the correct implementation of all aspects discussed in Section 2.3.

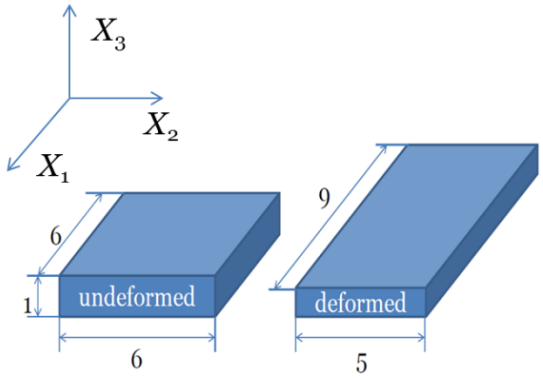

Figure 2.B1. Models used in the benchmark examples in Appendix 2B, an undeformed thin plate with geometry 6×6×1, and a deformed thin plate with geometry 9×5×1. The deformation is prescribed as $x_1 = 1.5X_1$, $x_2 = 5X_2/6$.

Fig. 2.B1 illustrates a thin film model used in the benchmark studies. X_3 axis is normal to the film and X_1 and X_2 axis are along the in-plane directions. The thickness of the film is set to 1. To illustrate that the large deformation can be correctly captured, a large deformation, $x_1 = 1.5X_1$, $x_2 = 5X_2/6$, is applied to deform the film as shown in Fig. 2.B1. We use 27 C3D8T elements in the benchmark studies.

2B.1. Benchmark updated Lagrange and total Lagrange descriptions on a same problem

The analogy between mass diffusion and heat transfer in ABAQUS lies on one basic foundation, which is the mass conservation law for diffusion in total Lagrange description (Eq. (2.22)) is equivalent to the heat conservation law for heat transfer in updated Lagrange description (Eq. (2.24)) through Eq. (2.25). To verify that this equivalence does describe the same physics, we create two scenarios. In the first scenario, we use ABAQUS built-in Fickian diffusion to study a pure heat transfer problem, i.e., without thermal expansion and mechanical deformation. The model is shown on the left

side in Fig. A1b. The top surface is subjected to a prescribed unit temperature for a unit time. Thus the governing equation in this case is Eq. (2.24). In the second scenario, we apply large deformation and then conduct the heat transfer. The model is shown on the right side in Fig. 2.B1. This deformation is uniform, which can be accurately described by these 27 elements used in the example. The boundary condition for heat transfer is the same as that in the first scenario. In this analysis, the large deformation option is on and the deformation gradient can be accessed by using the "dummy" UMAT subroutine as discussed in Appendix 2A. The conservation law is described in the total Lagrange framework, which is similar to Eq. (2.22). We implement Eq. (2.22) in updated Lagrange framework using Eq. (2.25) in UMATHT. These two scenarios solve a pure heat transfer problem since the deformation and heat transfer are intentionally decoupled. Fig. 2.B2 shows that the temperature profiles in the X_3 direction for these two scenarios identifies with each other for several time steps, which verifies that the realization of total Lagrange description in updated Lagrange framework via Eq. (2.25).

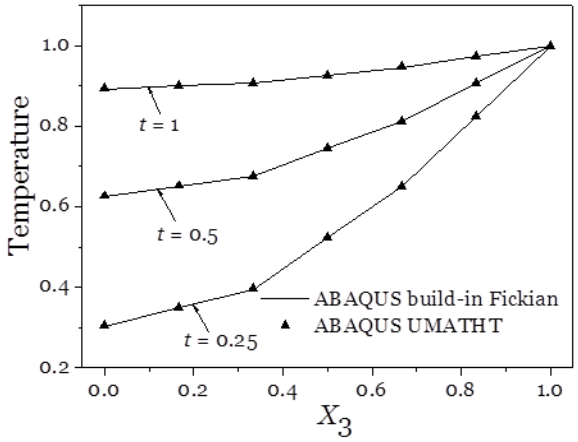

Figure 2.B2. Benchmark of numerical implementation in user subroutines UMATHT. Upon applying a prescribed temperature boundary condition, temperature profiles in X_3 direction at different time steps, using ABAQUS built-in thermal transport with Fickian law and ABAQUS UMATHT by expressing the total Lagrange description in updated Lagrange framework via Eq. (2.25).

2B.2. Benchmark prescribed flux boundary condition

Still because of the discrepancy between total Lagrange and updated Lagrange descriptions, flux is applied on different element of area in these two descriptions. This discrepancy can be eliminated by using the Nanson's formula as discussed in Eq. (2.34). We create two scenarios as benchmarks. The first scenario is similar to the first case in section 2B.1, except that the prescribed temperature boundary condition is replaced by a prescribed flux boundary condition. Specifically, the top surface of the film is subjected to a unit heat flux for a unit time. The same prescribed flux boundary condition and the deformation field are applied in the second scenario. To accommodate the change of the area on top surface, subroutine DFLUX is used in the second scenario along with UMATHT for the heat conservation law defined in updated Lagrange framework when large deformation presents. It should be emphasized here again that these two cases are temperature-deformation decoupled. The deformation is introduced solely in order to show that a proper transformation between total Lagrange and updated Lagrange framework is needed to correctly describe the physics. Fig. 2.B3 shows that the temperature profiles in the X_3 direction at different time steps for these two scenarios are identical, which verifies the implementation of DFLUX to capture the flux when large deformation presents.

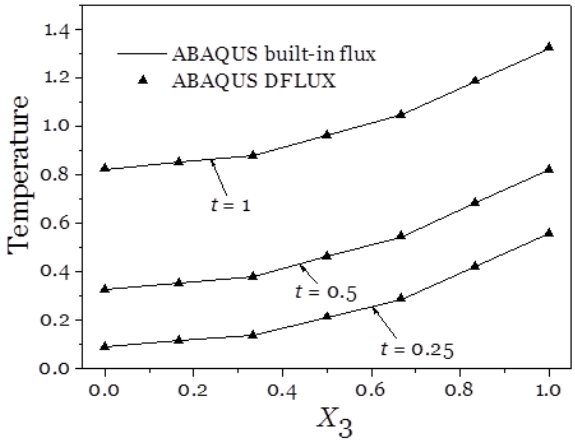

Figure 2.B3. Benchmark of numerical implementation in user subroutine DFLUX. Upon applying a prescribed flux boundary condition, temperature profiles in X_3 direction at different time steps, using ABAQUS built-in heat transfer/flux boundary condition and ABAQUS UMATHT/DLFUX via Eqs. (2.25) and (2.34).

2B.3. Benchmark thermal expansion for large deformation

For large deformation, the thermal expansion needs to redefine to realize the desired compositional expansion (Eq. (2.28)) through Eq. (2.32). We study a steady state problem by increasing the temperature from zero to unit and the compositional expansion coefficient β= 0.5874. The thermal expansion is redefined in UEXPAN via Eq. (2.32). As shown in Fig. 2.B4, a desired linear expansion is produced. The slope is just the compositional expansion β (=0.5874).

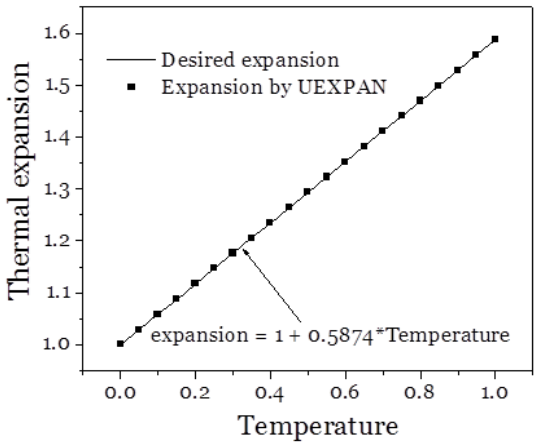

Figure 2.B4. Benchmark of numerical implementation in user subroutines UEXPAN. Thermal expansion versus temperature for a static state problem, by increasing the temperature from 0 to 1, using ABAQUS UEXPAN. The coefficient of thermal expansion is taken to be 0.5874 and thus large deformation due to elevated temperature is introduced.

APPENDIX 2C

ANALYTICAL SOLUTION FOR A 1D PROBLEM

As illustrated in Fig. 2.2a, the substrate is assumed rigid. Due to the symmetry of the problem, there are five independent field variables $\lambda_1^e(X_1,t)$, $\lambda_2^e(X_1,t)$, $\lambda_1^p(X_1,t)$, $\lambda_2^p(X_1,t)$, and $\bar{C}(X_1,t)$.

From the incompressibility of plastic deformation

$$\ln\left(\lambda_1^p\lambda_2^p\lambda_2^p\right)=0, \tag{2C.1}$$

and the fixed in-plane displacement condition imposed by rigid substrate

$$\lambda_2=1, \tag{2C.2}$$

as well as the traction free condition in the thickness direction

$$\sigma_1=0, \tag{2C.3}$$

one obtains

$$\ln\lambda_2^p=-\ln\lambda_2^e-\ln\left(1+\beta\bar{C}\right), \tag{2C.4}$$

$$\ln\lambda_{eq}^p=2\left|\ln\lambda_2^P\right|. \tag{2C.5}$$

In addition, from the traction free condition in the thickness direction and the elastic constitutive relations, one can reach

$$\sigma_2=\frac{E}{1-\nu}\ln\lambda_2^e, \tag{2C.6}$$

$$\sigma_v=\frac{E}{1-\nu}\left|\ln\lambda_2^e\right|. \tag{2C.7}$$

Substituting the von Mises stress and equivalent strain into the yielding criterion, one obtains

$$\frac{E}{1-\nu}\left|\ln\lambda_2^e\right|=\sigma_{Y0}+2E^p\left|\ln\lambda_2^P\right|. \tag{2C.8}$$

During lithiation, there is no unloading and the film is subjected to lateral compressive stress, which gives

$$\ln \lambda_2^e \le 0, \ln \lambda_2^P \le 0. \tag{2C.9}$$

Then Eq. (2C.8) leads to

$$-\frac{E}{1-\nu} \ln \lambda_2^e = E \ln \lambda_{Y0} + 2E^p \left(\ln \lambda_2^e + \ln\left(1+\beta \bar{C}\right) \right), \tag{2C.10}$$

from which all the four independent deformation fields could be determined as a function of $\bar{C}$ in the following

$$\ln \lambda_2^e = -\frac{(1-\nu) E \ln \lambda_{Y0} + 2(1-\nu) E^p \ln\left(1+\beta \bar{C}\right)}{E + 2(1-\nu) E^p}, \tag{2C.11}$$

$$\ln \lambda_1^e = \frac{2\nu E \ln \lambda_{Y0} + 4\nu E^p \ln\left(1+\beta \bar{C}\right)}{E + 2(1-\nu) E^p}, \tag{2C.12}$$

$$\ln \lambda_2^p = \frac{(1-\nu) E \ln \lambda_{Y0} - E \ln\left(1+\beta \bar{C}\right)}{E + 2(1-\nu) E^p}, \tag{2C.13}$$

$$\ln \lambda_1^p = \frac{-2(1-\nu) E \ln \lambda_{Y0} + 2E \ln\left(1+\beta \bar{C}\right)}{E + 2(1-\nu) E^p}. \tag{2C.14}$$

Two dependent variables which explicitly enter the governing equation for diffusion problem could be calculated as

$$\sigma_h = -E \frac{2E \ln \lambda_{Y0} + 4E^p \ln\left(1+\beta \bar{C}\right)}{3E + 6(1-\nu) E^p}, \tag{2C.15}$$

$$\ln \lambda_1 = \frac{-(2-4\nu) E \ln \lambda_{Y0} + \left(3E + (2+2\nu) E^p\right) \ln\left(1+\beta \bar{C}\right)}{E + 2(1-\nu) E^p}. \tag{2C.16}$$

Aforementioned formulas hold for plastic deformation, which is specified by the condition of yielding

$$\frac{1}{1-\nu}\ln\left(1+\beta\bar{C}\right) > \ln\lambda_{Y0}. \tag{2C.17}$$

The formulas for elastic deformation can be degenerated from the plastic solution by simply taking $E^p \to \infty$.